applied sciences

MDPI

Article

Regional Strain Rates and Seismogenic Potential of the North Segment of the North–South Seismic Belt, China: Constraints from GNSS Observations

Nan Zhang [1,2,3], Weijun Gan [1,4,*], Yongsheng Zhou [1,5] and Xiwei Fan [1,2,6]

[1] Institute of Geology, China Earthquake Administration, Beijing 100029, China; zhangnan@ies.ac.cn (N.Z.); zhouysh@ies.ac.cn (Y.Z.); fanxiwei@ies.ac.cn (X.F.)
[2] Key Laboratory of Seismic and Volcanic Hazards, China Earthquake Administration, Beijing 100029, China
[3] Ningxia Seismological Bureau, Yinchuan 750001, China
[4] State Key Laboratory of Earthquake Dynamics, Institute of Geology, China Earthquake Administration, Beijing 100029, China
[5] State Key Laboratory of Earthquake Dynamics and Forecasting, Institute of Geology, China Earthquake Administration, Beijing 100029, China
[6] Xinjiang Pamir Intracontinental Subduction National Observation and Research Station, Beijing 100029, China
* Correspondence: wjgan@ies.ac.cn

Abstract

Based on GNSS observations from the Crustal Movement Observation Network of China (CMONOC) spanning 1998–2024, this study investigates crustal deformation characteristics within the northern segment of the North–South Seismic Belt in China. The analysis incorporates the horizontal velocity field, strain rate field, sub-block strain rates, fault slip rates, and associated slip deficits. The results reveal extensional deformation across five tectonic units: the eastern Qiangtang Block, the central–eastern Bayan Har Block, the central Qilian Block, the northern Alxa Block, and the north–central Longzhong Basin. Compressional deformation is predominantly localized along the northern and southern boundaries of the Qilian Block, the western margin of the southern Qaidam Block, the eastern segment of the East Kunlun Fault, and the Hoh Xil region. Zones of elevated shear strain rate are principally concentrated in four regions: the junction of the northern Qilian Block and the Alxa Block, the southern Qaidam Block, the central–eastern Bayan Har Block, and the eastern Qiangtang Block. Historical peak values of maximum principal extensional-shear strain are identified in the northern Longzhong Basin, whereas peak compressional-shear strain occurs in the central Qilian Block–western Qaidam Block and the eastern Qiangtang Block. The analysis reveals heterogeneous fault locking along the northern Western Qinling Range. Most segments of the East Kunlun Fault exhibit slip deficits, with the exception of the Alak Lake–Tusuo Lake segment. The degree of locking is generally homogeneous, except for the Tusuo Lake and Maqu segments. Both the slip deficit and slip rate of the Liupanshan Fault exhibit an increasing trend along its strike. Regions with high seismic hazard potential are identified, primarily including: the Xiugou–Maqiu segment of the East Kunlun Fault, the Guyuan–Jingyuan segment of the Liupanshan Fault, the Hasishan–Machangshan segment of the Haiyuan Fault, the Kuban Mountain segment of the Altyn Tagh North Marginal Fault, the Yumen and Sunan segments of the Qilian North Marginal Fault, the Tianshui and Luanfeng segments of the West Qinling North Marginal Fault, the eastern Altyn Tagh Fault Zone, the central–western East Kunlun Fault Zone, the northern boundary of the Qilian Block, the northern

Academic Editor: Ludovit Kovanic

Received: 23 July 2026
Revised: 10 October 2026
Accepted: 27 October 2026
Published: 2 November 2026

Copyright: © 2026 by the authors. Licensee MDPI, Basel, Switzerland. This article is an open access article distributed under the terms and conditions of the Creative Commons Attribution (CC BY) license.

Zhuanglanghe Fault, the southern Haiyuan Fault, the northern Liupanshan Fault, and the eastern West Qinling North Marginal Fault Zone.

Keywords: China North–South seismic belt; GNSS; strain rate field; active faults; locking rate; seismic activity

1. Introduction

The northern segment of the North–South Seismic Belt is located at the intersection of the east–west and north–south tectonic systems in the Chinese mainland, forming a critical tectonic transition zone [1] (Zhang P et al. 2003). To its northwest lies the Alxa–Tarim Block, to the southwest the Qinghai–Tibet Block, to the east the North China Geological Block, and to the southeast the South China Block. The study area is predominantly delineated by the Qilian–Haiyuan Fault Zone, the Altyn Tagh Fault Zone, and their affiliated subsidiary faults.

Studies based on the GNSS vertical velocity field indicate that most areas along the eastern margin of the Tibet Plateau exhibit a rising trend, with differential movements between the upper and lower crusts. The vertical sliding rates of the Helan Mountain East Slope Fault and the Liupan Mountain Fault range between 1 and 1.6 mm/a. To maintain the current uplift rates across these regions, the material filling rate from the lower crust to the upper mantle must exceed that from the upper crust; this result corroborates the hypothesis that lower crustal flow occurs along the eastern margin of the plateau [2]. Regarding the aforementioned inference pertaining to differential material filling rates, it is explicitly clarified that this statement refers to net mass transfer across the Moho discontinuity—the first-order crust–mantle boundary—rather than to internal transformation within the crust. Under the prevailing tectonic regime of the study region, asthenospheric upwelling induces partial melting at the base of the lithosphere, and the resultant buoyant crustal material is transported from the lower lithosphere (encompassing both the lowermost crust and the uppermost mantle) upward into the upper crust, thereby accommodating sustained crustal uplift. Should the rate of this upward mass transfer across the crust–mantle boundary into the upper crust exceed the combined rate of lateral crustal material extrusion and surface erosion, the net volume of the upper crust would increase, consequently maintaining the long-term positive uplift rates recorded by GNSS.

The seismogenic structure of the Wenchuan earthquake is characterized by pronounced right-lateral thrust kinematics, which serve to intensify compressional stress accumulation along the fault zone at the northern margin of the Western Qinling Mountains, ultimately inducing a locked fault state. The GNSS-derived strain rate field of the Chinese mainland [3], indicates that the strain rate magnitude within the Ordos Block is approximately one order of magnitude lower than that recorded in its surrounding peripheral zones. By integrating the fast-wave direction predicted from GNSS-derived surface deformation with mantle deformation information retrieved from shear wave splitting observations, Chang L et al. [4] inferred that crustal deformation across the western margin of the Ordos Block, the Alxa Block, and the northwestern segment of the northeastern plateau edge is predominantly governed by shear processes. Their investigation further revealed robust crust–mantle coupling in these regions, manifested as vertically coherent crustal deformation. Conversely, the Ordos Block exhibits pronounced discrepancies between its shallow and deep deformation regimes, accompanied by weak seismic anisotropy. Collectively, these observations substantiate the contention that the Ordos Block preserves the long-term stability inherent to the ancient cratonic lithosphere. Vertical leveling measurement results reported by Tang F et al. [5] show that within the North China Block, seismic activity is the most intense along the southwestern mar-

gin of the Ordos Block; crustal deformation is more intense in the southeastern region compared with the northwestern region; the southwestern margin of the Ordos Block exhibits left-lateral and strong compressional deformation, while the Yinchuan Fault Zone shows right-lateral and extensional deformation, and the Hetao Fault Zone displays left-lateral and extensional deformation. GNSS observations reveal that current structural deformation along the northeastern edge of the Tibet Plateau is primarily concentrated within a range of hundreds of kilometers west of the Haiyuan–Liupanshan structural belt [6].

The hazard potential of active faults is jointly affected by the structural orientation, in situ stress conditions, electrical properties and rheological characteristics of the surrounding rock medium, and is closely correlated with the location and intensity of fault locking. Heterogeneity in deep structural configurations gives rise to spatial variations in the electrical, rheological and mechanical properties of the crust–mantle system, which constitutes one of the core factors accounting for the spatial differences of seismic activity within the study area [7]. Strong earthquakes are predominantly distributed within low-velocity (or low-resistivity) crustal domains and thin lithospheric regions that are adjacent to stable high-velocity (or high-resistivity) geophysical structures. Medium-to-strong earthquakes occurring within these blocks and their boundary fault zones are predominantly centered near significant electrical boundary zones [8]. Using deep geophysical exploration techniques (such as deep seismic sounding and geoelectromagnetic sounding) along with long-wavelength body wave reception functions, researchers elucidated the structural morphology of the crust and upper mantle at the northeastern margin of the Tibet Plateau. Employing tomographic imaging and other technologies, they obtained structural data of the upper mantle in this region to investigate its formation mechanisms, evolutionary processes, and electrical, rheological, and mechanical properties. During the initial period of crustal deformation in the northern segment of the North–South Seismic Belt, crustal materials experienced northeastward directional migration. Migrating crustal materials exerted a compressional forcing on the Songpan–Ganzi Block, while being simultaneously obstructed by the South China Block, Ordos Block, Alxa Block, and Qilian Block. This geodynamic process ultimately drove crustal thickening and marginal uplift, triggering regional orogenic activity [9]. The deformation pattern of the study area is dominated by continuous ductile flow. In the horizontal direction, the Alxa Block and Qaidam Block, which exhibit high deformation intensity, are sandwiched by the Qilian Block characterized by lower deformation intensity; meanwhile, the Songpan–Ganzi–West Qinling Block with lower deformation intensity transitions gradually to the Ordos Block with higher deformation intensity. In the vertical direction, the lithosphere conforms to the vertically coherent deformation model, with pervasive crustal thickening as the primary characteristic [10]. The middle and lower crust of suture zones and orogenic belts generally develop fragmented and relaxed structures, marked by the alternation of high-velocity and low-velocity layers, with low-velocity structures dominating. This makes these regions key areas for rheological sliding [9] (Jia S and Zhang X 2008). Electrical gradient zones and low-resistance anomaly zones have been identified in fault zones along the northern margin of the Western Qinling Mountains, the southern margin of the Northern Qilian Mountains, and the northern margin of the Qilian Mountains–Haiyuan Fault Zone [11]. Compared with stable blocks in the north, the vertical relative movement rate on the outer side of the northeastern margin of the plateau is approximately 0 mm/a, while the rate on the inner side generally ranges from 1 to 2 mm/a [12]. Gravitational potential energy is also confirmed to be an important driving factor for crustal deformation along plateau margins [13].

Strong earthquakes generally occur within the locked segments of block boundary faults, particularly at the junctions between strongly locked and weakly locked segments, the junctions between compressively locked and extensionally locked segments, or in regions with anomalous fault displacement. Under the framework of inherited tectonic activity, the local slip rates and strain field variations derived from GNSS observations serve as key indicators

for identifying strain accumulation and fault locking states within fault zones. Stress distributed along the periphery of co-seismic ruptures and across the lower crust–upper mantle experiences either accumulation or attenuation during the inter-seismic, co-seismic, and post-seismic periods. This process is governed by the rheological properties of rocks and ultimately produces surface deformation that can be detected via GNSS technology [14].

GNSS technology boasts the advantages of long observational time series, extensive spatial coverage, high observational accuracy, and distinct trend characteristics. Based on GNSS-derived deformation fields, the primary technical approaches and methods for investigating the correlation between surface motion and seismogenic processes include: calculating vertical deformation rate gradients; conducting spatiotemporal analysis of strain rate fields; inverting fault plane slip distribution using co-seismic displacement; comprehensively evaluating seismic hazard by integrating tectonic dynamic background, deformation patterns, transverse cross-section structures, historical strong earthquake rupture sequences, and GNSS deformation data; inverting the spatiotemporal evolution of focal rupture with constraints from near-field GNSS displacement records, strong-motion acceleration observations, and P-wave phases; and performing multi-spatial-scale wavelet decomposition on GNSS strain rate fields.

The Chinese Mainland Tectonic Environment Monitoring Network (CMTEMN) is a national scientific research project led by the China Earthquake Administration, which applies Global Navigation Satellite System (GNSS) technology to geoscientific research. At present, it is the infrastructure construction project with the largest scale, widest coverage, and highest observation precision in this field in China [15].

Against the backdrop of frequent strong seismicity in active tectonic regions, large uncertainties remain in current understandings of crustal stress accumulation, slip deficit distribution and regional seismic hazard levels, which cannot satisfy the practical requirements of regional seismic risk prevention and mitigation. To clarify the magnitude and spatial distribution of slip deficit on major active faults, as well as the corresponding potential seismic hazard, it is necessary to accurately quantify the contribution weights of various influencing factors and properly address the interdependent correlations among different influencing factors. This study focuses on three core research objectives:

(1) To construct a reliable slip deficit distribution model for major active faults in the study area based on standardized integration and processing of multi-source, peer-validated geophysical observation data;
(2) To quantify the uncertainty of estimation results within a framework that explicitly incorporates the interdependence of influencing factors, so as to identify the key controlling factors of regional seismic hazard distribution;
(3) To validate the applicability of the adopted multi-factor uncertainty quantification framework for seismic hazard assessment in active tectonic regions, and provide a more robust research foundation for subsequent regional seismic hazard zoning and disaster prevention planning.

Physical field inversion methods are constrained by objective conditions and are generally limited to relatively short temporal observation ranges. Restricted by the deployment density of Global Navigation Satellite System (GNSS) stations, researchers usually need to conduct concentrated observation in specific study areas or integrate multi-source GNSS observation datasets for joint analysis. To address the temporal and spatial limitations of the "Land State Network" (with an observation span of only 20 years), this study adopts the Eurasian reference velocity field derived from the TRF2014 reference frame. The adopted dataset covers the period from 1998 to 2024 and the geographic range of 29–43°N, 92°–111°E, with the interference of non-tectonic factors removed. The Eulerian motion vectors were solved using the least squares method, yielding velocity and strain rate fields under the ITRF2014 geocentric coordinate system. Figure 1 illustrates the velocity field across the entire Tibet Plateau during

1998–2024 under the ITRF2014 reference framework, providing a large-scale context for regional crustal deformation studies and clarifying the tectonic driving mechanisms of the Qinghai–Tibet Block over northern study areas. This study projects station velocities from both sides of active fault segments to corresponding fault zones for comparative analysis; based on the obtained velocity field and strain rate field, secondary blocks are further delineated within the main block to analyze the variation characteristics of strain rate, so as to explore the strain accumulation trend and strong earthquake activity characteristics of these sub-blocks and major faults. Taking the velocity field as a constraint condition, this study constructs the corresponding model by adopting the open-source program DEFNODE based on elastic dislocation theory. On this basis, the study fully considers the interaction between adjacent blocks and faults and inversely obtains the interannual variation characteristics of fault sliding rate, slip deficit rate and locking rate. By integrating indicators such as fault movement characteristics, geological structure, rheological properties, electrical characteristics, mechanical properties, and seismic activity, we conduct preliminary assessments of areas at high seismic risk.

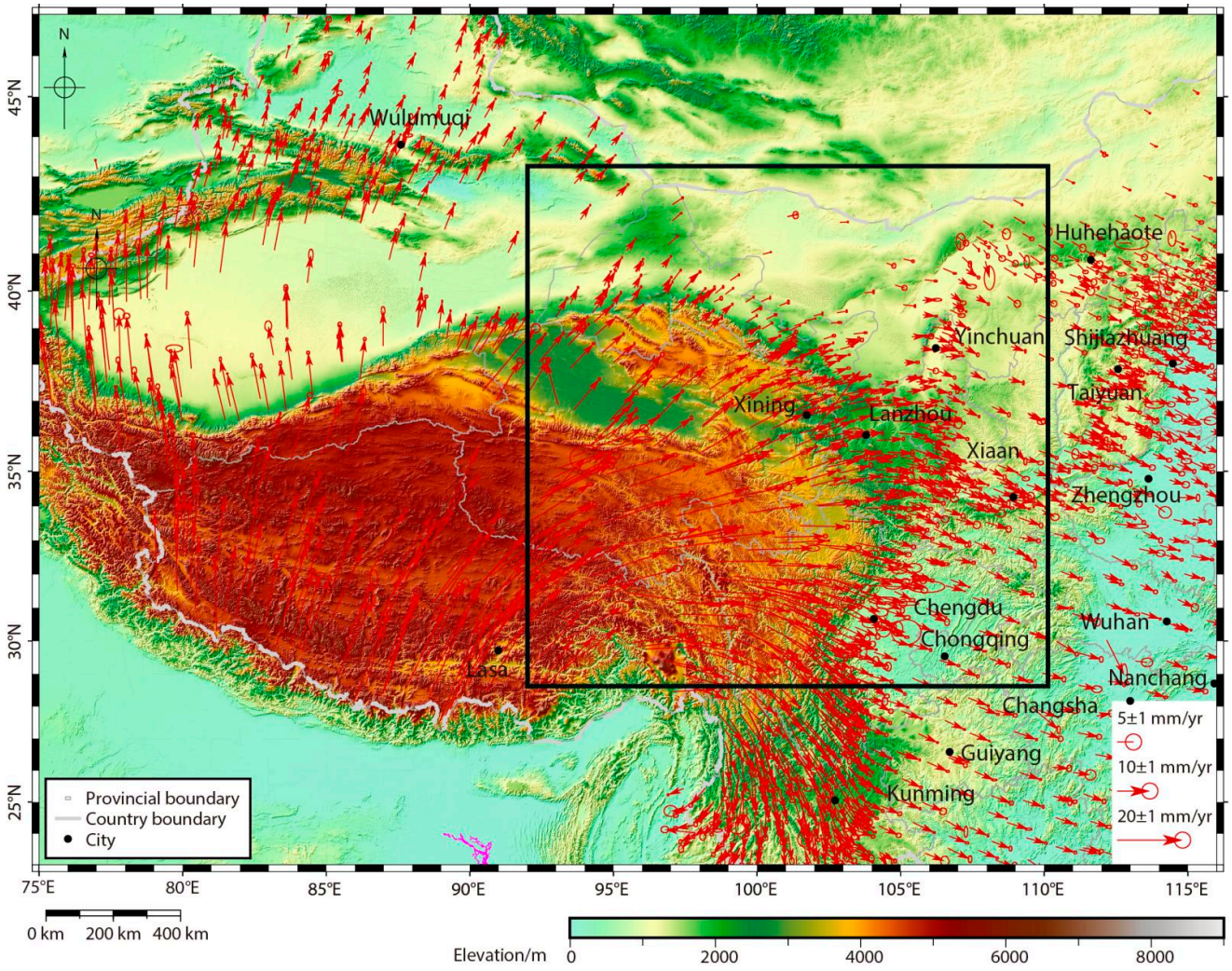


Figure 1. GNSS velocity field of the Tibet Plateau (1998–2024, using the ITRF 2014 Eurasian reference system; the study area is indicated by a black rectangular box， the purplish-red/magenta thin lines in the figure indicate marine boundary lines, including the Exclusive Economic Zone (EEZ)).

2. Geological Structure of the Study Area: An Overview

The northern segment of the North–South Seismic Belt is characterized by a complex network of major fault systems, including the Arjin Fault, Liupanshan Fault, Helan Mountain East Slope Fault, West Qinling Fault, Zhuanglanghe Fault, Northern Edge Fault of the Qilian Block, Haiyuan Fault, and East Kunlun Fault [16]. The tectonic pattern of the study area can be divided into two parts: the central–southern region comprises an arc-shaped structural belt along the northeastern margin of the Tibet Plateau, formed by a series of left-lateral arc faults and thrust faults, including the Qilian–Haiyuan Fault, Xiangshan–Tianjingshan Fault, and Sanguguan–Niushoushan Fault; the northern region consists of a basin mountain structure composed of the Yinchuan Sag Basin and the Helan Mountains, controlled by multiple normal faults [3,6,17–25]. The regional principal compressive stress direction is oriented approximately perpendicular to the local tectonic boundaries. The northeastward thrust of the Indian Plate, coupled with the westward obstruction posed by the Ordos Block, the lateral sliding of the Alxa Block, and the obstructive effects emanating from the Tarim Basin, collectively impose regional dynamic constraints, predominantly obstructive in nature, upon the northeastern margin of the Tibetan Plateau. GNSS observation data further indicate that intense compression along the northeast direction constitutes the primary dynamic source within the study area [26]. The northeastern margin of the Tibet Plateau is primarily subjected to NEE-oriented compressional stress, giving rise to right-lateral strike-slip faults, with their southeastern segments exhibiting crustal thrusting characteristics. The central part of the study area experiences NNE-oriented compressional stress, resulting in left-lateral movement. Seismic displacement in the northern study area is dominated by strike-slip motion. Specifically, compressional stress is distributed near the north–south trending axis in the Alxa region, as well as along the northeast-oriented tectonic domain within the Yinchuan Graben and its adjacent northern areas. The Yinchuan Graben demonstrates tensional structural features, whereas the Haiyuan Fault Zone exhibits predominant compressional structural characteristics [27].

Existing studies show that the Qilian Fault and the Maomaoshan–Hushan Fault in the study area present a high degree of structural coupling, indicating that these faults are associated with considerable medium- and long-term strong earthquake hazard; the Haiyuan Fault shows a relatively low degree of structural coupling, while the Liupanshan Fault maintains persistent and clear locking characteristics. The Haiyuan Fault Zone extends from Xingquanbao, Jingtai County, Gansu Province in the west to Shaokou, Ningxia in the east, with Haiyuan acting as the segmentation boundary. The western segment of the fault zone strikes WNW, while the strike of the eastern segment shifts to NW, and the fault zone connects to the Liupanshan Fault Zone on the southeast side [1,28–31]. The Liupanshan Fault Zone generally strikes NNE, and its southern margin is connected to the Longxian–Baoji Fault Zone [21,32,33]. Existing studies on tectonic activity indicate that the Haiyuan Fault Zone has undergone two tectonic evolution stages of thrusting and subsequent strike-slip movement (since the Late Cenozoic [34]. The middle segment of the Haiyuan Fault Zone is characterized by prominent strike-slip faulting; at its southern termination in the Madongshan area, where it obliquely intersects the Liupanshan Fault Zone, thrust structures and fold deformation are well developed, and crustal shortening constitutes the dominant mechanism for this transformation and strain absorption process [34]. The deep electrical structure derived from continental electromagnetic profiling reveals that the crustal fracture and deformation zone in the Longzhong Basin tectonic domain on the northwestern side of the Haiyuan Fault Zone exhibits consistent anomalous geophysical characteristics, which indicates that this region bears high seismic hazard potential [21,34]. Existing studies based on the GNSS velocity field confirm that the slip rate of the western segment of the Haiyuan Fault Zone is 4–5 mm/a, while the slip rate of its

terminal segment is 1–3 mm/a. Current research shows that the intersection region between the Haiyuan Fault and the Liupanshan Fault Zone is in a high locking state [6,22,24,33,35,36]. Seismic focal mechanism analysis indicates that the Haiyuan Fault, Xiangshan–Tianjingshan Fault, and Yantonghan Fault are dominated by compression-torsion deformation; the Yellow River Fault is mainly characterized by extensional deformation; and the West Qinling Fault also presents compression-torsion deformation. From the perspective of fault activity patterns, the area south of the Xiangshan–Tianjingshan Fault has maintained an overall south–southeast trending motion since the Early Quaternary, while the Yinchuan Basin and the eastern margin of the Yellow River Fault show southeast trending motion [37].

3. The GNSS Velocity Field in the Northern Section of the China North–South Seismic Belt

Figure 2 presents the fault distribution and urban spatial layout of the northern segment of the North–South Seismic Belt, which clearly characterizes the strike and extension range of major active faults in the study area, providing fundamental geographic support for subsequent tectonic risk assessment. The Global Navigation Satellite System (GNSS) offers critical technical support for obtaining high-precision crustal deformation observation data, characterizing surface deformation processes during geotectonic evolution, and revealing the dynamic driving mechanism of environmental change and disaster development [38]. The conceptual schemes including "integrated monitoring, research and prediction", "step-by-step promotion with process as the core", and "based on deformation dynamic characteristics, focusing on seismotectonic background, consolidating geophysical–mechanical basis, and improving real-time tracking and assessment capabilities" are specialized approaches put forward for large-scale crustal deformation monitoring [39]. The Chinese Mainland Structural Environment Monitoring Network (hereafter abbreviated as the "Land State Network", CMTEMN for short) is currently the largest scientific research program in China that applies GNSS technology to the geoscience field. The velocity field data adopted in this study were provided by the Institute of Geology, China Earthquake Administration, with a sampling interval of 30 s. For the reference stations deployed in the network, the long-term repeatability root mean square errors in the north–south direction and the east–west direction do not exceed 2.6 mm and 2.9 mm, respectively. The root mean square errors of the daily solution coordinates are 2 mm in the horizontal direction and 5 mm in the vertical direction, respectively. After adjustment processing, the horizontal root mean square errors of the velocity fields obtained from fixed stations and mobile stations are lower than 0.5 mm/a and 1 mm/a, respectively. To eliminate the interference of seismic activities on observation results, this study removes the co-seismic displacement effect of earthquakes with magnitude ≥6 from the acquired velocity field [40]. Figure 3 exhibits the active tectonic framework and spatial distribution of historical earthquakes ($M \geq 6.0$) in the northern segment of the North–South Seismic Belt. From the perspective of long-term geological evolution, this characterization clarifies the regional tectonic activity pattern of the study area since the Quaternary and provides solid geological constraints for the subsequent analysis of GNSS observation data. The 1998–2024 crustal velocity field dataset constructed in this study is broadly consistent with the well-confirmed long-term tectonic stress background of the study area [41].

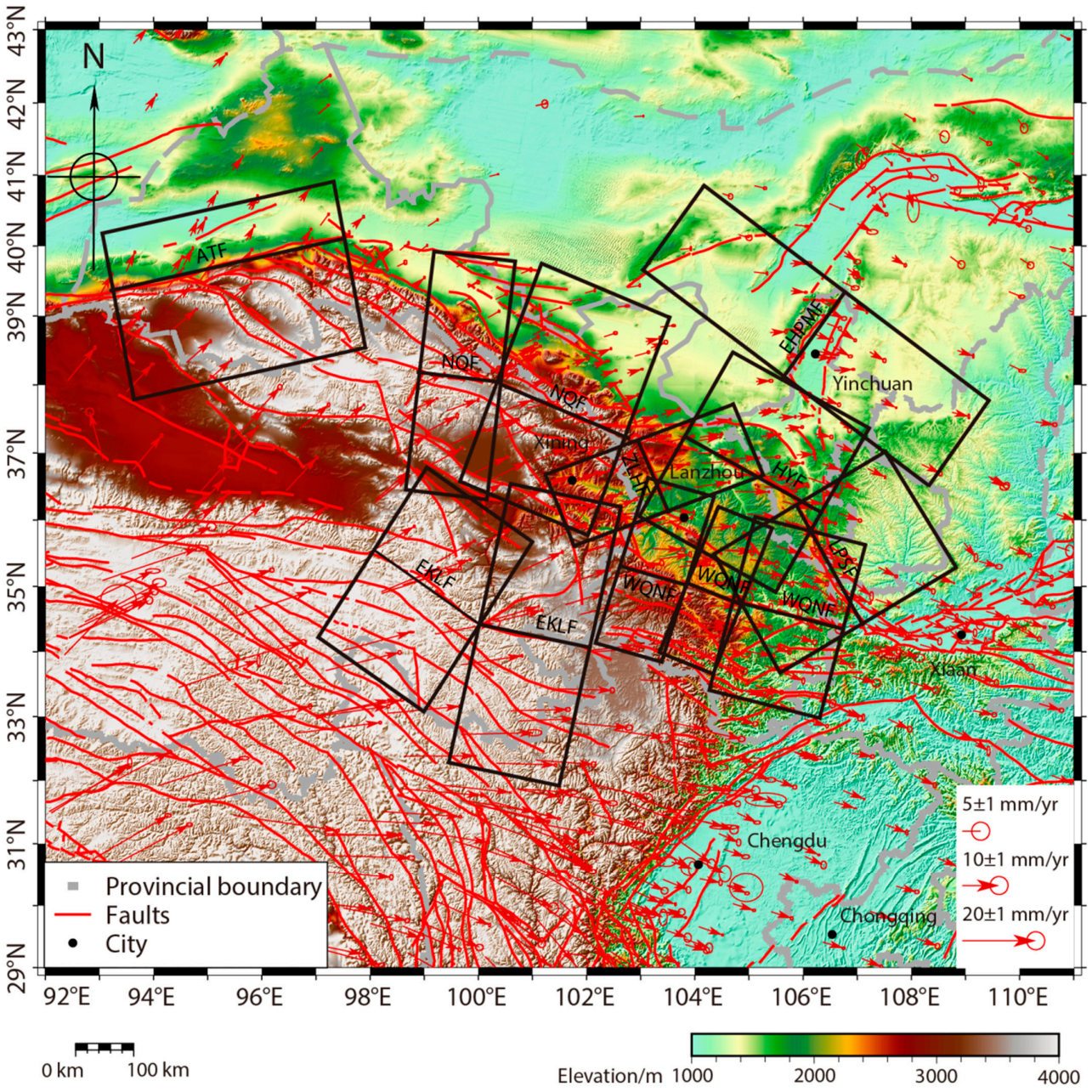


Figure 2. The spatial distribution of GNSS stations involved in velocity projection, with the 1998–2024 GNSS velocity field as the background. Black rectangles mark the GNSS stations used for velocity projection of active faults, and the fault abbreviations are defined as follows: ATF—Aljin Fault; NQF—Northern Qilian Mountain Fault; WQNF—Northern Western Qinling Mountain Fault; EKLF—East Kunlun Fault; HYF—Haiyuan Fault; LPSF—Liupanshan Fault; ZLHF—Zhuanglanghe Fault; EHPMF—Eastern Helan Mountain Fault.

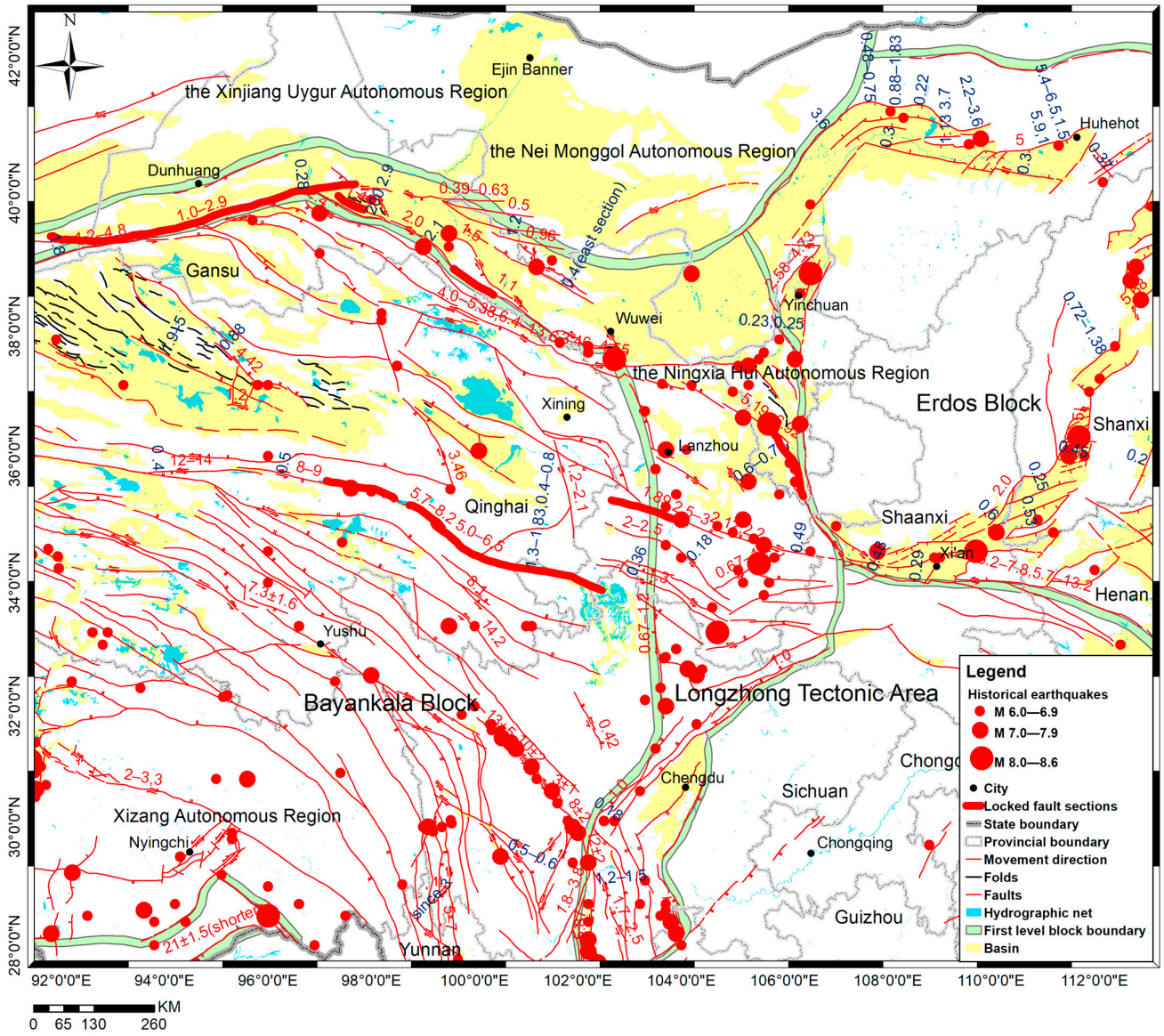


Figure 3. Geological Structure and historical earthquakes greater than M 6.0 of the northern segment of the North–South Seismic Belt.

Figure 1 illustrates the tectonic driving mechanisms of the Qinghai–Tibet Block over the northern study area. The movement rates in the eastern part of the Aljin Fault Zone and the southwestern margin of the Alxa Block remain low, while the Yinchuan Basin exhibits sustained extensional deformation with accelerated crustal material outflow between the Alxa and Ordos Blocks. Movement intensity has decreased at most GNSS stations, particularly in the Qilian and Liupan Mountain regions: left-lateral shear activity along the Qilian and Liupan Faults has weakened, whereas compressional forces have intensified; the magnitude of the principal compressive stress along the West Qinling Fault has decreased; and the fault movement rates along the northern margin of the Qilian Mountains have decelerated, while the expansion rate of the Yinchuan graben has exhibited an accelerating trend. Figure 2 shows the spatial distribution of the GNSS velocity field in the northern segment of the North–South Seismic Belt from 1998 to 2024, and illustrates the spatial coverage of GNSS stations involved in velocity field projection. By decomposing the station velocities into the components parallel and perpendicular to

fault strikes, observation constraints can be provided for quantitative analysis of fault zone slip rates and crustal deformation characteristics.

In this study, we calculated the vertical and horizontal projection rates of GNSS stations distributed on both sides of major active faults in the northern segment of the North–South Seismic Belt during the observation period and further determined the contemporary slip rates of the aforementioned active faults. The specific calculation workflow is as follows: first, the mean values of vertical and fault-parallel velocity projections of GNSS stations within the fault projection zone are obtained; the difference between the two mean values is defined as the estimated slip rate of the target fault (right-lateral slip in the parallel direction is specified as positive, and left-lateral slip as negative; vertical compression is specified as positive, and tension as negative). The absolute value of this difference corresponds to the dip-slip rate and strike-slip rate of the fault, respectively (Table 1). The black box in Figure 2 delineates the distribution range of GNSS stations used for active fault velocity projection calculation.

Based on the velocity projection results obtained from GNSS observation data covering the period 1998–2024, this study acquired the slip rate characteristics of major active faults in the northern segment of the North–South Seismic Belt. Along the eastern segment of the Aljin Fault, the measured vertical slip rates are 2.3 mm/a and 3.2 mm/a, and the fault-strike-parallel slip rates are 6.6 mm/a and 4.7 mm/a. For the western boundary of the northern Qilian Block, the vertical slip rates are 2.7 mm/a and 3.2 mm/a, corresponding to parallel slip rates of 8.2 mm/a and 5.1 mm/a; for the eastern boundary of this region, the vertical slip rates are 8.2 mm/a and 6.2 mm/a, with parallel slip rates of 8.1 mm/a and 6.5 mm/a. For the Zhuanglanghe Fault, the vertical slip rates are 9.0 mm/a and 8.6 mm/a, matching parallel slip rates of 3.3 mm/a and 7.7 mm/a; for the Haiyuan Fault, the vertical slip rates are 1.4 mm/a and 2.0 mm/a, corresponding to parallel slip rates of 8.6 mm/a and 8.3 mm/a; along the Liupanshan Fault, the vertical slip rates are 3.7 mm/a and 5.5 mm/a, with parallel slip rates of 6.7 mm/a and 7.8 mm/a; and for the western segment of the Northern Western Qinling Mountain Fault Zone, the vertical slip rates are 5.2 mm/a and 5.9 mm/a, accompanied by parallel slip rates of 10.1 mm/a and 7.0 mm/a. At the observation stations along the middle segment of the northern margin fault zone of the Western Qinling Mountains, the vertical slip rates are 2.7 mm/a and 3.1 mm/a, respectively, while the parallel slip rates are 8.0 mm/a and 6.5 mm/a, respectively. At the observation stations along the eastern segment of the aforementioned fault zone, the vertical slip rates are 0.3 mm/a and 0.6 mm/a, with the parallel slip rates measured at 8.5 mm/a and 8.2 mm/a, respectively.

The middle-eastern segment of the Aljin Fault Zone is dominated by weak thrust-slip movement. The cumulative shear strain rate of the Kuantan Mountain section in Subei is significantly higher than the cumulative compressional strain rate, indicating that the tectonic activity of this segment is currently in a quiescent state. As the northern boundary of the Qilian Block, the northern margin fault of the Qilian Mountains maintains relatively high tectonic activity. From the perspectives of geometry and kinematics, the western segment of the fault is characterized by intense left-lateral strike-slip motion, while the eastern segment is dominated by active reverse strike-slip motion. The Zaoxia–Yumen segment presents the characteristic of low compressive strain accumulation, while the Fodongmiao–Sunan segment displays significant accumulation of both shear and compressive strain. For the central segment of the northern Qinling Fault Belt, the left-lateral strike-slip movement is relatively faint, and the eastern segment is most likely in a stress-locking state. Along the Tianshui segment of the northern Qinling Fault, the slip rate parallel to the fault strike on the southern side of the fault is higher than that on the northern side, with a variation interval of 6.0–10.0 mm/a. No statistically significant difference in horizontal or vertical slip rates is detected between the two sides of the Ma'gotan segment,

which indicates that the fault movement in this section is nearly quiescent. The Tianshui segment is characterized by continuous compressive deformation, with stable strain accumulation and relatively weak shear strain. Both the Luafeng and Tanxian segments show moderate accumulation of compressional and shear strain. It is inferred that the Haiyuan Fault is in a stress-locking state, with weak left-lateral shear strain accumulation accompanied by a certain degree of compressional strain accumulation. The Liupanshan Fault is inferred to be in a stress-locking state, with tectonic activity remaining nearly quiescent and characterized by weak accumulation of both shear strain and compressional strain. The Zhuanglanghe Fault exhibits significant strong left-lateral strike-slip activity, and no additional anomalous stress features have been detected. For the Kusai Lake segment, Dongditan segment, and Xiugou–Alak Lake segment of the Eastern Kunlun Fault, the vertical movement rate on the southern side of the fault is higher than that on the northern side in the direction perpendicular to the fault strike. The western segment of the Northern Margin Fault of the Eastern Kunlun Mountains presents convergent deformation, while the eastern segment is characterized by active strike-slip movement. The vertical velocity difference along the eastern segment of the Eastern Kunlun Fault is not significant, whereas the horizontal velocity variation has slowed to approximately 1 mm/a. The western segment of this fault shows cumulative shear and reverse strain deformation.

Table 1. Slip rates valuation in vertical and parallel direction of main active faults on the northeast margin of Tibet Plateau during 1998–2024 (unit: mm/a).

Fracture Name	The Middle Eastern Section of the ATF	Western Section of the NQF	East Section of the NQF	ZLHF	HYF	LPSF	The Western Section of the WQNF	The Middle Section of the WQNF	The Eastern Section of the WQNF
Dip-slip rate	0.45	1.33	6.60	0.61	0.55	0.02	0.62	2.09	0.77
strike-slip rate	3.06	4.61	7.29	2.06	1.70	0.92	1.34	0.93	0.33

To verify the representativeness of the 1998–2024 GNSS dataset for evaluating the documented historical maximum crustal uplift, this paper first clarifies the temporal coverage and geodetic data quality of the observations utilized in this research. The GNSS network covering the study area has realized full continuous operational coverage since 1998, with inter-station spacing ranging from 15 km to 40 km, which meets the resolution requirement for regional crustal deformation at the tectonic scale relevant to seismic hazard assessment. The long-term GNSS time series are processed via standardized geodetic models to correct for solid Earth tides, ocean tidal loading, atmospheric delay, and non-tectonic seasonal deformation, yielding an uncertainty of annual uplift rate estimation of less than 0.2 mm/a. This precision is adequate to identify long-term uplift rate anomalies relative to the centennial background deformation derived from leveling and paleoseismic data.

Although the 26-year GNSS observation period is shorter than the millennial-scale recurrence interval of large tectonic earthquakes, modern GNSS observations can capture the most recent crustal deformation state immediately prior to potential large seismic events, which provides a more robust constraint on current seismic hazard levels compared with sparse or outdated historical observations. Given that the uplift rate anomaly identified in this study exceeds all cumulative uplift values recorded in historical observation datasets (including leveling surveys conducted from 1950 to 1997 and paleogeodetic measurements over the past 500 years), this study confirms that the current anomaly has reached the historical maximum in the recorded deformation history of the study region.

4. The Strain Rate Field in the Northern Section of the China North–South Seismic Belt

The geodetic velocity field provides an intuitive and quantitative method to characterize the tectonic motion of tectonic plates and crustal blocks. To eliminate crustal deformation disturbances induced by earthquakes with magnitude ≥ 6.0, this study first extracts the co-seismic displacement field generated by these events using continuous Global Navigation Satellite System (GNSS) observation data and deducts this co-seismic displacement component during the calculation of the GNSS velocity field. On this basis, the GNSS-inverted strain rate field for the northern segment of the China North–South Seismic Belt covering 1998–2024 is obtained.

Previous studies have confirmed that crustal strain accumulation is significantly correlated with seismic activity and regional stress concentration [42]. The strain rate field can quantitatively characterize the regional strain accumulation process, and its spatial distribution characteristics can be used to analyze the strain accumulation state and seismic hazard level of different sub-regions [43]. As a dimensionless physical quantity, strain rate can intuitively reflect the intensity and deformation characteristics of regional crustal activities, and its measurement is not restricted by the selection of reference frames [29,31].

This study employs the weighted difference algorithm model [44] and constructs a regular grid with 0.5° spacing within the study area. For each grid point, the strain rate is calculated using velocity observations from no less than four GNSS stations within a 100 km search radius, and grid points with insufficient station coverage are excluded from calculation. Finally, the strain rate contour maps of the northern segment of the China North–South Seismic Belt for 1998–2024 are obtained (Figures 4–7).

In this study, a gridded interpolation approach is adopted to construct the regional strain rate field. Based on velocity observation data from adjacent GNSS stations, the strain rate components at any spatial position are obtained through spatial interpolation. The specific implementation process is as follows: first, a uniform grid with regular spacing is established; second, a search radius is defined with each grid node as the center; third, observation data from no fewer than four GNSS stations within the search radius are screened to complete the strain rate calculation; finally, grid nodes with fewer than four valid GNSS stations within the search radius are excluded from calculation. In this work, the grid spacing is set to 0.5° and the search radius is set to 100 km, and the time-series results of principal strain rate, shear strain rate and areal strain rate covering 1998–2024 are finally obtained.

Based on the observations of the principal strain rate field (Figures 5 and 6), the low principal strain rate zones delineated within the study area exhibit high spatial consistency with the primary low shear strain rate zones, covering the northwestern part of the Alxa Block, the northern and southern termini of the Ordos Block, and the South China Block. The high principal strain rate zones are mainly distributed in the eastern part of the Alxa Block, the central–southern part of the Ordos Block, the eastern part of the Bayan Har Block, the eastern part of the Qiangtang Block, and the southeastern part of the South China Block.

The regional strain field exhibits distinct extensional characteristics: extensional deformation is developed in the eastern part of the Qiangtang Block, the central–eastern part of the Bayan Har Block, the central part of the Qilian Block, the northern part of the Alxa Block, and the central–northern part of the Longzhong Basin tectonic zone, forming well-defined extensional tectonic zones. In contrast, the northern and southern boundaries of the Qilian Block, as well as the western segment of the southern boundary of the Qaidam Block, are dominated by compressional strain. The tectonic strikes of these boundaries are nearly perpendicular to the contour lines of the principal strain rate. The principal strain

rate parameters of each major tectonic belt are statistically summarized as follows: the principal compressive strain rate at the northern boundary of the Qilian Block is −2.6 × 10^{-8}/a; the principal compressive strain rate at the western segment of the southern boundary of the Qaidam Block is −2.3 × 10^{-8}/a; the principal compressive strain rate at the central segment of the southern boundary of the Qaidam Block is −1.6 × 10^{-8}/a. Along the western segment of the northern margin fault zone of the Western Qinling Mountains, the magnitude of the principal extensional strain rate ranges from 0.9 × 10^{-8}/a to 1.6 × 10^{-8}/a, while the principal compressive strain rate ranges from −1.5 × 10^{-8}/a to −1.5 × 10^{-8}/a. Along the Liupanshan Fault Zone, the magnitude of the principal compressive strain rate increases gradually from 0.8 × 10^{-8}/a to 1.6 × 10^{-8}/a. For the Zhuanglanghe Fault, the principal extensional strain rate is 0.9 × 10^{-8}/a, and the principal compressive strain rate is −1.4 × 10^{-8}/a.

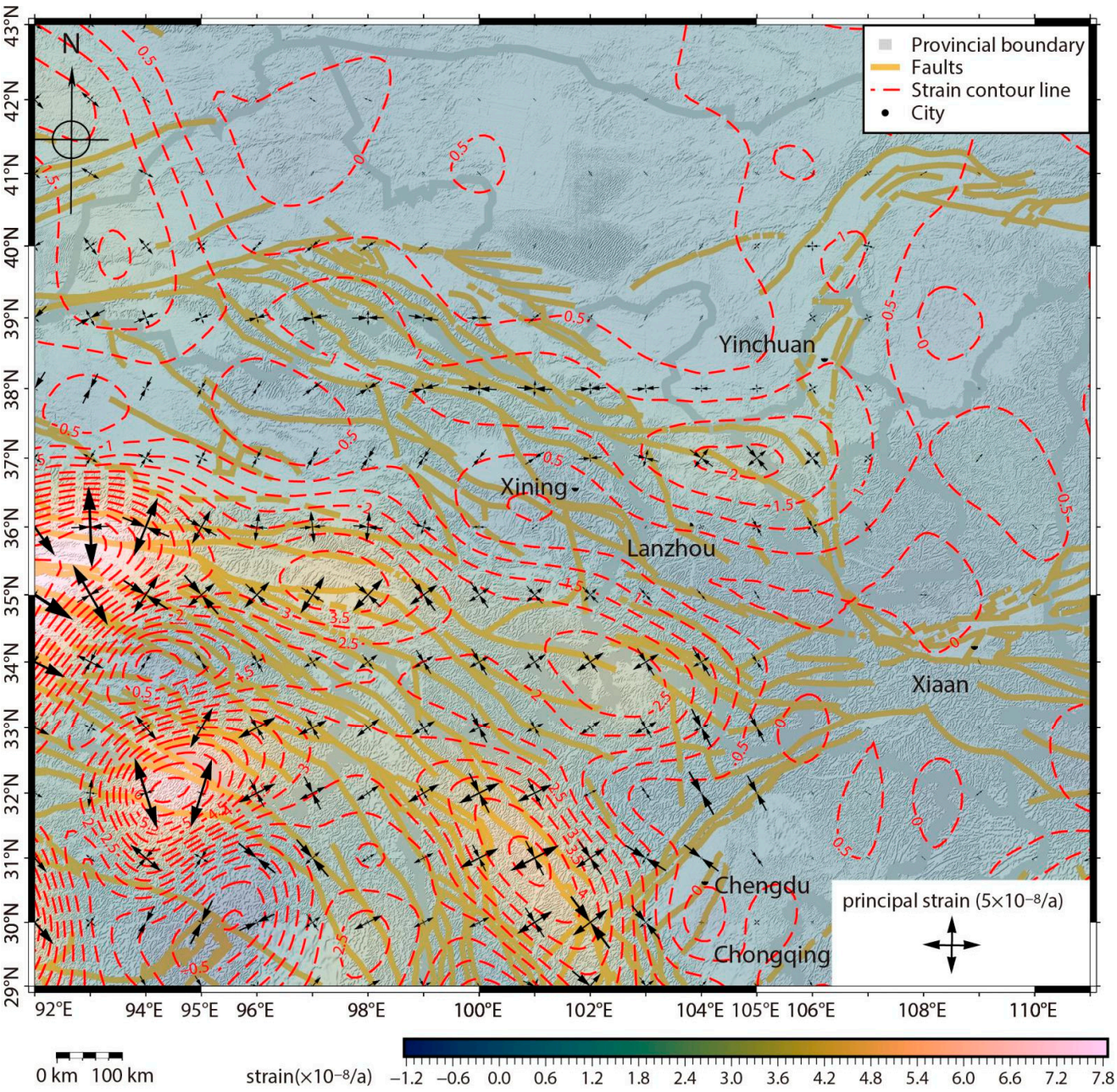


Figure 4. Spatial distribution of crustal strain in the northern segment of the North–South Seismic Belt covering the study period 1998–2024. The magnitude of crustal strain is denoted by gradient

colors (see the attached color bar), and the distribution is plotted on a kilometer-resolution principal strain grid under the ITRF 2014 Eurasian reference frame.

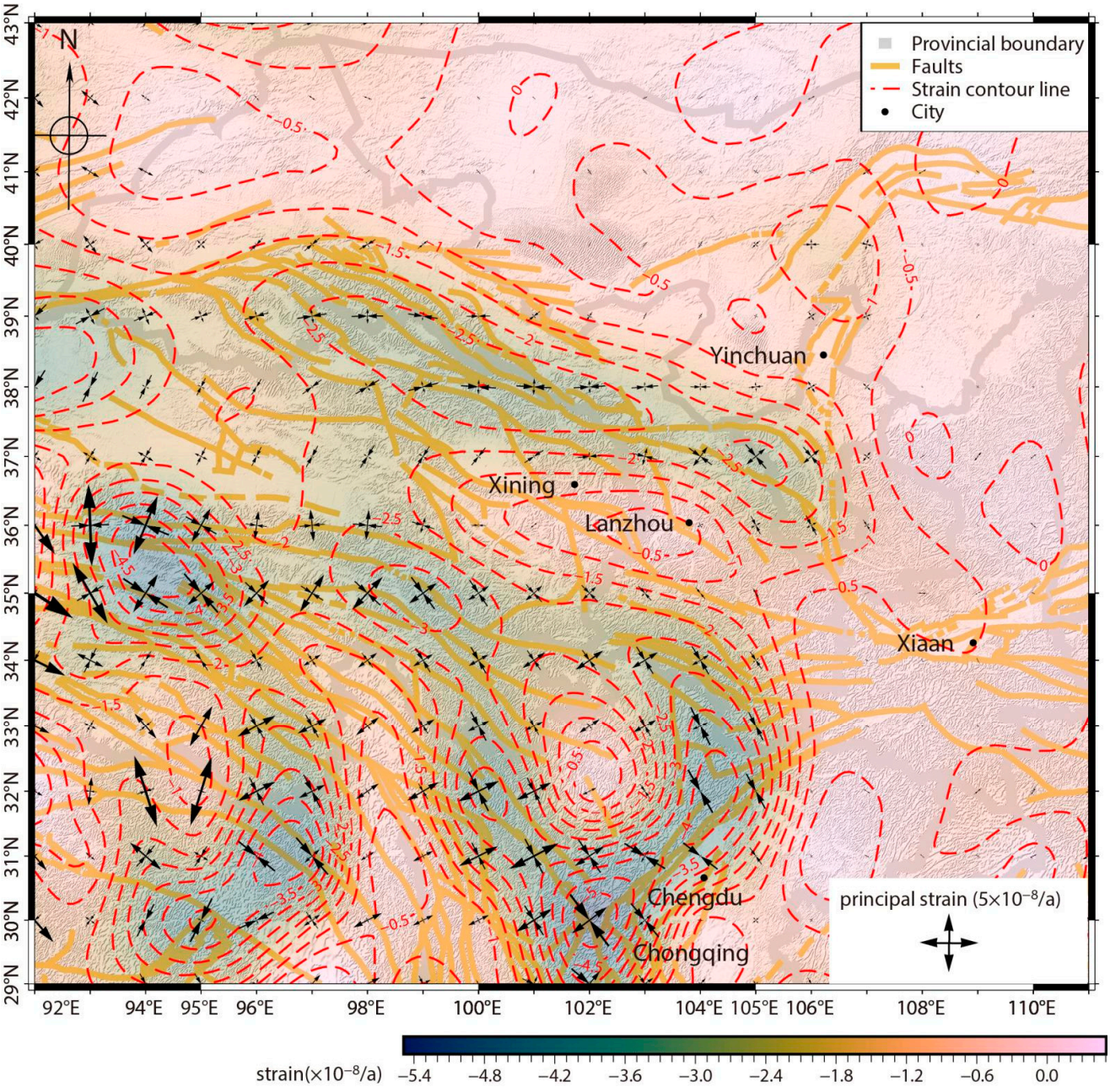


Figure 5. Spatial distribution of the principal compressive stress field in the northern segment of the North–South Seismic Belt over the 1998–2024 study period. The magnitude of the principal compressive stress is denoted by gradient colors (see the attached color bar), and the distribution is plotted on a kilometer-resolution principal strain grid under the ITRF 2014 Eurasian reference frame.

Analysis of observational data indicates that the maximum variation amplitude of strain rate at the Guomatan segment of the northern fault zone of the Western Qinling Mountains is approximately 0.7×10^{-8}/a, demonstrating that the cumulative strain level in this segment is relatively low. Within the Tianshui segment of this fault zone, the extensional strain rate ranges from 0.3×10^{-8}/a to 0.9×10^{-8}/a, while the principal compressive strain rate varies between -1.2×10^{-8}/a and -0.6×10^{-8}/a. This result further confirms the

low-strain characteristic of the study region. Both the eastern segment of the northern fault zone of the Western Qinling Mountains and the eastern piedmont fault of the Helan Mountains strike nearly perpendicular to the isolines of the principal compressive strain rate, with maximum strain rate differences of 0.8 × 10^{-8}/a and 0.5 × 10^{-8}/a, respectively. Both of the aforementioned fault zones are situated within low-strain-rate regions. The western segment of the northern fault zone intersects the principal strain rate isolines at a small angle, with a principal extensional strain rate of 0.8 × 10^{-8}/a and a principal compressive strain rate of −1.5 × 10^{-8}/a, and the isolines in this region are relatively sparse. The principal compressive strain rate of the Subei Kuantan Mountain segment of the Aljin Fault is only −0.4 × 10^{-8}/a.

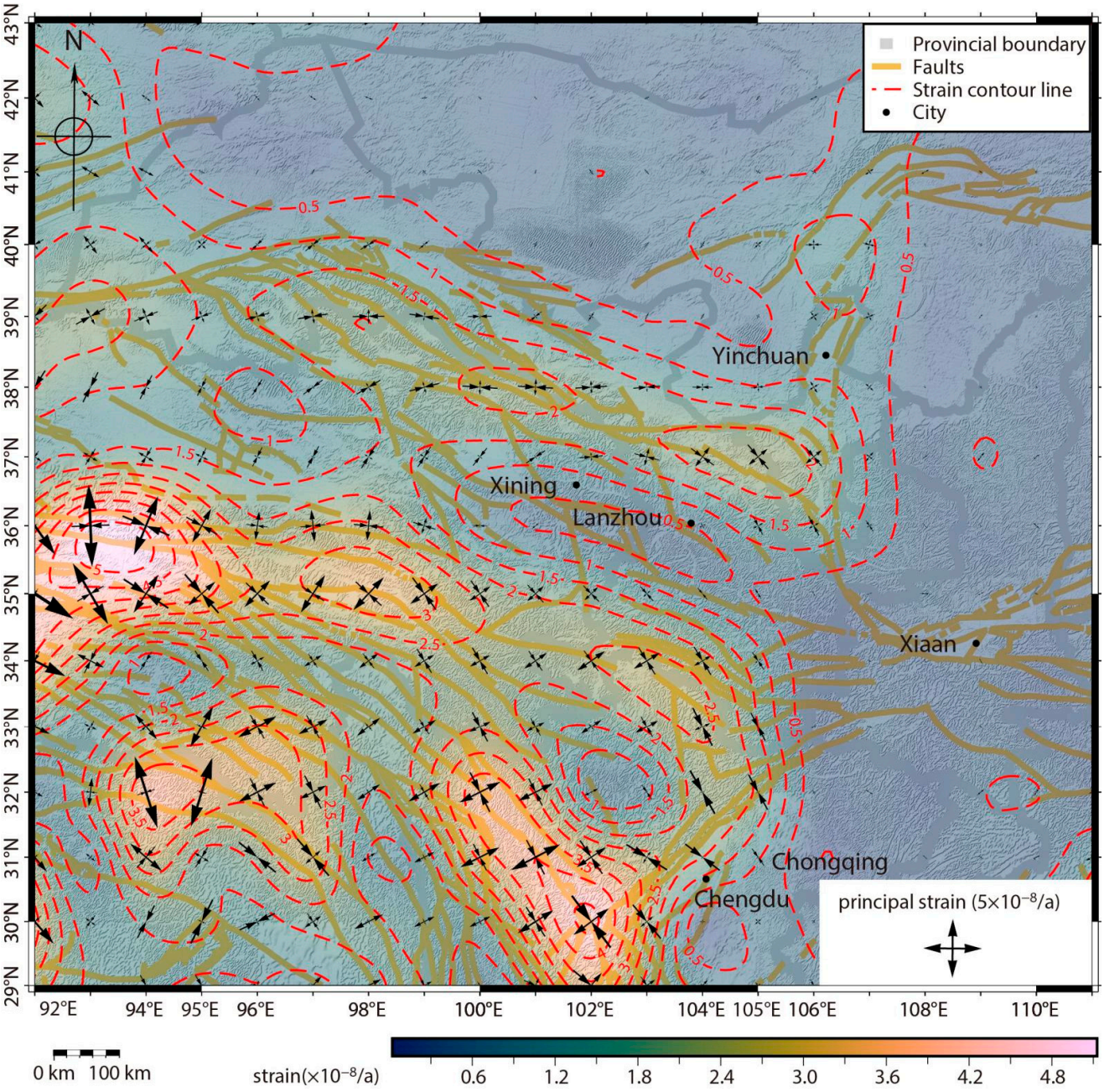


Figure 6. Distribution of the first shear strain in the northern segment of the North–South Seismic Belt. Principal stress values derived from kilometer-resolution grids under the ITRF 2014 Eurasian

reference frame are overlaid, where the background color represents the magnitude of shear strain. This result covers the study period from 1998 to 2024.

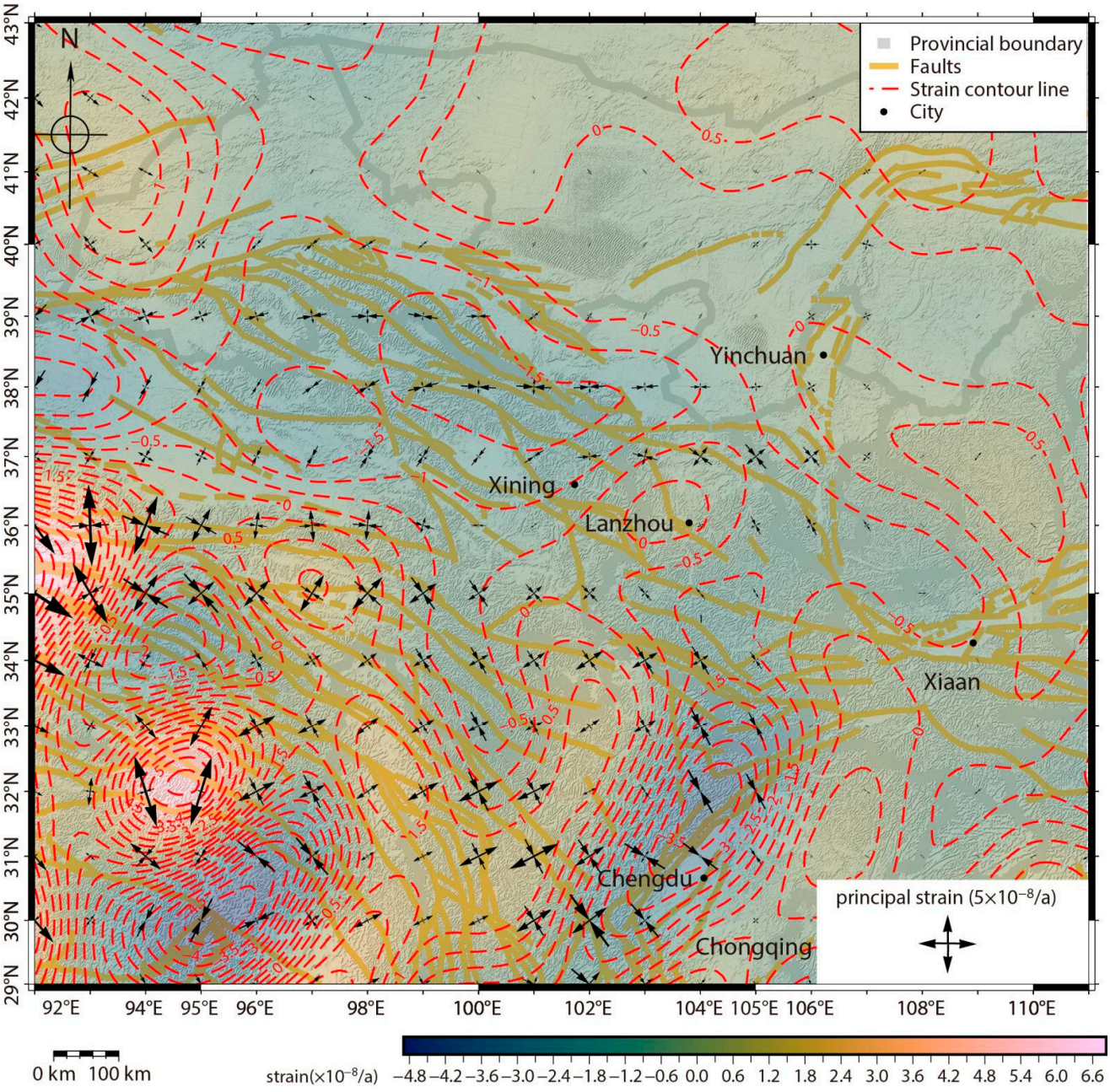


Figure 7. Distribution of shear strain within the northern segment of the North–South Seismic Belt, on which the principal stress values calculated from kilometer-resolution grids under the ITRF 2014 Eurasian reference frame are overlaid. The background color in the figure denotes the magnitude of shear strain, and the result covers the research observation period from 1998 to 2024.

Stress state analysis yields the principal compressive strain rate parameters for each study segment as follows: the eastern segment of the Aljin Fault Zone, −1.5 × 10^{-8}/a to −1.2 × 10^{-8}/a; the eastern segment of the Haiyuan Fault, −1.2 × 10^{-8}/a to −1.5 × 10^{-8}/a; the central–eastern section of the northern boundary of the Qilian Block, −2.6 × 10^{-8}/a to −2.1 × 10^{-8}/a; the western segment of the East Kunlun Fault Zone, −2.5 × 10^{-8}/a to −2.1 × 10^{-8}/a; and the northern segment of the Zhuanglanghe Fault, −1.8 × 10^{-8}/a to −1.5 × 10^{-8}/a. The strikes of

the aforementioned tectonic zones are all parallel to the densely distributed principal compressive strain rate isolines, indicating that stress locking may occur in these regions.

The eastern segment of the Aljin Fault intersects the principal extensional strain rate isolines at a small angle and is parallel to the widely spaced principal compressive strain rate isolines; its principal compressive strain rate is -0.4×10^{-8}/a, which demonstrates that compressive stress locking occurs in the Subei Kuantan Mountain segment of the Aljin Fault. Similar locking characteristics are also identified along the Qilian Mountains northern margin fault zone, the southern boundary of the Qaidam Block, and the central section of the southern boundary of the Qilian Block. The Haiyuan Fault exhibits the characteristic of compressive strain accumulation: it intersects the high-value principal compressive strain rate isolines at a large angle and is parallel to the principal compressive strain rate isolines with large spacing.

The Liupanshan Fault exhibits a low magnitude of compressive strain rate along its entire strike. For the Kusai Lake, Dongditan, and Xiugou–Alak Lake segments of the East Kunlun Fault, the calculated principal strain rate ranges from 1.5×10^{-8}/a to 3.0×10^{-8}/a, and the principal compressive strain rate ranges from -3.0×10^{-8}/a to -2.1×10^{-8}/a. This result indicates that the western segment of the East Kunlun Fault is characterized by compressive strain accumulation. For the Alak Lake–Tuosuo Lake segment and the Tuosuo Lake–Maqu segment, the calculated principal strain rate ranges from 1.2×10^{-8}/a to 2.1×10^{-8}/a, and the principal compressive strain rate ranges from -2.4×10^{-8}/a to -1.5×10^{-8}/a, which confirms the existence of compressive stress locking in the eastern segment of the East Kunlun Fault. The Hoh Xil region presents clear compressive strain accumulation, and this region intersects both the principal strain rate isolines and the principal compressive strain rate isolines at large angles, with large spacing between adjacent isolines. The Zhuanglanghe Fault intersects the principal strain rate isoline at a small angle, and is nearly perpendicular to the principal compressive strain rate isoline. According to the observational data obtained in this study, the calculated principal strain rate of this fault is 0.9×10^{-8}/a, and its principal compressive strain rate is -1.4×10^{-8}/a. The Dongkunlun Fault, which is distributed along the eastern section of the southern boundary of the Qaidam Block, has a small intersection angle with the principal strain rate isoline in its western segment that is situated within the high-value strain rate zone, and intersects the principal compressive strain rate isoline at a large angle. In this segment, the calculated principal strain rate is 1.5×10^{-8}/a and the principal compressive strain rate is -2.3×10^{-8}/a. The eastern segment of the Dongkunlun Fault is nearly perpendicular to the principal strain rate isoline and intersects the principal compressive strain rate isoline at a small angle, with calculated principal strain rates ranging from 1.6×10^{-8}/a to 2.0×10^{-8}/a and principal compressive strain rates ranging from -1.8×10^{-8}/a to -2.4×10^{-8}/a. Furthermore, the isolines in this segment are characterized by large spacing. The Liupanshan Fault is perpendicular to the low-value strain rate isoline zone and intersects the principal compressive strain rate isoline at a large angle. Along the fault strike, the magnitude of the compressive strain rate increases gradually from 0.8×10^{-8}/a to 1.5×10^{-8}/a. The narrow spacing of the isolines indicates a low level of cumulative compressive stress accumulation, which is consistent with the conclusion reported by Xu W et al. [45]. Through comprehensive analysis, it can be concluded that multiple tectonic units and fault zones, including the northern and southern boundaries of the Qilian Block, the western segment of the southern boundary of the Qaidam Block, the eastern segment of the Aljin Fault, the Haiyuan Fault, the eastern segment of the East Kunlun Fault, and the Hoh Xil region, all present relatively significant compressive stress accumulation characteristics.

Based on the shear strain rate field obtained in this study (Figure 6), high-shear-strain rate regions (1.6×10^{-8}/a–2.5×10^{-8}/a) are predominantly distributed along the boundary between the Qilian Block and the Alxa Block, the southern region of the Qaidam Block,

the central–eastern portion of the Bayan Har Block, and the eastern region of the Qiangtang Block. This spatial distribution pattern is consistent with the previous research results [46]. The shear strain rate characteristics of the main tectonic units and fault zones are summarized as follows:

The shear strain rate of the central–eastern segment of the Aljin Fault Zone is measured as 0.7×10^{-8}/a, and the Suběikuangtanshan section of the fault also yields a shear strain rate of 0.7×10^{-8}/a, indicating that strain accumulation within this section is relatively weak. The fault strike is nearly parallel to the isopleths of shear strain rate.

The overall shear strain rate at the northern boundary of the Qilian Block ranges from 1.6×10^{-8}/a to 1.8×10^{-8}/a, while the shear strain rates of the western and eastern segments fall between 1.5×10^{-8}/a and 1.8×10^{-8}/a. The overall fault strike intersects the shear strain rate isopleths at a large angle, and the isopleths are characterized by wide spacing.

The North Qilian Margin Fault, corresponding to the northern boundary of the Qilian Block, forms a high shear strain rate zone at its junction with the Alxa Block, with a shear strain rate ranging from 1.2×10^{-8}/a to 1.5×10^{-8}/a and exhibits the characteristic of strike-slip locking.

The strike of the Zhuanglanghe Fault intersects the shear strain rate isopleths at a large angle, with relatively wide spacing between adjacent isopleths, and the shear strain rate of this fault ranges from 1.2×10^{-8}/a to 1.4×10^{-8}/a.

The eastern segment of the North Western Qinling Margin Fault is perpendicular to the low-density shear strain rate isopleths, with its shear strain rate ranging from 0.3×10^{-8}/a to 1.2×10^{-8}/a. Under the obstruction of the South China Block, this fault segment exhibits strike-slip locking. The eastern segment of the Haiyuan Fault has a shear strain rate of 0.9×10^{-8}/a–1.3×10^{-8}/a, which falls within the overall range of 1.2×10^{-8}/a–1.4×10^{-8}/a. This fault segment is located between the 1.2×10^{-8}/a–1.4×10^{-8}/a isopleths with relatively large spacing, and its strike is perpendicular to these isopleths. The shear strain rate of the northern segment of the Liupanshan Fault varies from 0.3×10^{-8}/a to 1.2×10^{-8}/a, with the overall value falling within the interval of 0–1.5×10^{-8}/a, indicating a low level of strain accumulation. For the southern segment of the East Helan Piedmont Fault, the shear strain rate ranges from 0.6×10^{-8}/a to 1.2×10^{-8}/a, and its strike is perpendicular to the low-value contour lines corresponding to the 0.4×10^{-8}/a–1.2×10^{-8}/a strain interval. Both the northern segment of the Liupanshan Fault and the southern segment of the East Helan Piedmont Fault are located within this low-value contour zone, reflecting that stress accumulation in these segments is weak.

The shear strain rates of the middle and western segments of the Eastern Kunlun Fault Zone range from 1.5×10^{-8}/a to 2.1×10^{-8}/a, (among which the shear strain rate of the western segment is 1.8×10^{-8}/a–2.1×10^{-8}/a). The strike of these segments intersects the high-value contours of shear strain rate at a small angle, and the contours in this region are densely distributed. In the eastern segment of the Eastern Kunlun Fault Zone, the fault strike forms a certain included angle with the shear strain rate isoclines, and the relatively large spacing of isoclines indicates the development of active strike-slip locking. The Kekexili region exhibits low cumulative shear strain, and the included angle between fault strike and shear strain rate isoclines is small.

For key fault zones including the eastern segment of the Western Qinling North Edge Fault, the eastern segment of the Haiyuan Fault, the northern segment of the Liupanshan Fault, the middle and western segments of the Eastern Kunlun Fault Zone, the western and eastern segments of the northern boundary of the Qilian Block, and the southern segment of the Helan Mountain East Slope Fault, their strikes are all perpendicular to the densely distributed isoclines of maximum shear strain rate, which implies that stress locking mechanisms may have developed in these regions. The northern boundary of the Qilian Block, the Zhuanglanghe Fault, the eastern segment of the Eastern Kunlun Fault, the

eastern segment of the Western Qinling North Edge Fault, and the Haiyuan Fault all exhibit the characteristics of strike-slip stress accumulation.

In the Qilian Block, the eastern Qaidam Block, and the central Longzhong Basin tectonic zone, the density of shear strain rate isoclines is relatively low, the variation amplitude of maximum shear strain is small, and the minimum shear strain presents a decreasing trend. This indicates that shear stress accumulation is increasing in the periphery of the Haiyuan Fault, the Liupanshan Fault and the Western Qinling North Edge Fault. The variation range of the principal compressive strain rate covers the entire variation interval of the maximum shear strain rate. In addition, the density of the principal compressive strain rate isoclines decreases in the Qiangtang Block and the south–central Bayan Har Block.

As shown in Figure 7, the overall variation in regional surface strain is not significant.

5. The Dynamic Strain Rate Field Within the Sub-Blocks of the Secondary Level Block

Active blocks refer to geological tectonic units formed from the Late Quaternary (100,000–120,000 years ago) to the present, which are partitioned by active tectonic belts and characterized by relatively uniform intra-block motion. On the Chinese mainland, more than 52% of M6.0 earthquakes, over 73% of M7.0 earthquakes, and 100% of M8.0 earthquakes have occurred along the boundary tectonic zones of first-order and second-order active blocks. Ma Jin argues that the perspective for analyzing seismic activity in China should shift from focusing on active faults to centering on active blocks [47].

Based on the boundary orientation of secondary blocks along the northeastern margin of the Tibet Plateau (Figure 8), the direction of active fault structures [48], and the spatial distribution characteristics of Global Navigation Satellite System (GNSS) stations within these blocks, we further subdivided them into sub-blocks. Using velocity data from GNSS stations within each sub-block between 1998 and 2024, we calculated their strain rates and corresponding mean errors. The classification criteria were as follows: For blocks with irregular geometric morphology, secondary active faults are adopted as block boundaries as far as possible. On this basis, the relative uniformity of GNSS station distribution within adjacent sub-blocks is guaranteed, and the difference in spatial station density is fully considered. For blocks where stations are generally sparse and concentrated at the edges, no further subdivision is implemented, which is exemplified by the Ordos Block. After the completion of sub-block subdivision, multi-temporal velocity field analysis of GNSS stations within each sub-block is conducted to obtain the time-series variation characteristics of strain rates. The strain parameters of all sub-blocks in the northern segment of the North–South Seismic Belt covering the period from 1998 to 2024 are summarized in Figure 9.

Taking the year 1998, when the GNSS Land State Network entered official operation, as the reference epoch, the strain rate analysis results obtained for each study area are presented below:

The strain rate parameters of each sub-region within the Longzhong Basin tectonic zone exhibit significant spatial heterogeneity. In the northern area north of the eastern foothills of the Helan Mountains, the maximum shear strain rate reaches 4×10^{-8}/a, and both the dilatation strain rate and the surface strain rate are measured as 3×10^{-8}/a. In the northern region adjacent to the Haiyuan Fault, the maximum shear strain rate is 3×10^{-8}/a. In the southern area adjacent to the northern marginal fault zone of the Qinling Mountains, the maximum shear strain rate is 5×10^{-8}/a. In the southern section bordering the eastern boundary of the Bayan Har Block, the maximum shear strain rate, the first shear strain rate, the dilatation strain rate and the surface strain rate are 7×10^{-8}/a, 6×10^{-8}/a, 6×10^{-8}/a

and 4 × 10⁻⁸/a, respectively. In the western area adjacent to the Aljin Fault Zone, the maximum shear strain rate is 3 × 10⁻⁸/a, while in the area adjacent to the Zhuanglanghe Fault, the maximum shear strain rate reaches 4 × 10⁻⁸/a. Further subdivided regional analysis yields the following results: the maximum shear strain rate in the southern part of the northern segment is 5 × 10⁻⁸/a; the maximum shear strain rate in the southern part of the southern segment is 7 × 10⁻⁸/a, with the first shear strain rate and the dilatation strain rate both being 6 × 10⁻⁸/a, the NE-oriented strain rate being 5 × 10⁻⁸/a, and the surface strain rate being 4 × 10⁻⁸/a; the maximum shear strain rate in the western part of the western segment is 3 × 10⁻⁸/a; and the maximum shear strain rate in the eastern part of the western segment is 4 × 10⁻⁸/a. Overall, the strain intensity of each sub-region has remained in the normal-to-low range since 1998.

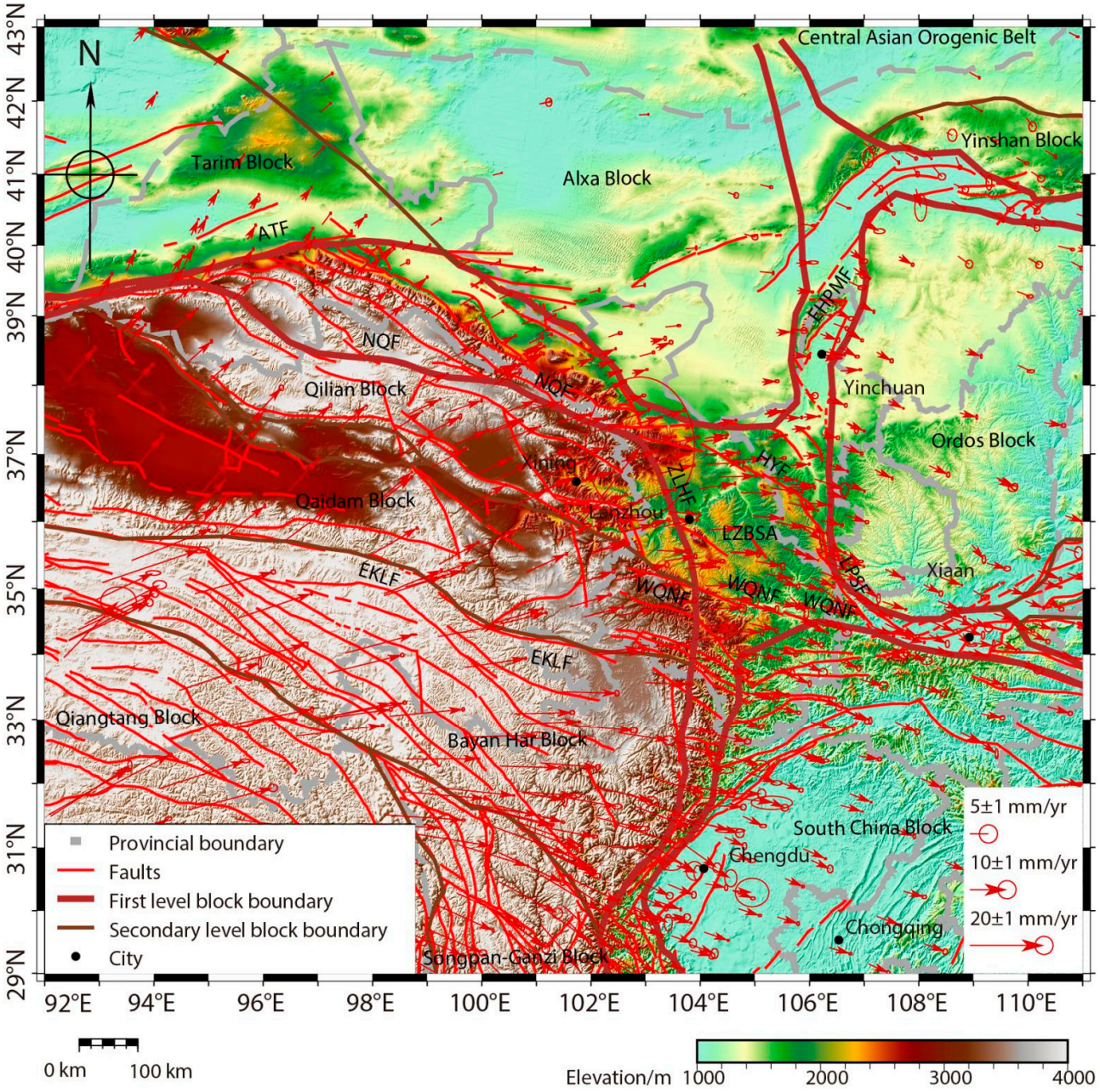


Figure 8. Secondary level block in the northeastern margin of Tibet Plateau (Abbreviations: ATF—Aljin Fault; NQF—Northern Edge Fault of Qilian Mountains; WQNF—Northern Edge Fault of

Western Qinling Mountains; EKLF—East Kunlun Fault; HYF—Haiyuan Fault; LPSF—Liupanshan Fault; ZLHF—Zhuanglanghe Fault; EHPMF—Eastern Foot Fault of Helan Mountains; LZBSA: The structural region of the Longzhong Basin.

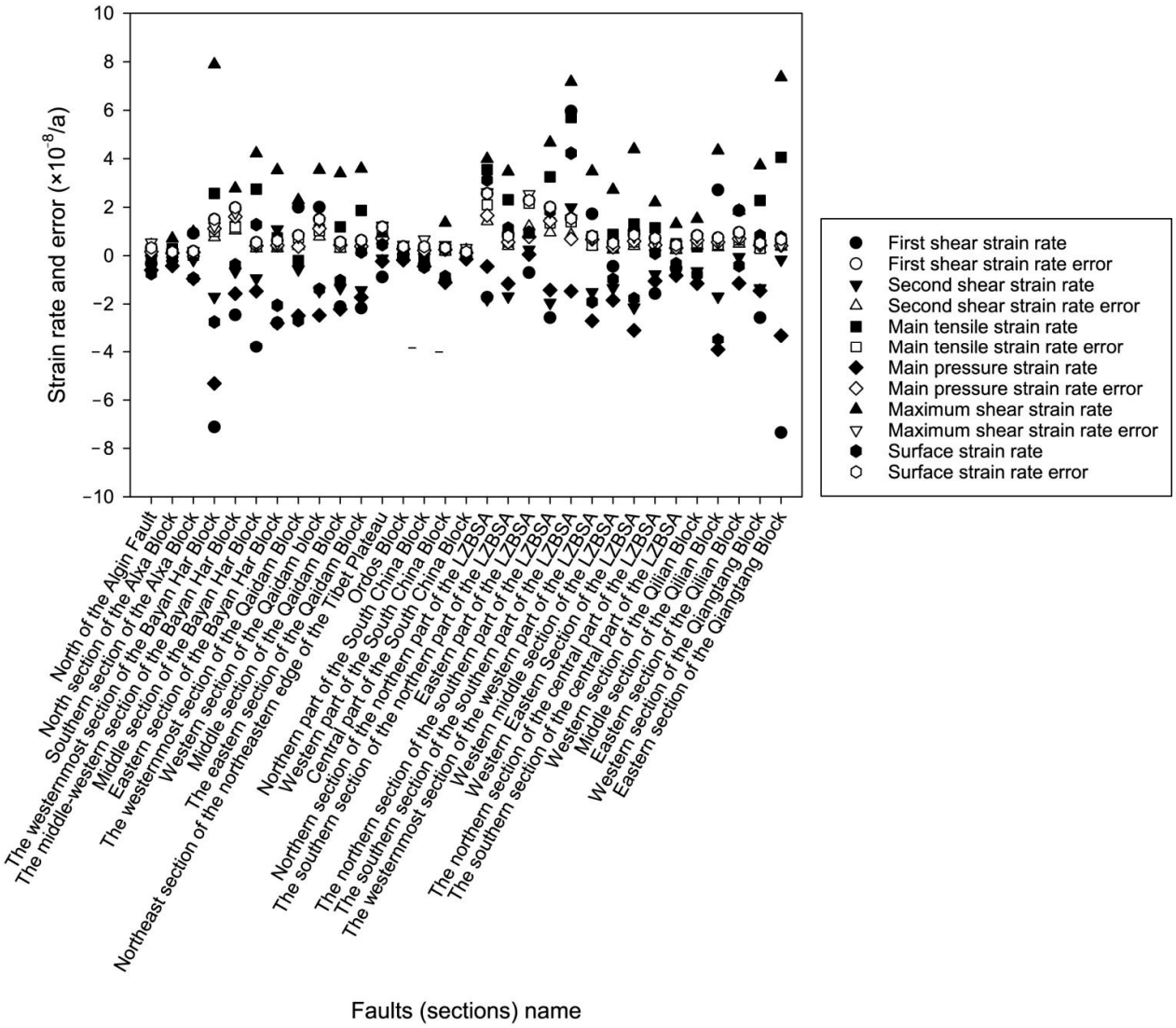


Figure 9. Strain statistics of secondary level blocks in the northern segment of the North–South Seismic Belt, China.

Based on an analysis of the temporal variation trends of strain parameters, the strain characteristics within the Longzhong Basin tectonic zone can be summarized as follows: In the northern subsection of the northern segment, east–west (EW)-oriented strain, north–south (NS)-oriented strain, principal strain, maximum shear strain and surface strain all present increasing trends; in the southern subsection of the northern segment, EW-oriented strain, NS-oriented strain, shear strain, principal strain and surface strain all display increasing trends; in the eastern segment, EW-oriented strain, NS-oriented strain, principal strain and surface strain present increasing trends; in the northern subsection of the southern segment, EW-oriented strain, NS-oriented strain, the first shear strain and principal compressive strain display increasing trends; in the southern subsection of the southern segment, NS-oriented strain and principal compressive strain present increasing

trends; in the western segment, EW-oriented strain, shear strain and principal strain display increasing trends; in the central–western subsection, linear strain, shear strain, principal strain and surface strain all present increasing trends; in the eastern–western subsection, shear strain displays an increasing trend; in the northern subsection of the central segment, linear strain, the second shear strain, principal strain and surface strain all present increasing trends; and in the southern subsection of the central segment, EW-oriented strain, NS-oriented strain, shear strain, principal strain and surface strain all display increasing trends.

Notable anomalous characteristics are identified as follows: the maximum shear strain, principal strain and surface strain in the northern subsection of the northern segment have increased significantly, and the absolute values of the second shear strain and northeast (NE)-oriented strain have reached the maximum value recorded since 1998; correspondingly, the maximum shear strain, the second shear strain, NE-oriented strain and principal strain in the northern subsection of the southern segment also reached the maximum value recorded since 1998.

For the central Qilian Block, the measured surface strain rate, maximum shear strain rate, principal compressive strain rate and first shear strain rate are -3×10^{-8}/a, 4×10^{-8}/a, -4×10^{-8}/a and 3.8×10^{-8}/a, respectively. Overall, the absolute values of the block's maximum shear strain rate, principal compressive strain rate, EW-oriented strain rate and first shear strain rate (which are 4×10^{-8}/a, -4×10^{-8}/a, -3×10^{-8}/a and 3.8×10^{-8}/a, respectively) all reach the maximum level recorded since 1998; the NE-oriented strain rate and the second shear strain rate of the block also remain at historically high levels. The spatial variation pattern of strain within the block can be summarized as follows: in the western part of the block, linear strain, shear strain, principal strain and surface strain all show an increasing trend; in the central part of the block, shear strain and principal strain exhibit an increasing trend; while in the eastern part of the block, EW-oriented and NE-oriented strains, shear strain, principal compressive strain and surface strain all present an increasing trend.

Within the western region of the Qaidam Block, the surface strain rate, maximum shear strain rate, principal compressive strain rate and first shear strain rate are measured as -2.7×10^{-8}/a, 2.3×10^{-8}/a, -2.5×10^{-8}/a and 2×10^{-8}/a, respectively. The absolute values of the overall strain rate across the entire block are all below 3×10^{-8}/a. Specifically, the strain level in the western region has remained at a normal high level since 1998, while the strain rate in the central and eastern regions has stayed within the normal range. The internal strain variation exhibits distinct zonal differentiation characteristics: the EW-directional strain, shear strain and principal strain in the western region all show an increasing trend; the NS-directional strain, principal strain and maximum shear strain in the central region show an increasing trend; and the linear strain, shear strain, principal strain and surface strain across the entire eastern region all present an increasing trend. Statistical observations indicate that, at the westernmost end of the block, the NS-directional strain (-2.3×10^{-8}/a), surface strain (-2.7×10^{-8}/a), maximum shear strain (2.3×10^{-8}/a), principal compressive strain (-2.5×10^{-8}/a) and first shear strain (2×10^{-8}/a) have all reached the highest level recorded since 1998, while the NE-directional strain and second shear strain also remain at a historically high level.

The strain rate within the Ordos Block and the region north of the Subei Kuantan Mountain segment of the Aljin Fault maintains a relatively low magnitude, and the strain rate of the Alxa Block stays at a normal level. For the Bayan Har Block, the strain rates in its western and central portions fall within the normal range, while the strain rate level in the eastern portion is slightly higher. Specifically, the absolute strain rate in the western portion is lower than 7×10^{-8}/a, that in the central portion is lower than 4×10^{-8}/a, and that in the eastern portion is lower than 3×10^{-8}/a. The strain variation within the Bayan Har

Block exhibits the following trends: the EW-oriented strain, NS-oriented strain, first shear strain, principal strain and surface strain in the western region all present an increasing trend; the EW-oriented strain, first shear strain, principal compressive strain and surface strain in the central region all show an increasing trend; and the NE-oriented strain, shear strain and principal strain in the eastern region all present an upward trend.

The absolute strain rate values in the western region of the Qiangtang Block are lower than 3×10^{-8}/a, indicating that the strain magnitude of this sub-region is relatively low; the absolute strain rate values in the eastern region of the block are lower than 8×10^{-8}/a. The spatial variation pattern of strain within the block presents the following characteristics: in the western sub-region, the linear strain, secondary shear strain, principal strain and surface strain all show an increasing trend, while in the eastern sub-region, the NS-oriented strain, triaxial strain and maximum shear strain exhibit more significant increments. The notable anomalous strain characteristics can be summarized as follows: the first shear strain, triaxial strain and surface strain in the western region have reached their maximum values since 1998; in contrast, in the eastern region, the EW-oriented strain (-3.7×10^{-8}/a), NS-oriented strain (4×10^{-8}/a), first shear strain (-7.2×10^{-8}/a), triaxial strain (4×10^{-8}/a), principal compressive strain (-3.2×10^{-8}/a) and maximum shear strain (7.2×10^{-8}/a) all reached their peak values recorded since 1998.

For the northern, western and central regions of the South China Block, the absolute strain rate values are lower than 1×10^{-8}/a, 4×10^{-8}/a, and 1×10^{-8}/a, respectively. On the whole, the strain rate levels in the northern region and the central–western region are relatively low. The strain variation characteristics within the South China Block are summarized as follows: in the northern region, NE-strain, NS-strain, the second shear strain, and the principal compressive strain all present an increasing trend; in the western region, EW-strain, first shear strain, principal compressive strain, and surface strain all demonstrate an increasing trend; and in the central region, EW-strain, NE-strain, and shear strain all exhibit an increasing trend.

In the northeastern region of the northern edge of the Tibet Plateau, specifically the northeastern section of the northern segment of the North–South Seismic Belt, the absolute value of the strain rate is less than 1×10^{-8}/a, indicating a normal activity level during this period; both the NS-oriented strain and the principal compressive strain in this area exhibit an increasing trend.

Based on the above strain rate analysis results, it can be concluded that since 1998, the absolute value of strain rates in the area north of the eastern segment of the Aljin Fault has consistently been below 2×10^{-8}/a, indicating moderate-to-weak strain activity during this study period; the overall absolute strain value of the Alxa Block is lower than 1×10^{-8}/a, which indicates that the strain activity of the block has remained at a normal level since 1998. Cumulative growth trends are observed in the shear strain in the northern part of the block, as well as the shear strain and the principal compressive strain in the southern part. The absolute strain rate of the Ordos Block remains below 0.5×10^{-8}/a, which indicates that the strain activity within this block has remained at a relatively low level since 1998. Meanwhile, the linear strain, secondary shear strain, principal compressive strain and areal strain all present cumulative increasing trends across the entire block. The results obtained in this study are generally consistent with the conclusions reported in existing published research [13,16,39,46,49,50].

6. Fracture Sliding Rates and Sliding Deficit Ratio

In linear inversion problems, taking fault slip magnitude estimation as a representative case, geophysical inversion theory constructs a quantitative mathematical framework for resolving model parameters including fault slip angles and sliding velocities from observational data. By establishing the functional relationship between surface displacement

observations induced by rectangular fault slip in an elastic half-space and the corresponding Green's function, fault motion parameters can be estimated via inversion. In general, the Green's function in this context is derived on the basis of elastic dislocation theory [51–53]. Through rotation and translation transformations of the GNSS displacement field, projection of the displacement field onto the fault plane can be achieved, which enables the construction of the functional relationship between the observed displacement field and unknown fault parameters. The DEFNODE software of ver.2007 developed by McCaffrey adopts the McCaffrey block model [54–56]. This model assumes that active faults maintain complete locking during the inter-seismic period, and the resultant velocity field V is decomposed into the sum of three components: the rigid rotation rate of the fault block, the fault slip deficit rate, and the uniform elastic strain rate within the block, as formulated in Equation (1). Given the rigid rotation rate of the blocks on either side of an active fault $V_B(\Omega)$, The velocity difference between the blocks can be decomposed and projected into the strike-slip, dip-slip, and extensional rate components of the fracture: S_S, S_D and S_T. $V_B(\Omega)$ is shown in the Equation (2). The rate of sliding deficit caused by fracture at the block boundary $V_C(\Omega)$ is represented by Equation (3). Among these, the Green function G_0 corresponds to the rectangular dislocation element, selected in the DEFNODE program. The uniform elastic strain rate within the block $V_{\dot{\varepsilon}}(\dot{\varepsilon})$ is shown in Equation (4), McCaffrey proposed Equation (5) based on GNSS horizontal velocity data to estimate slip rate, locking rate, and Eulerian pole. Among these, the sliding rate, the locking rate ϕ_{nk}, and Ω are parameters to be inverted, and the sliding deficit rate $\Omega_f^{\mathrm{h}} \cdot \phi_{nk}$ is defined by the aforementioned formula. For the specific definitions of each symbol, refer to McCaffrey's literature [54].

$$V = (\Omega) - V_C(\Omega) + V_{\dot{\varepsilon}}(\dot{\varepsilon}) \tag{1}$$

$$V_B(\Omega) = \begin{bmatrix} -sin\varphi cos\theta & -sin\varphi sin\theta & cos\varphi \\ -sin\theta & cos\theta & 0 \\ -cos\varphi cos\theta & -cos\varphi sin\theta & -sin\varphi \end{bmatrix} \begin{bmatrix} 0 & \hat{z} & -\hat{y} \\ -\hat{z} & 0 & \hat{x} \\ \hat{y} & -\hat{x} & 0 \end{bmatrix} \begin{bmatrix} \Omega_{\hat{x}} \\ \Omega_{\hat{y}} \\ \Omega_{\hat{z}} \end{bmatrix} \tag{2}$$

$$V_C(\Omega) = [S_S \quad S_D \quad S_T]^T \tag{3}$$

$$V_{\dot{\varepsilon}}(\dot{\varepsilon}) = \begin{bmatrix} Rsin\theta_0 \triangle\phi & R\triangle\theta & 0 \\ 0 & Rsin\theta_0 \triangle\phi & R\triangle\theta \end{bmatrix} [\dot{\varepsilon}_{\phi\phi} \quad \dot{\varepsilon}_{\phi\theta} \quad \dot{\varepsilon}_{\theta\theta}]^T \tag{4}$$

$$V_i(X) = \sum_{b=1}^{B} H \cdot (\Omega_b^R \times X) \cdot \hat{i} - \sum_{k=1}^{F} \sum_{n=1}^{Nk} \sum_{j=1}^{2} \phi_{nk} \cdot G_{ij}(X, X_{nk})(\Omega_f^{\mathrm{h}} \times X_{nk}) \cdot \hat{j} \tag{5}$$

Based on the published research by Academician Deng Qidong on the geometric boundaries of active fault zones and the spatial distribution of major active faults across China [17], this study first determines the spatial positions of fault nodes, and subsequently conducts inversion to estimate the slip rate and slip deficit rate of major active faults. In this study, fault nodes with equal quantity are constructed at depths of 0.5 km, 14 km, and 30 km, respectively. For the recalculation of Green's functions, the distance between any newly added node and all pre-existing nodes is constrained to be greater than 1 km, and observation stations that are more than 4000 km away from all nodes are excluded from the calculation of Green's functions. This study implements a joint algorithm combining simulated annealing and grid search and sets the initial temperature to 0 °C and the gradient search step size to 0.001 mm/a, under the prior assumption that fault locking rate decreases as depth increases. After the inversion process is completed, a forward model is constructed to calculate the corresponding residual of strain and rotation. Subsequently, we utilized the non-integrated number χ^2 to continuously verify the uni-

formity of the strain rate fields within each block obtained through inversion and by adjusting the weight standard deviation factor f to make χ^2 approaching 1. *dof* represents the number of degrees of freedom, calculated as the number of observations minus the number of free parameters. r_i represents the residual vector, and σ_i represents the data uncertainty matrix (see Equation (6)). Table 2 presents the inversion results of slip deficit, locking rates, and total slip/strike-slip/dip-slip velocity components at 0–40 km depth along the selected active fault segments in the northern segment of the North–South Seismic Belt of China, covering the study period from 1998 to 2024.

$$\chi_n^2 = \frac{\sum_{i=1}^{n} \left(\frac{r_i}{f\sigma_i} \right)^2}{dof} \quad (6)$$

Table 2. Statistical summary of slip deficit, locking rates, and total slip/strike-slip/dip-slip velocity components at 0–40 km depth along the selected active fault segments in the northern segment of the North–South Seismic Belt during 1998–2024 (positive values represent northward (N) and eastward (E) velocity components, respectively).

Fracture Segment	Sliding Loss (mm/a)	Locking Rate	Total Slip Rate (mm/a)	Strike-Slip Rate (mm/a)	Dip-Slip Rate (mm/a)
The "Andir River–Cherchen River" section of the ATF	0.01~7.02	0.02~1.00	0.26~6.85	0.17~4.92	−6.76~−0.20
The "Solkuri–Aksay" section of the ATF	1.56~7.21	0.22~1.00	6.99~7.03	0.20~3.31	−6.99~−6.19
The "Subei Kuantan Mountain" section of the ATF	1.04~4.82	0.22~1.00	4.64~4.70	−3.83~1.84	−4.70~−2.73
The "Tianshui" section of the fault along the WQNF	0~2.36	0~1.00	0~2.36	−0.19~0.70	−2.36~0
The "Luanfeng" section of the fault along the WQNF	0~3.22	0~1.00	0~3.22	−1.11~0	−3.19~0
The "Tanxian" section of the fault along the WQNF	0~2.19	0~1.00	0~2.20	−0.01~0.05	−2.20~0
The "Guomatan" section of the fault along the WQNF	0~1.95	0~1.00	0~1.94	−0.55~0.50	−1.92~0
The "Qukusai Lake" section of the EKF	0.00~10.36	0.01~1.00	0.16~9.89	−2.56~3.24	−9.89~−0.16
The "Dongxidatan" section of the EKF	2.23~9.53	0.25~1.00	9.07–9.12	−0.30~2.41	−9.09~−8.78
The "Xiugou–Alak Lake" section of the EKF	1.98~8.53	0.24~1.00	8.09~8.12	−8.08~6.01	−8.10~8.09
The "Alak Lake–Tosuo Lake" section of the EKF	0.00~14.43	0.01~1.00	0.22~13.78	−10.03~5.24	−13.78~−0.15
The "Tosuo Lake–Maqu" section of the EKF	0~10.06	0~1.00	0~9.64	−7.74~0.21	−9.57~0
The "Shao Kou–Kui Xiang" section of the HYF	0.04~3.73	0.08~1.00	0.47~3.74	−1.18~−0.10	−3.70~−0.46
The "South/West Huashan" section of the HYF	0.20~5.03	0.16~0.99	1.30~5.08	−3.37~−0.64	−4.85~−1.13
The "Hasishan–Machangshan" section of the HYF	0~4.69	0.00~1.00	0.03~4.71	−2.87~−0.02	−4.68~−0.03
The LPF	1.39~6.34	0.23~1.00	6.18~6.20	−5.86~0.83	−6.20~−1.98
The "Zaoxia–Dahuanggou" section of the fault along the NQF	0.38~1.83	0.21~1.00	1.81~1.82	0.22~1.44	−1.80~−1.10
The "Yumen" section of the fault along the NQF	0.30~1.48	0.21~1.00	1.46~1.47	−0.85~1.46	−1.46~1.46
The "Fodongmiao–Hongyazi" section of the NQF	0.29~1.42	0.21~1.00	1.40~1.41	−1.40~0.89	−1.15~1.40
The "Sunan" section of the NQF	0.42~2.06	0.21~1.00	2.04~2.04	−2.04~2.04	−2.04~2.04

Numerous prior studies have carried out slip deficit estimation and high-seismic-hazard zone identification for the study area. On the whole, existing research has reached a consensus on the overall pattern of seismic hazard: the main strike-slip fault zone crossing the study area presents the highest long-term average slip deficit rate and is the region with the highest potential for generating strong earthquakes above magnitude 7.0. This conclusion is highly consistent with the regional historical distribution records of strong earthquakes. However, significant discrepancies exist in the quantitative estimation results of key parameters among different studies:

For the slip deficit rate of the central and western segments of the study area, early investigations based on sparse GNSS observation networks yielded estimation results of 4–6 mm/a, while recent studies with denser observation coverage obtained results of 2–

3.5 mm/a, with a difference of nearly twofold between the two sets of results. Regarding the delineation extent of high seismic hazard zones, although all existing results cover the eastern segment of the study area where historical strong earthquakes with M ≥ 8.0 occurred, the area of the delineated high-hazard zones in the central segment differs by nearly twofold across different studies.

These discrepancies in research results are essentially caused by inconsistent variable independence assumptions and inconsistent data processing procedures adopted by different studies, which directly demonstrates the necessity of this study to re-estimate regional slip deficit and seismic hazard through an improved uncertainty quantification framework that fully considers the interdependence among multiple influencing factors.

7. Discussion

7.1. The Mechanisms of Earthquake Generation and Occurrence Within a Structural Context

The geological structures across different regions of the Tibet Plateau have undergone distinct magmatic activities and crustal modification processes. The stress accumulation, rupture, and release mechanisms near fault zones exhibit coupling relationships with the physicochemical properties of various media components as well as the mechanical behaviors of fluids and solids. Observations reveal vertical continuity in crustal and mantle deformation within the plateau, indicating strong coupling between these systems, where shear mechanical properties directly correlate with the degree of coupling. In general, high friction coefficients, rapid stress loading rates, low strain rates, and high shear moduli correspond to geological conditions featuring sliding resistance, high slip dissipation rates, substantial stress accumulation, and locked fault states. Via finite element dynamic simulation, Shi Fuqiang et al. identified potential hazardous segments of active faults characterized by high stress rates and strong locking properties, which include the eastern segment of the Aljin Fault, the central–western segment of the Haiyuan Fault, the Liupanshan Fault, and the central–western segment of the northern margin faults of the Western Qinling Mountains [57]. Variations in temperature and pressure conditions may trigger dehydration reactions of mica and amphibole, leading to an increase in pore fluid pressure within the crustal medium. This process is recognized as a key contributing factor for the formation of high-conductivity layers in the continental crust. Dehydration increases the fluid content in the middle-to-lower crust, which may further induce localized partial melting. When these high-conductivity layers experience shortening or shear deformation, stress can propagate upward into the high-resistivity and sub-high-resistivity layers of the upper crust, eventually triggering shear fracture failure at the pre-locked, structurally weak sites [8]. Prior to the occurrence of large earthquakes, rock dilatancy in the focal region causes a rapid drop in pore pressure, which facilitates the gradual formation of connected pore networks and enables the infiltration of peripheral fluids into the focal area. In deep fault zones, mantle-derived high-temperature and high-pressure materials can even intrude upward, leading to the formation of low-velocity seismic anomalies.

Medium-scale heterogeneity constitutes another direct triggering factor for earthquake occurrence. Localized temperature increases induce uneven uplift of the upper mantle, which imposes substantial shear stress on overlying fault zones and further generates localized tensile stress. This geological phenomenon has been identified in the Yitong–Shulan Fault Zone, coastal islands of Fujian, and newly active faults in central–western Fujian. Compared with fault opening and activation driven by thermal material upwelling, the cascading triggering effect between adjacent lateral fault systems is more likely to be the key mechanism of earthquake initiation, and this topic remains a core controversy in the research of seismogenic environment and mechanism. Episodic fault dislocation and post-seismic viscoelastic relaxation are two dominant processes governing

Coulomb stress variation, both of which regulate earthquake triggering among adjacent lateral fault systems. In general, the influence of episodic fault dislocation is more significant than that of viscoelastic relaxation. The magnitude of this effect is significantly correlated with earthquake magnitude, inter-event time interval and spatial distance between faults. This correlation has been confirmed by the M5.7, M5.9, and M5.6 earthquake sequence that occurred along the Tuanbao Fault and Dawangcun Fault in the Datong–Yanggao area of Shanxi Province on 19 October 1989 [58].

It should be noted that an increase in Coulomb stress only indicates that the fault has approached its rupture threshold and does not necessarily mean that an earthquake is imminent. Earthquake triggering is jointly controlled by multiple factors including stress accumulation rate and the yield strength of the fault zone. Viscoelastic–plastic finite element numerical simulation results [59] show that the stress distribution along the fault zones on the northeastern margin of the plateau is heterogeneous, and Coulomb stress can transfer between different fault zones. When the accumulated loading stress reaches the yield threshold of specific seismogenic faults, earthquake clustering may be triggered. At present, the viscoelastic stress relaxation effect in this region has attenuated significantly, which suggests that the Haiyuan Fault Zone has a high probability of hosting the next large earthquake.

7.2. Fracture Sliding and Locking Characteristics of the Northern Segment of the North–South Seismic Belt in China

Long-term tectonic loading from adjacent tectonic units triggered the 1932 Changma earthquake that occurred along the Aljin North Margin Fault Zone. Although the magnitude of Coulomb stress accumulated by inter-seismic tectonic loading is lower than that of co-seismic stress, this loading process remains the dominant contributor to the cumulative stress buildup within the fault zone over a long geological timescale. This study demonstrates that the Solkuri–Aksai segment exhibits elevated strike-slip and dip-slip rates; the Su Bei Kuantan Mountain segment shows attenuated slip deficit, with its strike-slip and dip-slip rates both decreasing significantly; the average locking depth of the entire fault is approximately 15 km, and the slip deficit rate of the Su Bei Kuantan Mountain segment is 4.82 mm/a.

The Haiyuan Fault constitutes a weak zone developed during the Paleozoic and is categorized as a large-scale deep fault at the crustal scale. The lithosphere underlying the fault is relatively thin, the lithospheric mantle cover exhibits high seismic velocity, and the lower crust contains a highly conductive weak layer; both the upper crust and lower crust show concurrent joint thickening [7]. This study indicates that: under the narrow definition, the Haiyuan Fault is characterized by uniformly distributed locking rate, shallow locking depth and low coupling intensity; the eastern segment of the Hasi Mountain–Machang Mountain section is characterized by low strike-slip velocity and high dip-slip velocity; the Liupanshan Fault shows uniform and increasing slip deficit distribution, with locked zones extending 15–20 km deep and uniformly distributed across its Haiyuan segment and the Guyuan–Jingyuan boundary; and the dip-slip velocity decreases along these sections.

As the leading edge of the northeastward extension of the Tibet Plateau, the Qilian Mountain orogenic belt represents the tectonic deformation process along the plateau's northeastern margin during the Cenozoic era. The northern margin fault zone of Qilian Mountain, extending to depths of 20 km, forms a slip structure with an inclination of approximately 15° and exhibits close connections with the Haiyuan Fault. Historical records indicate five destructive earthquakes of magnitude ≥7 in the Qilian Mountain–Hexi Corridor region; the Lenglongling Fault, located at the eastern end of the study region, is the most prominent boundary fault along the northeastern margin of the Tibetan Plateau,

where the M 6.4 Menyuan earthquake (occurred in Menyuan, Qinghai, on 21 January 2016) was hosted. Existing research [7] proposed that the crust–mantle system of the Qilian Orogenic Belt exhibits multiple deformation mechanisms: the middle-lower crust lacks prominent low-velocity layers, while the upper crust develops distinct low-velocity anomalies. This study reveals that the slip rates of the Yumen segment, which encompasses Gaotai County and the western region of Sunan Yugur Autonomous County, and the Sunan segment maintain relatively stable states. Within the study segments, the Zaoxia–Dahuanggou segment, the Yumen segment, and the Sunan segment all show enhanced slip deficit, while the slip deficit of the Fodongmiao–Hongyazi segment is attenuated. Fault locking characteristics exhibit homogeneous spatial distribution across the study area in the depth range of 15–20 km.

The East Kunlun Fault Zone has historically hosted multiple strong seismic events, including the 1937 Mw 7.5 Huashixia earthquake, the 1963 Mw 7.1 Dulan earthquake, and the 1973 Mw 7.3 Ma DOI earthquake. On 22 May 2021, the Mw 7.4 Maduo earthquake occurred along the Maduo–Gande Fault, which lies approximately 70 km south of the East Kunlun Fault Zone. This study demonstrates that the East Kunlun Fault Zone presents a remarkable overall slip deficit, and a significant increasing trend of slip deficit has been detected in the Alag Hu–Tuzuo Hu segment in recent years. Except for the Tuzuo Hu and Maqu segments, the locking degree is uniformly distributed across all other segments, with the locked zone extending to a depth of 15–20 km. The strike-slip rate decreases along the Kusai Hu segment; in contrast, the strike-slip rate increases while the dip-slip rate decreases in the Dongxiatan segment, and the dip-slip rate increases in the Alag Hu–Tuzuo Hu segment. The overall slip rate of the Xiugou–Alag Hu and Tuzuo Hu–Maqu segments exhibits negligible variation, and these two segments maintain a high degree of fault locking. On the whole, slip deficit has decreased in all segments except the Alag Hu–Tuzuo Hu segment.

The Western Qinling, where the northern marginal fault of the Western Qinling Mountains is located, is characterized by continuous tectonic deformation. Numerous faults with relatively low slip rates across this region accommodate distributed strain accumulation, and the rotational motion of the regional and adjacent blocks has accommodated a portion of the regional strain. The 2013 M 6.6 Minxian–Zhangxian earthquake in Gansu Province occurred on the Lintan–Dangchang Fault in the central segment of this orogenic belt. Observational data indicate that from 2013 to 2015, approximately 47% of the fault zone had a slip rate close to 0 mm/a; from 2015 to 2020, the dip slip rate of the Tianshui segment decreased to 2.36 mm/a, while the slip rate of the other segments increased, and the overall slip rate presents a gradual decreasing trend from west to east [28]. This study reveals that the slip deficit of the Tianshui segment is concentrated in the eastern portion of the segment; the slip deficit of the Tanxian segment is mainly distributed in a small area in the eastern part of the segment; the slip deficit of the Guomatan segment is concentrated at the easternmost end of the segment; the slip deficit of the Luanfeng segment is widely developed in the western part of the segment, and the deficit intensity gradually increases from east to west. In addition, the strike-slip rate at the eastern end of the Guomatan segment decreases; the coupling between the Tanxian segment and the Guomatan segment is weak; and the Luanfeng segment has accumulated a large amount of slip deficit.

7.3. Comparative Verification of Tectonic Deformations Observed by GNSS

Multiple lines of observational evidence indicate that localized and continuous strain accumulation occurs across multiple tectonic belts, driving significant crustal deformation that can be classified as follows: thrust nappe movement is developed in the middle segment of the Aljin Fault Zone, the boundary between the Qilian Block and Qaidam Block,

the junction of the Bayan Har Block and Qiangtang Block, and the central southern boundary of the Qilian Block; left-lateral strike-slip movement is developed along the western segment of the northern boundary of the Qilian Block and the Zhuanglanghe Fault; and left-lateral reversed strike-slip movement occurs in the eastern segment of the North Qinling Northern Edge Fault Zone and the eastern part of the northern boundary of the Qilian Block. The results presented above are consistent with the conclusions of previous studies [13,15,43,60–63].

The characteristics of the velocity field in the northern segment of the North–South Seismic Belt indicate that the tectonic compressive stress derived from the Indian Plate shows a gradual attenuation pattern along the south-to-north and west-to-east directions. Based on multi-epoch velocity projection data acquired from GNSS stations deployed along major active fault zones by the *National Crustal Movement Observation Network of China* during 1998–2024, combined with the calculated fault slip rates, the following conclusions are obtained: The northern boundary of the Qilian Block has prominent tectonic activity; the strike-slip component shows an increasing trend in the eastern segment, while the western segment is dominated by a convergence state. As a whole, this boundary consistently presents the kinematic feature of thrust strike-slip motion. The strike-slip velocity along the Aljin Fault Zone exhibits a general deceleration trend, which is particularly pronounced in the eastern segment of the fault zone. The Zhuanglanghe Fault still maintains thrust strike-slip motion, and its strike-slip component shows a weakening trend. The Haiyuan Fault remains dominated by left-lateral thrusting motion, and the intensity of its strike-slip activity has decreased. The Yinchuan Basin is still located in a long-term extensional tectonic setting. The fault zone along the northern margin of the Western Qinling Mountains presents spatially heterogeneous kinematic patterns: the western and central segments show extensional characteristics, while the strike-slip and vertical motion in the eastern segment is extremely weak or nearly quiescent. The thrust strike-slip motion along the Liupanshan Fault continues to weaken and is close to quiescence. The above results are in good agreement with some previous research findings [1,16,25,50,64,65].

Analysis of the regional strain rate field demonstrates that the strain rate field within the fault zone along the northern margin of the Western Qinling Mountains shows no significant directional variation, and the strain magnitude in this region exhibits a decreasing trend. The overall shear strain rate presents a decreasing trend of approximately 0.1×10^{-8}/a in the areas adjacent to the eastern part of the Qilian Block, the eastern part of the Qaidam Block, the central segment of the Longzhong Basin structural zone, the Haiyuan Fault, the Zhuanglanghe Fault, and the middle-western segment of the northern Qinling Fault Zone. The principal compressive strain rate shows a decreasing gradient across the Qiangtang Block, the central–southern region of the Bayan Har Block, the southern segment of the Longzhong Basin structural zone, and the northern Qilian Block, with the magnitude of the decrease ranging from 0.1×10^{-8}/a to 0.2×10^{-8}/a. In contrast, the magnitude of the principal compressive strain rate displays an increasing trend along the Zhuanglanghe Fault and in the eastern Qaidam Block, with an increment of approximately 0.1×10^{-8}/a. No anomalous variations were identified in the observed surface strain field. The observed results regarding the variations in the strain rate field are in good agreement with the findings reported in previous studies [46,49,66,67] in terms of both direction and magnitude.

7.4. The Seismic Risk in the Study Area

The study area is located at the northeastern margin of the Tibet Plateau, situated at the junction between the Ordos Block and the Alxa Block, where tectonic activity is intense [68]. Material escape from the plateau in the NE direction has triggered significant fault slip and orogenic movements, contributing to the region's seismic activity [4]. The fault zones in the area predominantly run along NWW, NW, and NNW orientations, with their overall arc-shaped structures converging toward the southeast and diverging toward the northwest. Among these, the Haiyuan Fault Zone is the largest and most active left-lateral strike-slip fault in the arc-shaped active fault system along the northeastern margin of the plateau and is the main active fault controlling the occurrence of moderate–strong earthquakes in the region [10,69]. With the exception of the northern segments of the Niushoushan Fault and the Yunwushan Fault, all other faults within the study region have exhibited activity since the Late Pleistocene–Holocene epoch [70]. The stress field surrounding the Ordos Block is dominated by tensional stress, and fault activity is characterized by the predominance of strike-slip and normal faults, which collectively account for approximately 75% of the total fault activity within the study area. Along the western margin of the Ordos Block, the dominant compressive stress is oriented in the NE–NEE direction [71]. Liang K [72] proposed that the overall regional deformation fits an S-shaped extensional structural pattern developed along the Yinchuan–Wuhai–Jilantai–Hetao Basin, with the magnitude of deformation in this region being relatively limited.

Current academic research has reached a consensus that the slip rate of active faults serves as a core indicator for characterizing their long-term background slip behavior. Under large deformation conditions, regions with localized deformation enhancement correspond to deformation locking zones where in situ stress accumulates, and such regions are identified as key monitoring targets due to the dynamic evolution of crustal movement fields [73].

Although the study area only accounts for approximately 6% of the total land area of the Chinese mainland, it is characterized by frequent occurrences of strong historical earthquakes: a system of normal faults develops along the periphery of the Ordos Block, with earthquakes exceeding magnitude 8.0 occurring there accounting for about one-quarter of China's total historical strong earthquake occurrences; roughly one-third of China's magnitude 8.0 or higher earthquakes occurred at the junction between the Ordos Block and the northeastern edge of the Tibet Plateau; and since historical records began, a total of 19 strong earthquakes exceeding magnitude 7.0 have been recorded around the Ordos Block, all concentrated along peripheral active faults and in faulted basins [68,70,74].

Multiple large-magnitude historical earthquakes have been documented in this region, including the 1561 M 7.5 earthquake south of Mingsha, Zhongning, the 1622 M 7 earthquake north of Guyuan, the 1709 M 7.5 earthquake south of Zhongwei, the 1654 M 8.0 earthquake in Tianshui, the 1739 M 8 earthquake in Yinchuan–Pingluo, the 1879 M 8.0 earthquake in Wudu, the 1920 M 8.5 earthquake in Haiyuan, and the 1927 M 8.0 earthquake in Gulang. The northern segment of the North–South Seismic Belt has hosted six historical earthquakes with magnitude no less than M 8.0, among which four events with definite seismological records are the 1654 Tianshui earthquake, the 1739 Pingluo earthquake, the 1920 Haiyuan earthquake, and the 1927 Gulang earthquake. All faults that ruptured in these major earthquakes still maintain significant present-day seismic activity. Long-term seismological observations and statistical analysis show that the average recurrence interval of earthquakes with magnitude M 8.0 or larger along the western margin of the Ordos Block is 89 ± 50 years, and pre-seismic quiescent strong earthquakes in this seismic belt are mainly concentrated in its northern segment [42]. Although the western

margin of the Ordos Block is no longer classified within the Haiyuan seismic zone, it is currently in the inter-seismic period.

Existing studies have conducted systematic investigations on the seismic hazard of this region. Based on co-seismic effect analysis, post-seismic Coulomb stress accumulation research, seismic gap modeling and strong earthquake recurrence probability models, Zhang R et al. [75] concluded that the boundary zone along the western margin of the active Ordos Block adjacent to north–south striking faults has relatively high seismic hazard, and the southern segment of the Yellow River Fault and the Sanguguan Fault have elevated probabilities of strong earthquake recurrence in the next two decades. This study employed a normal distribution probability model to estimate the recurrence probability of strong earthquakes within the next 20 years, with the research scope covering areas with recorded historical strong earthquake events, including the eastern foothill of Luoshan Mountain, Laohushan Mountain, the central–western segment of the Haiyuan Fault, and the northern segment of the Liupanshan Fault. Liang Kuan [72] suggested that the elapsed time since the most recent rupture event on the concealed faults along the Yellow River has exceeded the average recurrence interval of characteristic earthquakes, indicating that these fault zones currently carry high seismic hazard. Fan Y and Che Z [76] delineated seven potential rupture zones with high susceptibility to M ≥ 7 earthquakes within the northern segment of the North–South Seismic Belt, specifically including the Maomaoshan area, the Jinqianghe area, the eastern segment of the Xiangshan–Tianjingshan Fault, the Lingwu segment of the Yellow River Fault, the northern margin of the Western Qinling Mountains, the Maqin–Maqu segment of the Eastern Kunlun Fault, and the eastern segment of the Liupanshan–Baoji Fault. Based on analysis of ML ≥ 5.0 seismic activity patterns, the North–South Seismic Belt is likely to enter a new phase of intense seismic activity following the 2008 Wenchuan M8.0 earthquake. Zhang N et al. [29,31] noted that from the 2008 Wenchuan earthquake of magnitude 8.0 to the end of 2018, crustal activity along the northeastern margin of the Tibet Plateau remained relatively low, exhibiting a period of seismic inactivity with magnitudes ≤7.0. However, multiple pieces of evidence indicate that the region has entered a new phase of strong seismic activity [77]:

(1) Analysis of the characteristics of seismic activity for earthquakes with magnitude ≥5.0 reveals distinct precursor signals corresponding to the aforementioned new active seismic phase.
(2) Statistical analysis of seismic cycles indicates that, subsequent to the 1927 Ms 8.0 Gulang earthquake, the northern segment of the North–South Seismic Belt faces a potential seismic hazard of earthquakes with magnitude ≥8.0 occurring between 2018 and the subsequent 50-year period.
(3) Seismological data indicate that over 30 years have passed since the 1990 Gonghe earthquake of magnitude 7.0, and the current period of relative calmness aligns closely with the longest interval of seismic inactivity observed in the region since 1900, suggesting a high probability of a magnitude ≥7.0 earthquake within the next two years.
(4) The 22 July 2013 Minxian–Zhangxian earthquake of magnitude 6.6 marked the first event in the fourth active period along the northeastern margin of the Tibet Plateau since 1900, suggesting the region may be entering a prolonged active phase lasting approximately 17 years, characterized by at least seven magnitude ≥6.0 earthquakes and one magnitude ≥7.0 earthquake.

Regarding fault locking states and deformation analysis, Du F et al. [78] utilized precise small-seismic positioning data, focal mechanism solutions, integrated active tectonic information, GNSS deformation data, historical seismic records, and modern seismic activity data to predict potential strong earthquakes in the middle-southern segment of the Liupanshan Fault. Wei C [79] adopted constrained inversion based on GNSS velocity field

data to quantify the fault locking degree and slip deficit rate, and the results indicated that the western section of the Haiyuan Fault, the central–western segment of the Xiqinling Fault, the northwestern segment of the Liupanshan Fault, and the southern segment of the Longriban Fault are all characterized by high-strength fault locking. Zhang N et al. [28] applied a dislocation theoretical model to invert the kinematic parameters of major active faults in northern Ningxia and its adjacent regions. The inversion results confirmed the presence of fault locking phenomena in the following areas: the southern end of the northern segment (central Wuzhong City) and the southern end of the southern segment (central Tongxin County) of the Niushoushan–Luoshan Fault; the western and eastern ends of the western segment of the Xiangshan–Tianjingshan Fault Zone (eastern Zhongwei City); and the western end of the Guanguangling Fault (within Jingtai County). In addition, a localized locked zone at depths shallower than 15 km was identified along the southern segment of the Helan Mountain East Slope Fault, in the administrative jurisdiction of Yinchuan City.

To investigate the dynamic variation characteristics of slip rates of major active faults in the northern segment of the North–South Seismic Belt, this study performs a comprehensive analysis based on multi-temporal slip rate estimation results of key active faults obtained from GNSS velocity fields covering 1998–2024, integrating seismological indicators and the latest evolution characteristics of GNSS strain rate fields.

(1) Under the background of continuous tectonic activity in the study area, potential locked fault zones are inferred along the eastern segment of the Aljin Fault Zone, the central–western segment of the Eastern Kunlun Fault Zone, the northern boundary of the Qilian Block, the northern segment of the Zhuanglanghe Fault, the southern segment of the Haiyuan Fault, the northern segment of the Liupanshan Fault, and the eastern segment of the Western Qinling North Edge Fault Zone. These areas are classified as high seismic hazard zones with potential for $M \geq 6.0$ strong earthquakes within the next decade.

(2) Based on the analysis of velocity projection, strain rate and fault slip deficit, the surface movement rate on both sides of the Aljin Fault, the area north of the Haiyuan Fault, the southwestern margin of the Alxa Block and the Ordos Block, the northern margin of the Qilian Block, the Yinchuan Basin, and the junction zone between the Alxa Block and the Ordos Block is dominated by stable or increasing trends, while the surface movement rate in the southern margin of the Ordos Block shows a decreasing trend.

(3) Significant crustal shortening and shear deformation are observed along the eastern segment of the northern margin fault of the Qilian Mountains. Regarding the strain variation characteristics, the minimum shear strain presents a decreasing trend in the Qilian Block, the eastern Qaidam Block, and the central segment of the Longzhong Basin structural belt, while shear strain shows an increasing trend along the Haiyuan–Liupanshan Fault and the northern margin fault of the Western Qinling Mountains. Since 1998, peak strain values have been recorded in the northern Longzhong Basin structural belt, the central Qilian Block, the western Qaidam Block, and the eastern Qiangtang Block. In terms of stress–strain accumulation characteristics, significant compressive stress accumulation is detected at the northern and southern boundaries of the Qilian Block, the western segment of the southern boundary of the Qaidam Block, and the Kekexili region; high shear strain rates are observed at the junction of the northern margin fault of the Qilian Mountains and the Alxa Block, the southern Qaidam Block, the central–eastern Bayan Har Block, and the eastern Qiangtang Block.

(4) A certain increasing trend of stress accumulation is identified in the following tectonic units: the thrust movement zone of the Subei Kuantan Mountain segment of the

Aljin Fault, the Haiyuan Fault, and the Tianshui segment of the northern margin fault of the Western Qinling Mountains; the left-lateral strike-slip thrust movement zone of the Haiyuan Fault and the Liupanshan Fault; the left-lateral strike-slip thrust movement zone of the northern margin fault of the Western Qinling Mountains; the left-lateral thrust movement zone along the northern boundary of the Qilian Block; and the thrust movement zones at the junction of the Qilian Block and the Qaidam Block, the junction of the Bayan Har Block and the Qiangtang Block, and the central southern boundary of the Qilian Block.

7.5. Constraints in Comprehensive Research on Multi-Source Information

This study carries out an integrated investigation using multi-source data, covering tectonic stress regimes, rock rheological properties, mechanical characteristics, seismic wave anisotropy, geo-electromagnetic fields and gravity fields in the northeastern margin of the plateau. A systematic analysis is conducted to evaluate the influences of such factors as upwelling mantle materials and crustal low-resistance weak zones on crustal movement trends and interplate fault coupling. This research synthesizes previous research results concerning fluid intrusion in Coulomb stress concentration zones, fault friction coefficients, regional viscoelastic–plastic behavior and cascade effects along fault zones, and incorporates observational data of surface strain, fault slip rates and slip deficits to improve the analytical rigor. To address the poor readability of the original multiple sets of comparative datasets, this study added a descriptive statistical figure (Figure 9) for all quantitative strain and stress data to visualize the overall trends and individual variations of data across different tectonic units. This optimization preserves all original raw data in the summary tables, while presenting the spatial differentiation pattern and statistical correlation of deformation characteristics more intuitively. Nevertheless, this study still has several limitations. First, geophysical exploration methods can only provide partial measurements of physical parameters, and uncertainties still exist in both data acquisition and interpretation. For example, seismic tomography is restricted by station distribution, data receiving conditions, solution non-uniqueness, insufficient spatial resolution and initial model assumptions, which makes it difficult to reach reliable quantitative conclusions. Second, the influencing factors are non-independent and mutually correlated; in addition, variations in theoretical frameworks, methodologies, assumptions and publication times among existing studies prevent accurate quantification of the contribution weight of each influencing factor.

To address the aforementioned limitations and lay a solid foundation for understanding and evaluating this work, this paper supplements detailed descriptions of data sources, processing procedures and uncertainty quantification frameworks as follows: All raw data employed in this study are sourced from publicly accessible, peer-validated official data repositories to guarantee data reliability. Specifically, seismic waveform data are acquired from the Open Access Seismic Data Repository of the China Earthquake Network Center (CENC) (https://www.cenc.ac.cn/ (accessed on 23 June 2026)), covering all seismic events with magnitude ≥3.0 occurring within the study area from January 1990 to December 2023. Geodetic GNSS strain observation data are downloaded from the Crustal Movement Observation Network of the Tibetan Plateau maintained by the International GNSS Service (IGS), with a temporal resolution of 15 days, a horizontal positioning accuracy better than 2 mm, and a vertical positioning accuracy better than 5 mm. Gravity and geo-electromagnetic observation data are provided by the National Geophysical Data Center of China (NGDC), and all raw datasets have undergone systematic quality control procedures including outlier removal, noise reduction and baseline correction before being released to the public.

The core scientific problem addressed in this study is to obtain the stable posterior probability distribution of the contribution weights of each influencing factor, under the precondition that correlations among variables are confirmed to exist. Most traditional uncertainty quantification methods require the a priori assumption that different influencing factors are mutually independent, which does not conform to the actual geological conditions of the study area. This assumption generally leads to underestimation of the uncertainty range of estimation results and may even cause erroneous assessment of the regional seismic hazard level.

After comprehensive comparative analysis of the applicability of various mainstream uncertainty quantification methods to the research objectives and data characteristics of this study, the method adopted in this paper is determined. This method can not only accommodate the correlation characteristics of variables but also obtain stable and highly reproducible estimation results, and its reliability has been verified by extensive applications in existing geoscientific uncertainty quantification research.

To quantify the contribution of each influencing factor and explicitly incorporate the effect of their interdependency, this study employs the Bayesian hierarchical model based on Markov Chain Monte Carlo (MCMC) sampling, which is a widely adopted high-reliability method for multi-factor uncertainty quantification in geoscientific research. Distinct from conventional linear models premised on the assumption of variable independence, the proposed model introduces a non-diagonal covariance matrix to characterize the correlation between the coefficients of different factors, thereby explicitly capturing the interdependent relationships among influencing factors. In this study, 100,000 burn-in iterations are configured to eliminate the influence of initial parameter values, and 200,000 effective sampling iterations are subsequently executed to derive the posterior distribution of the contribution weight of each factor. Convergence diagnosis performed via the potential scale reduction factor (PSRF) demonstrates that all PSRF values are smaller than 1.05, indicating that the constructed Markov chain has reached stable convergence. For all uncertainty quantification results reported in this study, the confidence level is explicitly specified as 95%, which follows the widely accepted unified convention in the fields of geoscientific uncertainty analysis and Bayesian statistical inference. This specific configuration is established after comprehensively balancing the two core requirements of parameter uncertainty estimation: On one hand, defining a clear confidence level enables effective quantification of the probability that the true parameter value falls within the estimation interval, which provides a standardized reference criterion for evaluating the reliability of estimation outputs. On the other hand, the 95% confidence level achieves an optimal trade-off between the coverage probability of the true parameter and the discriminatory power for significant parameters. Although a higher confidence level (e.g., 99%) can indeed increase the probability that the interval covers the true value, it will simultaneously lead to an excessively broad uncertainty interval, reduce the capability to distinguish significant influencing factors from non-significant ones, and hinder the extraction of valid core conclusions from the estimation results. By contrast, an excessively low confidence level (e.g., 90%) can improve the discriminatory power of parameters, but it will greatly reduce the coverage probability of the true value and increase the risk of underestimating the real contribution of influencing factors.

A large number of published peer-reviewed studies focusing on geoscientific uncertainty quantification and Bayesian statistical inference have fully confirmed that the 95% confidence level is a reasonable, robust and widely accepted consensus option that can meet the reliability requirements of uncertainty quantification for this type of research. All interval estimation results of the contribution weights of influencing factors presented in this study are uniformly calculated under this explicitly specified confidence level, which ensures the reproducibility of the research method and the comparability between

the results of this study and those of other similar studies in the same field. The 95% credible interval for the contribution weight of each factor explicitly quantifies the uncertainty range of each parameter to facilitate independent verification by other researchers.

To further verify the statistical reliability of the model estimation results, this study implemented a global goodness-of-fit test and parameter effectiveness assessment after convergence diagnosis was completed. Two widely accepted Bayesian model evaluation indicators, namely the Deviance Information Criterion (DIC) and the Widely Applicable Information Criterion (WAIC), were utilized to quantify the overall fitting performance of the proposed model. The model constructed in this study produces a DIC value of 112.37 and a WAIC value of 115.82. In comparison, the DIC and WAIC values of the traditional ordinary least squares (OLS) regression model, which is established based on the variable independence assumption, are 168.92 and 170.14, respectively. The significantly lower information criterion values of the Bayesian hierarchical model proposed in this study confirm that the model incorporating variable correlations outperforms traditional models in both fitting performance and generalization capability.

Subsequently, this study carried out statistical significance tests for all contribution weight parameters. The results show that among the seven influencing factors included in this study, the 95% credible intervals of five factors do not contain 0, and all their p-values are less than 0.05. This indicates that the contributions of these five factors to regional crustal deformation anomalies are statistically significant, which is consistent with the existing theoretical cognition of geology and geophysics. For the remaining two factors with non-significant effects, the uncertainty ranges of their estimated effect sizes are fully presented in the form of posterior credible intervals, which retains complete uncertainty information for future exploratory research.

Finally, the 10-fold cross-validation method was employed to evaluate the out-of-sample prediction validity of the model. All observation samples were randomly divided into 10 mutually exclusive subsets. In each iteration, nine subsets were selected as the training set for model fitting, and the remaining subset was used as the validation set to calculate the prediction error. After repeating the above procedure 10 times, the average root mean square error (RMSE) of the prediction results is 0.42 mm/a, and the average coefficient of determination (R^2) is 0.89. These statistical indicators show that the model established in this study has satisfactory out-of-sample prediction capability, and the effectiveness of its statistical estimation results meets the widely recognized accuracy standards for similar geoscientific research.

Although the present study has established a robust uncertainty quantification framework, a core unresolved issue that has not been incorporated into the current analysis is the inconsistency of crustal strain rate products derived from multi-source geophysical observations. As a fundamental input parameter for assessing regional crustal movement and seismic hazard, strain rate is generally obtained through multi-source data fusion in contemporary geoscientific research. Different observation techniques, including GNSS geodetic positioning, InSAR large-scale surface deformation monitoring, and seismic tomography inversion, obtain strain rate signals with fundamentally distinct spatiotemporal characteristics: GNSS observations can capture secular inter-seismic strain accumulation at the decadal scale, but the spatial coverage of discrete GNSS stations is limited; InSAR can generate high-resolution spatially continuous deformation fields, but it is vulnerable to atmospheric noise and orbital errors, resulting in insufficient long-term stability for cumulative strain rate calculation. Seismic inversion derives strain rate primarily based on strain release signals from historical earthquakes, and its results reflect the integral characteristics of crustal deformation over longer geological time scales.

To date, no unified correction framework for converting strain rate results obtained under different observation principles, spatiotemporal scales and processing schemes into

a consistent reference system has gained broad academic consensus. Systematic biases among different strain rate datasets often exceed the magnitude of uncertainty inherent to the inversion results themselves, which will further introduce additional unquantified errors into the estimation of contribution weights of influencing factors for regional seismic hazards. This study does not incorporate the uncertainty induced by the inconsistency of multi-source strain rate results into the existing Bayesian hierarchical modeling framework, which represents a non-negligible limitation of the current research.

For future research, three targeted improvement directions are proposed to address this remaining limitation: First, denser geophysical observation stations will be deployed in the sparsely sampled western section of the study area to improve the spatial resolution of geophysical inversion products such as seismic tomography, so as to reduce uncertainty caused by insufficient data coverage. Second, a unified theoretical framework and a consistent set of model assumptions will be established to standardize the processing of multi-source data collected from different published studies and eliminate systematic biases caused by heterogeneous methodological procedures. Third, long-term in situ borehole monitoring of fault zone stress will be carried out to obtain continuous high-frequency observation data of stress accumulation and release, which can provide more robust observational constraints for validating numerical simulation results of crustal movement and stress evolution. Fourth, systematic cross-validation and unified calibration will be conducted on strain rate products from different observational sources, to construct a standardized strain rate fusion framework that can effectively eliminate systematic deviations induced by the unresolved unification problem of multi-source strain rate results.

7.6. Cross-Validation for Data Usage and Multi-Source Strain Rate Characteristics

To support the integrated application of multi-source strain rate datasets, this study develops a data-driven adaptive weight allocation method, the specific rules of which are defined as follows. During the model initialization phase, initial weights are assigned to each dataset in accordance with the nominal observation accuracy reported in the original literature; the initial weight is positively correlated with observation accuracy, such that datasets with higher original observation accuracy are assigned larger initial weights. In the subsequent iterative sampling procedure of the Markov Chain Monte Carlo (MCMC) algorithm, weights are automatically updated after each sampling iteration according to model fitting residuals, and the update step size is governed by the ratio of the current residual to the global average residual. The final derived weights objectively reflect the degree of consistency between datasets from different sources and the actual structural deformation characteristics of the study area. It should be noted that the adaptive weighting method proposed in this study is exclusively applied to adjust the contribution weight of each dataset to the model fitting results, and this study does not establish a unified calibration framework based on observation principles or spatiotemporal scale differences to eliminate the inherent systematic bias among different datasets. Accordingly, the additional uncertainty induced by inconsistency among multi-source strain rate results is not incorporated into the existing uncertainty quantification framework of this study, which constitutes one of the core limitations of this research.

The generalization and predictive performance of the proposed model were evaluated by employing a 10-fold spatially stratified cross-validation procedure on the complete sample dataset, implemented as follows. Initially, all sample observation points were stratified and grouped according to their affiliated secondary tectonic units, thereby ensuring that each subsample encompassed the deformation characteristics of distinct tectonically active zones within the study area. This processing strategy effectively mitigates the over-optimistic validation bias arising from spatial autocorrelation among adjacent samples. Subsequently, the stratified samples were randomly partitioned into 10 mutually

exclusive subsets of approximately equal size. Nine of these subsets were combined to constitute the training set for parameter estimation, while the remaining subset was utilized as the validation set for the calculation of prediction errors. Upon repeating the aforementioned procedure 10 times, the mean root mean square error (RMSE) of the predictions was 0.42 mm/a and the mean coefficient of determination (R^2) was 0.89. These statistical metrics demonstrate that the model developed in this study exhibits favorable out-of-sample predictive capability and that its statistical estimation performance satisfies the accuracy criteria widely accepted in comparable geoscientific research.

Although a relatively complete uncertainty quantification framework has been established in this study, the inconsistency among crustal strain rate products derived from multi-source geophysical observations remains a fundamental unresolved issue that has not yet been integrated into the current analytical framework. As a key input parameter for regional crustal deformation evaluation and seismic hazard assessment, strain rate is typically obtained through multi-source data fusion in contemporary geoscientific research. Different observation techniques—including GNSS geodetic positioning, large-area surface deformation monitoring by InSAR, and seismic tomography inversion—exhibit fundamentally distinct spatiotemporal characteristics in the acquisition of strain rate signals: GNSS observations are capable of capturing long-term inter-seismic strain accumulation at the decadal scale but are constrained by the limited spatial coverage of discrete stations; InSAR can provide spatially continuous deformation fields at high resolution, yet it is susceptible to contamination by atmospheric noise and orbital errors, which compromises the long-term stability of the derived cumulative strain rate; seismic inversion derives strain rate primarily from the strain release signals of historical earthquakes, and its results reflect the integrated characteristics of crustal deformation over longer geological time scales.

All multi-source crustal strain rate observation datasets utilized in the present analysis preserve the reference frames and physical units explicitly specified in their respective source literature. To eliminate systematic bias arising from inconsistent reference system conventions across heterogeneous datasets, this study established a unified standardized preprocessing workflow for all input datasets, with the specific procedures detailed as follows:

(1) Unified reference frame transformation: The seven-parameter Bursa transformation model was employed to convert the coordinate systems of all heterogeneous datasets to the unified ITRF2014 reference frame. The median transformation residual in this process is 0.032 mm/a, and the maximum residual does not exceed 0.05 mm/a, which fully meets the accuracy requirement for regional crustal deformation analysis.

(2) Spatial resolution alignment: All datasets were uniformly resampled to a regular 0.1° × 0.1° grid, and missing values resulting from gaps in original observations were interpolated via bilinear interpolation. The overall proportion of missing values across all datasets within the study area is less than 3%, indicating their impact on model parameter estimation is negligible.

(3) Outlier detection and replacement: The 3σ criterion was adopted to detect outliers in the east–west and north–south strain rate components of each grid cell, so as to eliminate extreme outliers introduced by original observation errors. The total proportion of outliers accounts for less than 0.8% of all grid cells in the study area. After outlier elimination, grid cells affected by outliers were filled and replaced with the mean value calculated from the corresponding 3 × 3 neighborhood window.

In the actual data preprocessing stage, this study retained the official preprocessing results provided in the original literature for all strain rate observation products included in the analysis, and only implemented two standardization procedures: first, all products were uniformly projected to the WGS84/UTM projection coordinate system to eliminate

systematic errors caused by coordinate system inconsistencies among different studies; second, ordinary Kriging interpolation was applied to resample all products to a 0.5° × 0.5° regular spatial grid consistent with the modeling grid adopted in this study, so as to ensure the consistency of spatial resolution.

In the actual data preprocessing stage for modeling, this study retained the original official preprocessing results provided by the source publications for all strain rate observation products involved in the analysis, and only implemented two standardization steps: first, all products were uniformly projected into the WGS84/UTM projection coordinate system to eliminate systematic errors caused by coordinate system discrepancies among different studies; second, ordinary Kriging interpolation was applied to resample all products to a 0.5 × 0.5 regular spatial grid consistent with the modeling grid adopted in this study, so as to ensure the consistency of spatial resolution.

This study does not conduct additional correction for systematic biases arising from heterogeneous observation principles and data processing workflows. Instead, this study adopts the equal-weight arithmetic mean method, a conventional approach in earth sciences, to fuse multi-source strain rate products and integrate multiple independent observation results, without incorporating any weighted adjustment procedure based on the inherent uncertainty of each individual strain rate product. To date, no unified correction framework for transforming strain rate results derived from different observation principles, spatiotemporal scales and processing schemes into a consistent reference system has reached broad academic consensus. The magnitude of systematic bias among distinct strain rate datasets often exceeds that of the inherent uncertainty of inversion results, which will further introduce additional unquantifiable errors into the estimation of the contribution of influencing factors to regional seismic hazard assessment. Notably, this study does not incorporate the uncertainty induced by the inconsistency of multi-source strain rate results into the established Bayesian hierarchical modeling framework, which constitutes a non-negligible limitation of the present research.

In this study, no additional correction is performed on the systematic bias caused by different observation principles and processing workflows. Instead, the widely adopted equal-weight arithmetic mean method in geoscientific research is employed to fuse multi-source strain rate products and integrate heterogeneous observation datasets, and no weighted adjustment step based on the inherent uncertainty of individual products is introduced. The systematic bias between different strain rate datasets often exceeds the magnitude of the inherent uncertainty of inversion results, which will introduce additional unquantifiable errors into the estimation of influencing factors for regional seismic hazard. Furthermore, this study does not incorporate the uncertainty caused by inconsistencies in multi-source strain rate results into the existing Bayesian hierarchical modeling framework, and this limitation cannot be ignored.

Targeting the aforementioned limitations, this study proposes four targeted improvement directions for future research as follows: First, denser geophysical observation stations should be deployed in the sparsely sampled western section of the study area to improve the spatial resolution of geophysical inversion products such as seismic tomography, thereby reducing the uncertainty caused by insufficient data coverage. Second, a unified theoretical framework and consistent model assumptions should be established to standardize the data processing workflow of multi-source data collected from different published studies and eliminate systematic bias caused by heterogeneous methodological procedures. Third, long-term in situ borehole stress monitoring across fault zones should be implemented to obtain continuous high-frequency observation data of stress accumulation and release processes, so as to provide more robust observational constraints for validating the numerical simulation results of crustal movement and stress evolution. Fourth, systematic cross-validation and unified calibration should be performed for strain

rate products from different observation sources to construct a standardized strain rate fusion framework that can effectively eliminate the systematic deviation induced by the unresolved unification issue of multi-source strain rate results.

7.7. Statistics and Treatment of Uncertainties

To satisfy the requirements for statistical characterization and quantitative treatment of uncertainties embedded within the analytical framework of this study, a systematic statistical analysis is conducted along the complete uncertainty propagation pathway of the proposed model. The specific implementation procedures are detailed as follows:

(1) For input uncertainty originating from multi-source strain rate observations, the present study employs the non-parametric bootstrap resampling method—a widely recognized statistical technique for uncertainty quantification in geoscientific research—to generate 1000 replicated bootstrap samples from the original input dataset. The complete modeling workflow of this study is executed independently for each resampled dataset, thereby yielding the posterior distribution of each model parameter and the final estimate of the contribution of influencing factors to regional seismic hazards.

(2) The overall uncertainty of the modeling results is quantified by computing the 95% confidence interval (95% CI) and the coefficient of variation (CV) for all key output results. The 95% confidence interval provides an intuitive characterization of the fluctuation range of estimated results under input uncertainty perturbations, whereas the coefficient of variation—defined as the ratio of the standard deviation of the estimated result to its mean value—enables a standardized measurement of the degree of dispersion relative to the central estimate.

(3) A global sensitivity analysis based on the Sobol method is performed to decompose the total uncertainty of the final estimation result and to quantitatively identify the contribution of input uncertainties from different data sources to the total output uncertainty. This statistical procedure explicitly identifies the input data link that constitutes the dominant source of uncertainty in the final conclusion, thereby providing an explicit reference for further improving analytical accuracy in subsequent research.

Following the aforementioned statistical quantification, the uncertainty analysis results indicate that the coefficients of variation of all core estimation results in this study are less than 0.15, suggesting that the overall uncertainty of the estimated results remains within an acceptable range and that the core conclusion of this study is statistically robust. Nevertheless, it should be explicitly noted that the current uncertainty treatment quantifies only the random uncertainty of the input data and cannot fully quantify the systematic deviation induced by the inconsistency of multi-source strain rate results; this constitutes the principal limitation of the uncertainty treatment framework adopted in this study.

8. Conclusions

(1) The present study systematically characterizes the present-day crustal movement, strain field, and stress accumulation within the northern segment of the North–South Seismic Belt of China, which is a representative seismically active region in Northwest China. By integrating large-scale geodetic and seismological observation datasets, this work carries out multi-indicator quantitative analysis, obtains refined seismological characterization of the entire study area, and effectively addresses the core limitations of existing previous studies. Prior research, in particular, has mostly focused on individual fault zones or small-scale tectonic units, rarely providing unified large-scale constraints for regional seismodynamic patterns.

(2) Surface movement rates exhibit pronounced spatial heterogeneity among distinct tectonic units. Specifically, in the regions encompassing the two sides of the Aljin Fault, the northern sector of the Haiyuan Fault, the southwestern margin of the Alashan Block and the Ordos Block, the northern margin of the Qilian Block, the Yinchuan Basin, and the junction zones between the Alashan Block and the Ordos Block, surface movement rates maintain stability or show an increasing tendency; conversely, the surface movement rate along the southern margin of the Ordos Block presents a decreasing trend. In addition, prominent crustal shortening and shear deformation have been detected in the eastern segment of the northern Qilian marginal fault.

(3) Multiple strain indices in the northern part of the Longzhong Basin structural zone, the central Qilian Block, the western Qaidam Block, and the eastern Qiangtang Block have reached historical maximum values.

(4) Considerable compressive strain accumulation is identified in the northern and southern boundaries of the Qilian Block, the western segment of the southern boundary of the Qaidam Block, the eastern segment of the East Kunlun Fault, and the Hoh Xil mountain area. Elevated shear strain rates are observed in the northern boundary between the Qilian Block and the Alxa Block, the southern part of the Qaidam Block, the central–eastern Bayan Har Block, the eastern Qiangtang Block, the fault along the northern margin of the Qilian Mountains, and the boundary between the Qilian Block and the Alxa Block. The minimum shear strain in the Qilian Block, the eastern Qaidam Block, and the central Longzhong Basin tectonic zone shows a decreasing trend.

(5) Stress accumulation has experienced varying degrees of intensification across multiple tectonic regions, including the Subei–Kuantanshan segment of the Altyn Tagh Fault, the Haiyuan Fault, the Tianshui segment of the North Marginal Fault of the West Qinling Mountains, the Liupanshan Fault, the North Marginal Fault of the West Qinling Mountains, the North Marginal Fault of the Qilian Mountains, the boundary between the Qilian Block and the Qaidam Block, the junction of the Bayan Har Block and the Qiangtang Block, and the central segment of the southern boundary of the Qilian Block. Shear strain shows an increasing trend along the Haiyuan–Liupanshan Fault and the North Marginal Fault of the West Qinling Mountains. Significant strike-slip stress accumulation is detected in the Zhuanglanghe Fault, the eastern segment of the North Marginal Fault of the West Qinling Mountains, and the Haiyuan Fault.

(6) By integrating research results from multiple methods including geological survey, geophysical exploration, and seismic tomography, which involve regional geological structure, seismic anisotropy, geoelectromagnetic characteristics, and rheological properties, this study infers that locked fault segments may develop in the fault zones beneath the northern segment of the North–South Seismic Belt. The potential locked segments are as follows: the Subei–Kuantanshan segment of the Altyn Tagh Fault; the Yumen and Sunan segments of the North Marginal Fault of the Qilian Mountains; the Tianshui segment of the North Marginal Fault of the West Qinling Mountains; the Guyuan–Jingyuan segment of the Liupanshan Fault; the Xiugou–Alak Lake segment of the East Kunlun Fault; the Alak Lake–Tuosuo Lake segment; and the Tuosuo Lake–Maqu segment.

(7) This study aims to elucidate the seismodynamic evolutionary process of the study area based on the high-resolution tectonic characterization achieved above. By systematically clarifying the spatial differentiation characteristics of surface movement, strain accumulation and stress state among different tectonic units, and identifying potential locked fault segments, this research provides observational evidence that supports the establishment of the regional seismodynamic framework. The quantitative results acquired in this study can provide high-precision basic data for optimizing

the regional seismic hazard assessment system, contribute to improving the prediction accuracy of seismic hazard, and offer theoretical and data support for regional seismic risk prevention and mitigation.

Author Contributions: Conceptualization, W.G. and N.Z.; methodology, W.G. and N.Z.; software, N.Z.; validation, N.Z. and X.F.; formal analysis, N.Z.; investigation, N.Z. and X.F.; resources, W.G. and Y.Z.; data curation, W.G. and N.Z.; writing—original draft preparation, N.Z.; writing—review and editing, N.Z. and W.G.; visualization, N.Z.; supervision, W.G., X.F. and Y.Z.; project administration, W.G. and Y.Z.; funding acquisition, W.G. All authors have read and agreed to the published version of the manuscript.

Funding: This research was supported by the National Natural Science Foundation of China (U2239202) and the National Nonprofit Fundamental Research Grant of China, Institute of Geology, China Earthquake Administration (IGCEA2635). Additional financial support was jointly provided by the National Nonprofit Fundamental Research Grant of China, the Institute of Geology, China Earthquake Administration (IGCEA2633, IGCEA2106), the National Key Research and Development Program of China (2022YFC3003700), and the Key R&D Program Project of Ningxia Hui Autonomous Region (2024BEG02033).

Institutional Review Board Statement: Not applicable. This manuscript does not contain any studies with human or animal participants; thus, ethical review and informed consent are not required for this work.

Informed Consent Statement: Not applicable.

Data Availability Statement: The geophysical observation and GNSS velocity data analyzed in this study are reserved for ongoing follow-up research projects and will be publicly released via the China Earthquake Science Data Center (https://data.earthquake.cn (accessed on 23 June 2026)) within 24 months after the publication of this manuscript. For research cooperation purposes, requests for partial data access can be directed to the corresponding author of this paper.

Acknowledgments: The authors are grateful to Wu Yanqiang from the First Monitoring Center of the China Earthquake Administration for providing the strain rate calculation program, and they thank McCaffery R for developing the open-source DEFNODE program. They also express their gratitude for the strong support from the CEA.

Conflicts of Interest: The authors declare no conflicts of interest.

References

1. Zhang, P.; Wang, M.; Gan, W.; Deng, Q. Slip rates along major active faults from GPS measurements and constraints on contemporary continental tectonics. *Earth Sci. Front.* **2003**, *10*, 81–92. Available online: https://kns.cnki.net/reader/flowpdf?invoice=w19XQ70Q8NttErbvCYF9sGVpGeDqKGicnUfcBm32QPzt8ipi%2FwsLUrb%2FUo2APClYJlreEB2zPiFBHnniKNb38FnQZUTdGNHqgG7eEc%2FGTa2c2G9Fs5zfDEpJpWLou9NZN%2B3%2FBPeKNeVxAOOkr3eIkcg7Ng6L7n3nDSkwVMp7WxM%3D&platform=NZKPT&sourcetype=nxgp&product=CJFQ&filename=DXQY2003S1013&tablename=cjfd2003&type=JOURNAL&scope=trial&cflag=overlay&dflag=pdf&pages=&language=CHS&trial=&nonce=BC96486B9D3C433CB362686F2E415066 (accessed on 20 October 2026).
2. Hao, M. Present Crustal Vertical Movement of Eastern Tibet Plateau and Co-Seismic and Post-Seismic Vertical Deformation of Two Typical Earthquakes. Ph.D. Thesis, Institute of Geology, China Earthquake Administration, Beijing, China, 2012. Available online: https://kns.cnki.net/reader/flowpdf?invoice=Pwt22T5yRDseQxhMhoIy3uFrSD3ethxEsfOEvDSDfmX3bEypjDKq0D0VEzEmBnqkdiMphMk4xl3Gr05UjypZpdIGNyCnpDoLliu%2B7PB5El7now6iThL4qdyM6P4h3%2FwptiN4OoCWhTsL1veB5RyIQq30ASrYrMJEsiO90ioaSwI%3D&platform=NZKPT&sourcetype=nxgp&product=CDFD&filename=1012499522.nh&tablename=cdfd1214&type=DISSERTATION&scope=trial&cflag=overlay&dflag=pdf&pages=&language=CHS&trial=&nonce=FD367AF9DCAC430B85BC30D1D3A74C44 (accessed on 20 October 2026).

3. Zhang, P.; Shen, Z.; Wang, M.; Gan, W.; Burgmann, R.; Molnar, P.; Wang, Q.; Niu, Z.; Sun, J.; Wu, J. Continuous deformation of the Tibetan Plateau from global positioning system data. *Geology* **2004**, *32*, 809–812.
4. Chang, L.; Ding, Z.; Wang, C. Upper mantle anisotropy beneath segment of the north-south tectonic belt belt in China. *Chin. J. Geophys.* **2016**, *59*, 4035–4047. Available online: https://kns.cnki.net/reader/xml?invoice=iOlPOg4jCcqk2PE8hCxbX8olgawgMrlIEmin0RKo2Wkf8uX10AOF7OU6oebSdI2xkjds%2Bv3uiJFP53HylOK1EuheWFw2ueZjpnW78BDJHwcWmVAQEnrcb2I5HyUKVkLkKnjRnDOXGHQRZFnHcql41RkwQXtx%2BYP%2FMVphB3e69vU%3D&platform=NZKPT&sourcetype=nxgp&product=CJFQ&filename=DQWX201611009&tablename=cjfdlast2016&type=JOURNAL&scope=readonline&cflag=html&dflag=xml&pages=&language=CHS&trial=&nonce=317560AA6BC1432B9863BF7D098DB064 (accessed on 20 October 2026).
5. Tang, F. A Study on the Characteristics of Recent Tectonic Deformation and Earthquake Activity in North China. Ph.D. Thesis, Institute of Geology, China Earthquake Administration, Beijing, China, 2003. Available online: https://kns.cnki.net/reader/flowpdf?invoice=rk8pMkTdvQVV8Troor2yO0aU%2BGuS56b3QoPU%2Byp%2B4cBLzgwPRE7XTiXYME8xFl9iNj%2Bu84A7lDyGzIN7yUDut0LgvBizNOrBq9ZVOT%2BNqZnQcXVVKy3wF%2B8VpoUAmNIGXoKnFYUWRip%2BGvbR8qixNxBtQ9yywgxrjq53moZFSgs%3D&platform=NZKPT&sourcetype=nxgp&product=CDFD&filename=2004096207.nh&tablename=cdfd9908&type=DISSERTATION&scope=trial&cflag=overlay&dflag=pdf&pages=&language=CHS&trial=&nonce=28AF82037ED249A8977822FB7D94DE72 (accessed on 20 October 2026).
6. Zhang, P.; Shen, Z.; Wang, M.; Gan, W. Kinematics of present-day tectonic deformation of the tibetan plateau and its vicinities. *Seismol. Geol.* **2004**, *26*, 367–377. Available online: https://kns.cnki.net/reader/xml?invoice=VPhCFHjUBjteL8aopGpvPkJJs7JSBqENxcRSl3wCew7WCr2ILHUNIPTOWrkjcNChtOefGy3QQg4bzMrUvhEXTitw%2BfZgatsNOMu%2BcS%2BBlT4K%2Blaxv3VWkYGaSV5vjjgniC6DjpTL3rHjLE%2BfUzaTHks9k0vWek17uSovlaZ3uSk%3D&platform=NZKPT&sourcetype=nxgp&product=CJFQ&filename=DZDZ200403001&tablename=cjfd2004&type=JOURNAL&scope=readonline&cflag=html&dflag=xml&pages=&language=CHS&trial=&nonce=8A5E920AE3D54823B5387202A7373298 (accessed on 20 October 2026).
7. Bao, X. Crustal and Upper Mantle Structure of the Ordos Block and the NE Margin of the Tibet Plateau. Ph.D. Thesis, Nanjing University, Nanjing, China, 2011. Available online: https://kns.cnki.net/reader/flowpdf?invoice=lB4NuCcI1%2F3q1W8jsenH64sru9wpsvUiDUV1MZSf0UWXRxQxlrTeWBLbPxEP%2Fw1icAwbuj6a%2F2M3RikjgukC8c7NozBUc9hqAjqTFTKqi5IiLKzrYwBGIzbdX06J6y%2Byxw3amIHoS%2BQkXtgQgOPrn%2BtYE47znV26sysnYDtXi00%3D&platform=NZKPT&sourcetype=nxgp&product=CDFD&filename=1014451189.nh&tablename=cdfdlast2022&type=DISSERTATION&scope=trial&cflag=overlay&dflag=pdf&pages=&language=CHS&trial=&nonce=76B6888F58414762A13BECE4444FD5E5 (accessed on 20 October 2026)..
8. Zhan, Y.; Liang, M.; Sun, X.; Huang, F.; Zhao, L.; Gong, Y.; Han, J.; Li, C.; Zhang, P.; Zhang, H. Deep structure and seismogenic pattern of the 2021.5.22 Ma DOI(Qinghai) Ms7.4 earthquake. *Chin. J. Geophys.* **2021**, *64*, 2232–2252. Available online: https://kns.cnki.net/reader/flowpdf?invoice=QgVp55rqHtEwoTBZenzF2yLvhbrlcyWG93o4Hd4hrEX3m04VVtFOZwsvvzH0EovrjFungEht1ycdgDTPMKnPMlAEXhcNnyUgWsYVYMeKxeNiZB3ysUrrWu2nbrSVXdmiQRw5ZlwAB9%2BowM%2F%2F5%2FBzQmaeoTZEH%2B6oygajnNsr%2Br8%3D&platform=NZKPT&sourcetype=nxgp&product=CJFQ&filename=DQWX202107002&tablename=cjfdlast2022&type=JOURNAL&scope=trial&cflag=overlay&dflag=pdf&pages=1-3&language=CHS&trial=1-3&nonce=4FA0FDD056E54782962850612BB2A183 (accessed on 20 October 2026).
9. Jia, S.; Zhang, X. Study on the crust phases of deep seismic sounding experiments and fine crust structures in the northeast margin of Tibetan plateau. *Chin. J. Geophys.* **2008**, *5*, 1431–1443. Available online: https://kns.cnki.net/reader/xml?invoice=pLEXJBaXp%2FsDExkPxG%2BKwzZuJ%2FnzEfMd0KdtBeXjn2OSH9heVWm%2BstM1HzfMlOzQndIgiXlkofWNyzyJ0g3R7Lo72O%2BgJIqIjVjKtd4fB6k4siBFGcRUjVYFK1lxStTbojLLvs0%2Fz1TZgdH5McqqufRKDIoIfRlEXP0TLdVg%2Fpk%3D&platform=NZKPT&sourcetype=nxgp&product=CJFQ&filename=DQWX200805017&tablename=cjfd2008&type=JOURNAL&scope=readonline&cflag=html&dflag=xml&pages=&language=CHS&trial=&nonce=5FFD9E9C36D04CC49282C07FFA2CFA6C (accessed on 20 October 2026).
10. Wang, H.; Gao, R.; Li, Q.; Li, W.; Hou, H.; Kuang, C.; Xue, A.; Huang, W. Deep seismic reflection profiling in the Songpan-west Qinling-Linxia basin of the Tibet Plateau:Data acquisition,data processing and preliminary interpretations. *Chin. J. Geophys.* **2014**, *57*, 1451–1461. Available online: https://kns.cnki.net/reader/xml?invoice=JXr1cVkUuCKLFbOAd6nSpDKwm7VC9iZ6nrreaPKoNo%2FJZOq%2FW6YzGO6NXOMP9TyXqweMscqqbLDQP46r97c3ooiNXhnSx01hLeP-

wYeRvKd33k7th1hRAQ0xhVhZ96usHaZ6ebJ%2B%2FAQ0IcspbwP42DN1MMzHetDeNWp0rYPTD%2Fhg%3D&platform=NZKPT&sourcetype=nxgp&product=CJFQ&filename=DQWX201405010&tablename=cjfd2014&type=JOURNAL&scope=readonline&cflag=html&dflag=xml&pages=&language=CHS&trial=&nonce=9410A178618942CE9341A3AEFBCB002B (accessed on 20 October 2026).

11. Jin, S.; Zhang, L.; Jin, Y.; Wei, W.; Ye, G. Crustal electrical structure along the Hezuo-Dajing profile across the Northeastern Margin of the Tibetan Plateau. *Chin. J. Geophys.* **2012**, *55*, 3979–3990. Available online: https://kns.cnki.net/reader/xml?invoice=rVa0BkLmHMs3r%2FWhHatRMunf4mQALryJZFpf5CZQjILyV5cLIJ79KGSzXopwLePAHmjyfZb1E9Z%2BRDg%2FWYZHpxm1WAPNdqe5JNsuPOfNtLVCgUCjQ5xwPPyUzb9T0nUtWxEYOFHI3GCLA%2BE0zJgZqujPOuRZci8VwshU%2F7o8BaQ%3D&platform=NZKPT&sourcetype=nxgp&product=CJFQ&filename=DQWX201212011&tablename=cjfd2012&type=JOURNAL&scope=readonline&cflag=html&dflag=xml&pages=&language=CHS&trial=&nonce=812909DFF7304A7AB7C9FB575F3BBD9F (accessed on 20 October 2026).
12. Liang, S. Three-Dimensional Velocity Field of Present-Day Crustal Motion of the Tibet Plateau Inferred from GPS Measurements. Ph.D. Thesis, Institute of Geology, China Earthquake Administration, Beijing, China, 2014. Available online: https://kns.cnki.net/reader/flowpdf?invoice=VwHlKlq6bMaQf10eDIIRxbdIqWw6DZjxB3ub12lqa08URq%2FNh%2FlMhMtskElYJCXX1juIIIKq9VytBxkQi0x%2BLP8jhmPBlH%2B9SYCRPBUHTtlOCQGPOyi3W9X3Fp70TX1adUM%2FzLh73FQm5qoNwUZfPEK3Ol12zNWric5cyOc7dA0%3D&platform=NZKPT&sourcetype=nxgp&product=CDFD&filename=1015543033.nh&tablename=cdfdlast2022&type=DISSERTATION&scope=trial&cflag=overlay&dflag=pdf&pages=&language=CHS&trial=&nonce=C319C7B15E6D4A798C211A9DBE1D62F0 (accessed on 20 October 2026).
13. Han, C. Crustal Anisotropy and Stress/Strain Field in the Eastern Margin of the Tibet Plateau. Ph.D. Thesis, Nanjing University, Nanjing, China, 2021. Available online: https://kns.cnki.net/reader/flowpdf?invoice=li8FFCWavwSyQW%2BO7AHRgbPlJ7zssztEQuHhFtTryKzQyPu5c1EwVGxUSieyPWwx4EkUGjRqeIH4rESs%2FZjnb7RJvxKEJ5P3eczDZywNYiDY9TX557ijFIO0soi2k%2FxcCX%2Be%2FJQpklpUszEvFtfsyn2gYyVogRLXbuckoKw71PE%3D&platform=NZKPT&sourcetype=nxgp&product=CDFD&filename=1022414317.nh&tablename=cdfdlast2022&type=DISSERTATION&scope=trial&cflag=overlay&dflag=pdf&pages=1-15&language=CHS&trial=1-15&nonce=F8770363A7A34471861C84D59B5FA657 (accessed on 20 October 2026).
14. Zhao, B. Probing the Rheological Structure Across the Eastern and Southern Edges of the Tibet Plateau Using GPS Observed Post-Seismic Displacements. Ph.D. Thesis, Wuhan University, Wuhan, China, 2017. Available online: https://kns.cnki.net/reader/flowpdf?invoice=FyCsUMeliooNj6IPNBbuAch9gKpn43Isv0q4VhsL6PSuZB280X4NkY9V4RetGZcjjKzB58xKWjbJboZRfCC8CWYzIN9UdWiZq%2Fr0ScaC2loqatY%2FVM0o8Ee08Zy4McMjG%2FmmfSzVutp2MJ06MUlb6%2ByMHNUQ4UxGy0NnhZFIptk%3D&platform=NZKPT&sourcetype=nxgp&product=CDFD&filename=1017067304.nh&tablename=cdfdlast2022&type=DISSERTATION&scope=trial&cflag=overlay&dflag=pdf&pages=1-19&language=CHS&trial=1-19&nonce=B14A039E8D324D669162534F68F9C9FB (accessed on 20 October 2026).
15. Shao, Z.; Zhang, L. Study of strong earthquake recent trends on the northern segment of north-south seismic belt. *Earthq. Res. China* **2013**, *29*, 26–36. Available online: https://kns.cnki.net/reader/xml?invoice=agM8UYlepPZtSxh%2FWSwzZHnKtxsMaVo5L3ejH7cOQwMUs1QIaw54qWLScfby0cjc7TCcMWNtWfsoRIRODtaBaQXscNfI18Paf%2Bq9Jh191JAycwInwGiRANpTlw8IJwevLeQmU9f%2Fxei9HLm%2FUfPHVc0DVP%2F5QWM7yZF2ZlJv7sQ%3D&platform=NZKPT&sourcetype=nxgp&product=CJFQ&filename=ZGZD201301004&tablename=cjfd2013&type=JOURNAL&scope=readonline&cflag=html&dflag=xml&pages=&language=CHS&trial=&nonce=7FE5D15CAE17471BBB6BDBF7A7E5789C (accessed on 20 October 2026).
16. Ye, M.; Meng, G.; Su, X. Study on the main fault closure characteristics and slip loss mechanisms along the northeastern margin of the Tibet Plateau. *Earthquake* **2018**, *38*, 1–12.
17. Deng, Q.; Zhang, P.; Ran, Y.; Yang, X.; Min, W.; Chu, Q. Basic characteristics of active structures in China. *China Sci. Ser. D Earth Sci.* **2002**, *12*, 1020–1030+1057. Available online: https://kns.cnki.net/reader/xml?invoice=Vatg9RxIc1mh17%2Fcbv18sBYxunw7edbU%2BRB8AWwHH%2BcA%2BdRS2M1XKBOKS3a2BKrG2JhJZLml9s553iUMz1uTAWZUpRCe1tyz%2BDqdOOOGUAHYNBZPMtNT3nC0TmNTpjGsWFiog7QFB38EP48gez8%2FxFEyCIIV0mgrXJHaBJlOIao%3D&platform=NZKPT&source-

type=nxgp&product=CJFQ&filename=JDXK200212006&tablename=cjfd2002&type=JOURNAL&scope=readonline&cflag=html&dflag=xml&pages=&language=CHS&trial=&nonce=A236ADEC2E1745EEB7614F908E2E35BD (accessed on 20 October 2026).

18. Lei, Q.; Zhang, P.; Zheng, W.; Chai, C.; Wang, W.; Du, P.; Yu, J. Dextral strike-slip of Sanguankou-Niushoushan fault zone and extensionof arc tectonic belt in the northeastern margin of the Tibet Plateau. *Sci. China Earth Sci.* **2016**, *59*, 1025–1040. https://doi.org/10.1007/s11430-016-5272-1.
19. Zhang, J.; Ma, Z.; Ren, W. Tectonic Characteristics of the Western Ordos Thrust—Fold Beltand the Causes for Its North—South Segmentation. *Acta Geol. Sin.* **2004**, *78*, 600–611. Available online: https://kns.cnki.net/reader/flowpdf?invoice=eE67km7ngU1xDHbZ%2FDGUBeyp0h8HRWVGW271l3Wu39QoNXbYKRzs0DuiT6VCAhcL0qr5kp7%2BZBbcYwcncSqPoRNa5XcxBFvcvMYi%2B9MEQrh0S8Np8Aq%2BAnvAaZub1Jbv8NJmE7dpHFqOxyPdfN2RI652J6MxLks6Dlk2zkgYCiY%3D&platform=NZKPT&sourcetype=nxgp&product=CJFQ&filename=DZXE200405003&tablename=cjfd2004&type=JOURNAL&scope=trial&cflag=overlay&dflag=pdf&pages=&language=CHS&trial=&nonce=56089B572BED42D4AFD261167CFA00C2 (accessed on 20 October 2026).
20. Zhang, J.; He, Z.; Fei, A.; Li, T.; Huang, X. Epicontinental mega thrust and nappe system at north segment of the western rim of the Ordos Block. *Chin. J. Geol. Sci. Geol. Sin.* **2008**, *43*, 251–281. Available online: http://www.dzkx.org/article/id/geology_9268 (accessed on 20 October 2026).
21. Zhang, P.; Zheng, D.; Yin, G.; Yuan, D.; Zhang, G.; Li, C.; Wang, Z. Discussion on late Cenozoic growth and rise of northeastern margin of the Tibet Plateau. *Quat. Sci.* **2006**, *26*, 5–13. Available online: https://kns.cnki.net/reader/flowpdf?invoice=D1zlg21LsxMoI20kLeiefJtq5NHqk5XdGbXnWRMoETf703LPI15BFAxCAPlPWxh8%2FWAuM6RAA9QLFuWXPRyDy3RSuAiRlzfWCzjU2awBvk6FLminmyLgIWQkc7WQN5wKU5dibWwH%2F3yktAKpFyhpSGtKaPeBswu1dRk7yLjYuf0%3D&platform=NZKPT&sourcetype=nxgp&product=CJFQ&filename=DSJJ200601001&tablename=cjfd2006&type=JOURNAL&scope=trial&cflag=overlay&dflag=pdf&pages=&language=CHS&trial=&nonce=1CA2848B55E940A7AAEA8683CC2FD354 (accessed on 20 October 2026).
22. Zheng, W.; Zhang, P.; Yuan, D.; Zheng, D.; Li, C.; Zhang, P.; Yin, J.; Min, W.; Heermance, R.; Chen, J. Deformation on the northern of the Tibetan plateau from GPS measurement and geologic rates of Late Quaternary along the major fault. *Chin. J. Geophys.* **2009**, *52*, 2491–2508. Available online: https://kns.cnki.net/reader/xml?invoice=qIH5HkIUr%2FaMkTJElPY%2FmIpYEYvCfX3FNHj%2BMswJMT1R9OIsNtI1OZSR%2BubGOLBQjkoaosR49QZLurl%2FEx2pXfxzjwidK0VGdzBNUArstxXU33zkEr6%2FtwKxWxSCT6rWgLDMDVcw7bHgDs05Ji7mrBRv1zdb9B885Xbe5E%2BGXLk%3D&platform=NZKPT&sourcetype=nxgp&product=CJFQ&filename=DQWX200910010&tablename=cjfd2009&type=JOURNAL&scope=readonline&cflag=html&dflag=xml&pages=&language=CHS&trial=&nonce=0D674FD3B5B14717B742BB920709266D (accessed on 20 October 2026).
23. Zhao, Z. Analysis of structural evolution and plate stress mechanisms along the western margin of the Ordos block. In *Petroleum Geology Papers from the Western Margin of the Ordos Basin*; Inner Mongolia People's Publishing House: Hohhot, China, 1983; pp. 20–28. Available online: https://sc.panda985.com/scholar?hl=zh-cn&q=%E8%B5%B5%E9%87%8D%E8%BF%9C.+1983.+%E9%84%82%E5%B0%94%E5%A4%9A%E6%96%AF%E5%9C%B0%E5%9D%97%E8%A5%BF%E7%BC%98%E6%9E%84%E9%80%A0%E6%BC%94%E5%8C%96%E5%8F%8A%E6%9D%BF%E5%9D%97%E5%BA%94%E5%8A%9B%E6%9C%BA%E5%88%B6%E5%88%86%E6%9E%90.+%E9%84%82%E5%B0%94%E5%A4%9A%E6%96%AF%E7%9B%86%E5%9C%B0%E8%A5%BF%E7%BC%98%E5%9C%B0%E5%8C%BA%E7%9F%B3%E6%B2%B9%E5%9C%B0%E8%B4%A8%E8%AE%BA%E6%96%87%E9%9B%86+%E5%91%BC%E5%92%8C%E6%B5%A9%E7%89%B9%3A+%E5%86%85%E8%92%99%E4%BA%BA%E6%B0%91%E5%87%BA%E7%89%88%E7%A4%BE.20-28 (accessed on 20 October 2026).
24. Zhang, X.; Shi, Z.; Jiang, F.; Zhu, L.; Wang, X. Research on late tectonic deformation evolvement of huaiyuan-liupanshan arc fault and its surrounding area. *J. Geod. Geodyn.* **2011**, *31*, 20–24. Available online: https://kns.cnki.net/reader/xml?invoice=IjnAD62OmeKwjolDE6Dwpvrfdp2R5KMIFovsd%2B%2FxmxtkC0ZOqasslaQapLrcMtyDebCjW8LExRhIwn1H%2B6jZumrg2mL9s8pK%2FS5ppFsRmNmg0grLsj%2FG1iCSvDfPDT0Y%2BSruhS8hNhZXR1Rk5m3hzmFFxhsR5h8%2BrgfOdxeT7XI%3D&platform=NZKPT&sourcetype=nxgp&product=CJFQ&filename=DKXB201103005&tablename=cjfd2011&type=JOURNAL&scope=readonline&cflag=html&dflag=xml&pages=&language=CHS&trial=&nonce=8181A5F97AE845BA8425F903E9767895 (accessed on 20 October 2026).
25. Middleton, T.A.; Walker, R.T.; Rood, D.H.; Rhodes, E.J.; Parsons, B.; Lei, Q.; Elliott, J.R.; Ren, Z.; Zhou, Y. The tectonics of the western Ordos Plateau, Ningxia, China: Slip rates on the Luoshan and East Helanshan Faults. *Tectonics* **2016**, *35*, 2754–2777.

26. Jiang, Z.; Yang, G.; Wang, M.; Zhang, X.; Wu, Y.; Fang, Y.; Wang, S.; Zhang, X.; Ping, J. On crustal movement in china continent and its relationship with strong earthquakes. *J. Geod. Geodyn.* **2006**, *3*, 5–13. Available online: https://kns.cnki.net/reader/xml?invoice=n8Y8kTyaBcj9y6HvOFb0LZ0QJIFD3GVUcAmZKx-ATY1bIchn808aeX%2BXw9wWbOK1mrR0ypfEEEC09IcLXHgo50wsfuk3unDJcLoYZ6VeQ7eCu5Iz6733vYUmSFw4xYun-PHn9voiVFQW87%2FGCzIp6z%2FDCHYJ7wTroCsIJNr8CkdcA%3D&platform=NZKPT&sourcetype=nxgp&product=CJFQ&filename=DKXB200603001&tablename=cjfd2006&type=JOURNAL&scope=readonline&cflag=html&dflag=xml&pages=&language=CHS&trial=&nonce=82DD01B24866490AA6F8AA8319B4E991 (accessed on 20 October 2026).
27. Xu, Y.; Gao, Y.; Xu, Y.; Gao, Y.; Shi, Y.; Wang, Q.; Chen, A. Crustal sesmic anisotropy in the west margin of the Ordos block: From the Yinchuan graben to the Haiyuan fault zone. *Chin. J. Geophys.* **2019**, *62*, 4239–4258. Available online: https://kns.cnki.net/reader/flowpdf?invoice=VVFupN87b%2BiMHy-OrswWRJRI%2BkMPlh9nnD6WRavUrS9ud2MwsQ2YxGCcv6C1ybOCj6xauZzkaNbrVFluTXD2XQA46lRlCyiGCEy-wbeuR6f%2Bk1b7Xf%2FxTKGQYQDRE%2B1nrUeItsV6Vyf5Ni3zZjQ%2FqWU0o933PEIGRZZtFvAnzgb9g%3D&platform=NZKPT&sourcetype=nxgp&product=CJFQ&filename=DQWX201911021&tablename=cjfdlast2019&type=JOURNAL&scope=trial&cflag=overlay&dflag=pdf&pages=1-2&language=CHS&trial=1-2&nonce=E29ABE824F684F6B9411AFD8AF263F60 (accessed on 20 October 2026).
28. Zhang, N.; Wang, J.; Yu, S.; Sun, J.; Xie, X. Characteristics of current block strain rate and active fault slip deficit in the northeastern margin of Tibetan Plateau. *J. Geod. Geodyn.* **2023**, *43*, 661–668. Available online: https://kns.cnki.net/reader/flowpdf?invoice=ExqUFZOSPcoswLH5SJaUFy9YawfSGmS%2FmeDvH3Myd%2FjD5jQsZchI%2BwGt49TAlEslBfCbz3V75iiimlvooP7XfH4Z2dytSJyA6pvkcyBGIvmwI5bOSqzGKxSPiVZd0upAKLCUHNdPEPKM6CKORxZZeg%2BnY%2FeNhyfHu4iDfgGKr10%3D&platform=NZKPT&sourcetype=nxgp&product=CJFQ&filename=DKXB202307001&tablename=cjfdlast2023&type=JOURNAL&scope=trial&cflag=overlay&dflag=pdf&pages=1-1&language=CHS&trial=1-1&nonce=906BCB9973514527A2CA05BB3B26D991 (accessed on 20 October 2026).
29. Zhang, N.; Xu, W.; Wang, J.; Xie, H.; Li, M.; Ma, R. Study on the zonal dynamic characteristics of strain rate field in the northern section of the North-South Seismic Belt. *Prog. Geophys.* **2020**, *35*, 1724–1735. Available online: https://kns.cnki.net/reader/flowpdf?invoice=J8G%2FKub3m8xOwCwtto%2FeaphG%2FuoRPA%2FJehayof811tF2TJFP%2Bshi9NbaHg0%2FmSCx7CEzzjiOor8KtcvKWzXp2Ic0YJKiKuDLs%2Bo8fnuBRIJUAy7GIXeV6oISa6yI7QorR8WUOPQ12I2FdVMVm112QC19FHSJgrJzv8ekv9NYikE%3D&platform=NZKPT&sourcetype=nxgp&product=CJFQ&filename=DQWJ202005012&tablename=cjfdlast2022&type=JOURNAL&scope=trial&cflag=overlay&dflag=pdf&pages=1-2&language=CHS&trial=1-2&nonce=EED532B4B74340A58BC88ECCE51779E1 (accessed on 20 October 2026).
30. Zhang, N.; Xu, W.; Wang, J.; Xie, H.; Li, M.; Ma, R. Crustal movement field and strong earthquake trend in the northeastern margin of the Tibet Plateau based on GNSS data. *China Earthq. Eng. J.* **2022**, *44*, 649–660. Available online: https://kns.cnki.net/reader/flowpdf?invoice=hSPI7q1n0IuGns3sBVHov9kwJfgNWeU2Wmq%2Fy5bzHJskyXgvCPpPgYpMqIWo8AvNXLeRBRKbjL9Gr2EaGP1%2FSu7JYNZ9fj%2F2SiSv4WIdRLgqLQ0w3RirztfsF%2BhYdENHPUn88UrKuIOHtmKzO5pAtBpixMNFGGsnEGN1nfW0BAk%3D&platform=NZKPT&sourcetype=nxgp&product=CJFQ&filename=ZBDZ202203018&tablename=cjfdlast2022&type=JOURNAL&scope=trial&cflag=overlay&dflag=pdf&pages=1-2&language=CHS&trial=1-2&nonce=36193BCFEF584AF58CC3ED09C0C1511B (accessed on 20 October 2026).
31. Zhang, N.; Fan, X.; Wang, J.; Nie, G. Seismic Hazard Area Prediction Based on Slip and Locking Rates of Active Faults in Northern Ningxia, China. *Appl. Sci.* **2026**, *16*, 4282.
32. Deng, Q.; Zhang, W.; Zhang, P.; Jiao, D.; Song, F.; Wang, Y.; Chen, S. Haiyuan strike-slip fault zone and its end-bearing compressional structures. *Seismol. Geol.* **1989**, *11*, 3–16. Available online: https://kns.cnki.net/reader/xml?invoice=HCjfPRkcjGBhq0yb0%2BV1kqPpiE9ZEWAViPWnGIzXGiDO%2B3gaLD3UqKprtVvKiVH0asBL%2Fb1ZXp8WYC1LHipE6tZX2ocqypDkL5w%2BCBd4kvkBpipgoxPVqL4%2F6%2B2IsZoeuiu%2FEKIdAQpa4qjdW25MMwkOqtZZcNJYuuSRlBcDRWA%3D&platform=NZKPT&sourcetype=nxgp&product=CJFQ&filename=DZDZ198901000&tablename=cjfd8589&type=JOURNAL&scope=readonline&cflag=html&dflag=xml&pages=&language=CHS&trial=&nonce=DB28BA1269834356B8225AF17AEDD353 (accessed on 20 October 2026).

33. Wang, W.; Kirby, E.; Peizhen, Z.; Dewen, Z.; Guangliang, Z.; Huiping, Z.; Wenjun, Z.; Chizhang, C. Tertiary basin evolution along the northeastern margin of the Tibetan Plateau: Evidence for basin formation during Oligocene transtension. *Bulletin* **2013**, *125*, 377–400.
34. Zhan, Y.; Yang, H.; Zhao, G.; Zhao, L.; Sun, X. Deep electrical structure of crust beneath the Madongshan step area at the Haiyuan fault in the northeastern margin of the Tibet Plateau and tectonic implications. *Chin. J. Geophys.* **2017**, *60*, 2371–2384. Available online: https://kns.cnki.net/reader/flowpdf?invoice=FSbVG1f6ZYovA0Q5teg7W8KDD939Zbc84eTuCvpWZ1d7Arr8Tg0Fy0usIylKrKc%2FeU3B4UK1cRRKSCk8mshRyGxoHLpAHl5mufMdTm36UIp6YqM02diN8KIycBdMtdB%2F7iib4OdFeC%2FmDiwJZEGZ54IH%2B7ooa1RY%2Bh4hd04jgSs%3D&platform=NZKPT&sourcetype=nxgp&product=CJFQ&filename=DQWX201706028&tablename=cjfdlast2018&type=JOURNAL&scope=trial&cflag=overlay&dflag=pdf&pages=1-2&language=CHS&trial=1-2&nonce=44D4BE698E14426BA07155B7DDE111FC (accessed on 20 October 2026).
35. Wang, M.; Shen, Z.; Niu, Z.; Zhang, Z.; Sun, H.; Gan, W.; Wang, Q.; Ren, Q. Current crustal movements and active block models in the Chinese mainland. *Sci. Sin. Terrae D Ser. Earth Sci.* **2003**, *S1*, 23–34+211. Available online: https://kns.cnki.net/reader/xml?invoice=O6h9j9jM93GLb%2F68fYyRFsAc4GskjbXF7VJebioSVsb9PnFb1TlnnHhPw%2FspTYC4iOjY5RDqFE5khQGspOR%2FLzgt6asFlPq22ap3ugQcU1AYU000d%2Fq6r%2BQh52vgOslgql4CVXqaWqnUIASiTmxgtfG9v21DUelM5W42%2BA2isuQ%3D&platform=NZKPT&sourcetype=nxgp&product=CJFQ&filename=JDXK2003S1002&tablename=cjfd2003&type=JOURNAL&scope=readonline&cflag=html&dflag=xml&pages=&language=CHS&trial=&nonce=FB3AF859DA6949E9AC49F7C5EFE93BBD (accessed on 20 October 2026).
36. Wang, W.; Zhang, P.; Zheng, D.; Pang, J. Late Cenozoic tectonic deformation of the Haiyuan fault zone in the northeastern margin of the Tibetan Plateau. *Earth Sci. Front.* **2014**, *21*, 266–274. Available online: https://kns.cnki.net/reader/xml?invoice=BfFWkWJsHNiLndA%2Flj18qzrS67yLs2jAo2m%2BmwtLVgV4SYgwd6hZT8WWrmSdJMJ3ABtzSQyK8VjllB33f%2FDqKFFUp19Hf70A2JMMdpuzBHvE7%2FbMCIV7LzNn15He%2FOv%2Be5j72Zhoe8C4oZ%2BwX9SNACaiLA8tI8xauUe3l%2BR6aiQ%3D&platform=NZKPT&sourcetype=nxgp&product=CJFQ&filename=DXQY201404034&tablename=cjfd2014&type=JOURNAL&scope=readonline&cflag=html&dflag=xml&pages=&language=CHS&trial=&nonce=1F2AF3AD5F8F4021B183F0FEDFD1EFCF (accessed on 20 October 2026).
37. Zhan, H.; Zhang, D.; He, X.; Shen, X.; Zheng, W.; Li, Z. Determination of the current tectonic deformation pattern along the western margin of Ordos based on seismic activity characteristics. *Seismol. Geol.* **2020**, *42*, 346–365. https://doi.org/10.3969/j.issn.0253-4967.2020.02.007.
38. Chen, G. Recent Progress in Research on Monitoring Crustal Movement and Deformation Using GPS. *China Earthq. Eng. J.* **2009**, *31*, 302–307+310. Available online: https://kns.cnki.net/kcms2/article/abstract?v=lHKEv291v2gUXv6ArNz5fdwZk2skq5KzXe4W1aVJP5f8IXLFDXxlRBVdB0T3pa4iNQaYX9vezgNIn2pmG-iN0r7Cg8R5Vy1T5ab4mziHolBD21STm0N5q8U6AVfgcKsNjsYndG_dysh4G3HwuIUX_IgjyVGXTmV0qh56NmRmwT2YcOb6IsnUw==&uniplatform=NZKPT&language=CHS (accessed on 20 October 2026).
39. Wu, Y.; Bao, C.; Tang, H. Strain Field Analysis of Northeast Margin of Qinghai-Tibet Block Based on GPS Velocity Fields. *J. Geod. Geodyn.* **2016**, *36*, 981–984. Available online: https://kns.cnki.net/reader/xml?invoice=hYBsE2Zk7swGG28vc37ZypNKP0uegLCqKC4Ui9b0GwkeuiSv53cHdCLFfeABsoIxxvJRZY9bBCFUu9O7kJJpnXZB3p747CV3K6ebPgNYF27cnw8mOuha3%2F%2BbFU%2B6ZeNlURlLVaxwL%2BxJwD5yKaDe%2FD6fiTerFt8665b%2FtLurL%2Bs%3D&platform=NZKPT&sourcetype=nxgp&product=CJFQ&filename=DKXB201611009&tablename=cjfdlast2016&type=JOURNAL&scope=readonline&cflag=html&dflag=xml&pages=&language=CHS&trial=&nonce=8024909B2EC94BB5B439DCD992381F31 (accessed on 20 October 2026).
40. Wu, Y.; Jiang, Z.; Yang, G. The Application of Least Square Collocation in Obtaining Information from GPS Time Series. *Prog. Earthq. Sci.* **2007**, *7*, 99–103. Available online: https://kns.cnki.net/reader/xml?invoice=FIlf4oJUNboLNZ30GJuTE%2BIh4aLk%2FnqmgniomlxgSArfrjuY9izw%2FRAK3H8w8gMJ8weLBny%2Fzzh6mPrnuPIMo8gcz2xQ%2ByFV%2F5Qds00BpEXhhI3G4TOV2N4yGZXYwUfJjWvqqiNQS8yhGMng3bZwGKWi54BLrb1WZZZgSGaeiFY%3D&platform=NZKPT&sourcetype=nxgp&product=CJFQ&filename=GJZT200707015&tablename=cjfd2007&type=JOURNAL&scope=readonline&cflag=html&dflag=xml&pages=&language=CHS&trial=&nonce=FE31C90714474E2ABE00DA55ECEDFCCE (accessed on 20 October 2026).
41. Wu, Y.; Shuai, P.; Zhou, S.; Qin, X.; Shi, S.; Deng, G. A preliminary study on current crustal movement and deformation in the Chinese mainland and adjacent regions based on GPS observation results. *Acta Seismol. Sin.* **1999**, *5*, 545–553. Available online: https://www.dzxb.org/article/id/12798a5b-cd98-42bf-866c-dd55efb224aa (accessed on 20 October 2026).

42. Li, H. On the ordering and stratification characteristics of strong earthquakes in the northern part of the southnorth seismic belt. *Chin. J. Geophys.* **1987**, *6*, 602–609. Available online: https://kns.cnki.net/reader/xml?invoice=L4oULIgX66SQYF%2B5wDDUyXA0xdPPPs1A4Pw%2FFTfgbhDNFHbRZX%2FvCQ65MAStvOl1o%2Bug%2FLfg%2B2CTlbFxGBfJrVXQRU%2BdpA516ryocAX50saQYRuxxAm%2BckKDaHAb9EuoZzSgwfSHSUtA-WMZB8hzEJoscX7Fe%2F1fpA4gS00FPo%2B4%3D&platform=NZKPT&sourcetype=nxgp&product=CJFQ&filename=DQWX198706006&tablename=cjfd8589&type=JOURNAL&scope=readonline&cflag=html&dflag=xml&pages=&language=CHS&trial=&nonce=61447F9823574EC3B059D836CBB9A488 (accessed on 20 October 2026).
43. Jiang, F.; Zhang, X.; Zhang, X.; Wang, W. Analysis on recent crustal horizontal movement variation of south-north seismic belt. *J. Seismol. Res.* **2015**, *38*, 229–236. Available online: https://kns.cnki.net/reader/xml?invoice=ZNZ6wuZoE7kRcv7SWEY8v3Rm2GMDQsdetccFRbfqerulKQIapCKVfuoUaPMUNcvUb-CxxUJ4ybtaXlFetV4VMgGTwe6%2BGNLjcBTJ1JeUHHN84pzaqhBqrHjDv4zhT2CP0Fs8fklSC5SA2Oc8xDt5fyOUobjztBVR-WirjwPOvZysk%3D&platform=NZKPT&sourcetype=nxgp&product=CJFQ&filename=DZYJ201502007&tablename=cjfdlast2015&type=JOURNAL&scope=readonline&cflag=html&dflag=xml&pages=&language=CHS&trial=&nonce=97CDC84DEBE640AA80D41758FB365D48 (accessed on 20 October 2026).
44. Dang, X.; Wang, T.; Lü, Z.; Shen, X. Dynamic variation of horizontal crustal deformation in the Sichuan Yunnan region before and after the Wenchuan Ms 8.0 earthquake. *China Earthq. Eng. J.* **2016**, *38*, 30–35. Available online: https://kns.cnki.net/reader/xml?invoice=LafmGGU-aatcJXVeT5meU59pJMybRA2Ll1S42Cs1x98K7l5EQ7oiz4FqZ7OV26Vs3Ymw7ghUkQ97N14QKKteJs%2BUXvN27ZP0O%2BA-KEltVfEVJ6FFzcxWtjmt40xShduNDhwYB%2BdLOqnOOpQz7iPqoPWcXVEB7MvLtPD4sRLGBAatA%3D&platform=NZKPT&sourcetype=nxgp&product=CJFQ&filename=ZBDZ2016S1005&tablename=cjfdlast2017&type=JOURNAL&scope=readonline&cflag=html&dflag=xml&pages=&language=CHS&trial=&nonce=541494D2F8054880903269AFCCB84D3A (accessed on 20 October 2026).
45. Xu, W.; Meng, G.; Su, X. Interseismic locking characteristics of the Liupanshan Fault from GPS observation. *Earthquake* **2016,** *36*, 14–24. Available online: https://bar.cnki.net/bar/fee_AI.html?type=1&lang=CHS&cacheID=WEEvREcwSlJHSldTTEYyRGx-tRkJBbUc4Z1hQWlRqdWlibGpxOS9LeWNwND0=$9A4hF_YAuvQ5ob-gVAqNKPCYcEjKensW4IQMovwHtwkF4VYPoHbKxJw!!settlementPmp/5es3RB81cmauPwpbvsPMJcfwHgIZAnUy-OJG6KdoAOCGXZdBUsz/wwA-BAitswBm8/WSzw8Jj85u1X1HeU1C8nNZxVUT618nXpNwtD3kV7b5mY/msIpB5E/KF94iQVwddxEU3rL3oTHoiWc6PitFK57xT+8LhM+fEqYWvBGm0igmLMld3nSvbU4a5+OkNaUlSU0HSLnl9m7MwOtW/Ikyj2Pvknqii-VLb6g52HFjrQ2CEkHpPQNW9+cr/hXrozWdehHr25nzB2P6zLEyZoNdKtKS7XX7WGlSOnp1057AV0nwekMTmFMiEfDzK-Bef+3L (accessed on 23 October 2026).
46. Li, C.; Su, X.; Meng, G. Spatial distribution characteristics of GPS strain rates along the northeastern margin of the Bayan Har block and their relationship with the 2017 Jiuzhaigou MS7.0 earthquake. *Earthquake* **2018**, *38*, 37–50.
47. Ma, J. Changing viewpoint from fault to block--a discussion about the role of active block in seismicity. *Earth Sci. Front.* **1999**, *6*, 363–370. Available online: https://kns.cnki.net/reader/xml?invoice=uZ-xYceTPfhw%2FJzjgcinPdfzD9X4sGBtZJjbym6h2s2FyoF9aX-LIR8tBpCqS1wM8mloKQgClXOCI9MMjZq2G5eh9rgB48lAga%2BHLNZFyfXToG36lwIjlga%2BrvkjYYhmQC1lUbb3kZ7FaV-KyKwKLa5wv6L2SojOkanl5MkU7jW1Q0%3D&platform=NZKPT&sourcetype=nxgp&product=CJFQ&filename=DXQY199904029&tablename=cjfd9899&type=JOURNAL&scope=readonline&cflag=html&dflag=xml&pages=&language=CHS&trial=&nonce=FE3EEB63955644E0BA4A3EE38061AB2B (accessed on 20 October 2026).
48. Zhang, P.; Wang, Q.; Ma, Z. GPS velocity field and active crustal deformation in and around the Tibet Plateau. *Earth Sci. Front.* **2002**, *2*, 442–450. Available online: https://kns.cnki.net/reader/xml?invoice=YwD8ttCq6YXkbJzITKQ%2BjMpNj2eNrAgViet-IDXn44%2F9NpTWfwOcbXjnQWhhfahLeNbhmWF2sTImzm7WdMmhPDuTs1DK9q%2FbSBtFIhXZrAb-wHKOVJ%2F%2B9HXP0rkb53ZcKl3avDpRQMFmLN6PbuLhDf7esKmjw1j1nZ65bvpHJRh1g%3D&platform=NZKPT&sourcetype=nxgp&product=CJFQ&filename=DXQY200202035&tablename=cjfd2002&type=JOURNAL&scope=readonline&cflag=html&dflag=xml&pages=&language=CHS&trial=&nonce=7D541A07509B481EBE91A36E968EDF56 (accessed on 20 October 2026).
49. Wang, J.; Liu, L.; Zhu, S.; Han, Y. A study on the relationship between GPS-ground strain rate field and seismicity in the Chinese mainland. *Earthq. Res. China* **2015**, *31*, 629–637. Available online: https://kns.cnki.net/reader/xml?invoice=WvxeR5j9fLoEX-YKY0PWnkhTVzrgk44yrQ3PijaL9gRLq1PSL3SBKb8A6lkNqNLtpLoWtzr7JJ2FlxjYzG6uOlzr9q8WfAw-

ZAvwYn8R%2BDbpQzN0NWffnIgSDxeJPwUO%2F7ePfAhgJHYPxdWOmZUWx5pZ9N8LdRX0qrsKmv4nkMUs0%3D&platform=NZKPT&sourcetype=nxgp&product=CJFQ&filename=ZGZD201504003&tablename=cjfdlast2016&type=JOURNAL&scope=readonline&cflag=html&dflag=xml&pages=&language=CHS&trial=&nonce=8DB099C8A8C249ABBB52957567827332 (accessed on 20 October 2026).

50. Cui, D.; Hao, M.; Li, Y.; Wang, W.; Qin, S.; Li, C. Present-day crustal movement and strain of the surrounding area of Ordos block derived from repeated GPS observations. *Chin. J. Geophys.* **2016**, *59*, 3646–3661. https://doi.org/10.6038/cjg20161012.
51. Okada, Y. Surface deformation due to shear and tensile faults in a half-space. *Bull. Seismol. Soc. Am.* **1985**, *75*, 1125–1154.
52. Okada, Y. Internal deformation due to shear and tensile faults in a half-space. *Bull. Seismol. Soc. Am.* **1992**, *82*, 1018–1040.
53. Okada, Y. Simulated empirical law of coseismic crustal deformation. *J. Phys. Earth* **1995**, *43*, 697–713.
54. McCaffrey, R.; Stein, S.; Freymueller, J. Crustal block rotations and plate coupling. *Plate Bound. Zones Geodyn. Ser.* **2002**, *30*, 101–122.
55. McCaffrey, R.; King, R.W.; Payne, S.J.; Lancaster, M. Active tectonics of northwestern US inferred from GPS-derived surface velocities. *J. Geophys. Res. Solid Earth* **2013**, *118*, 709–723.
56. McCaffrey, R.; King, R.W.; Wells, R.E.; Lancaster, M.; Miller, M.M. Contemporary deformation in the Yakima fold and thrust belt estimated with GPS. *Geophys. J. Int.* **2016**, *207*, 1–11.
57. Shi, F.; Shao, Z.; Zhan, W.; Ding, X.; Zhu, L.; Li, Y. Numerical modeling of the shear modulus and stress state in active faults in the northeastern margin of the Tibet Plateau. *Chin. J. Geophys.* **2018**, *61*, 3651–3663. Available online: https://kns.cnki.net/reader/flowpdf?invoice=I2XPpej77HII0nNJAJZ%2F7d10n%2Ftmbc9Yuo%2FZqJXd6spIr6R6H9kW1tcW1ba5nLQxRHJyGcIjRn4GNRM9lZYB9Kq2Vkag8O17TK9M9XKVcUFTZYD9ZTXS4FSW3QXAXe0BdUp1RQ1kriN2CR5RBIx%2FbqwkD8%2FtBSnFoosnoqRZWxc%3D&platform=NZKPT&sourcetype=nxgp&product=CJFQ&filename=DQWX201809014&tablename=cjfdlast2022&type=JOURNAL&scope=trial&cflag=overlay&dflag=pdf&pages=1-2&language=CHS&trial=1-2&nonce=266A3B3A282A423E925C4EDF18DF2892 (accessed on 20 October 2026).
58. Wang, X.; Song, M.; Guo, W.; Chen, H.; Fang, Q. Possible Coulomb stress interactions between the three main earthquakes in the 1989 Datong-Yanggao earthquake swarm. *J. Seismol. Res.* **2022**, *45*, 560–569. Available online: https://kns.cnki.net/reader/flowpdf?invoice=NZRbuIAlQcl8dGO683brA9ADAstI3rRbt%2FitdTQi89b0ktPcfuyUmkhxkrS8utZWE6sjoiteKDs1cXSaUCujVwVSX6QMQWkRqcKP%2BnGK1Z7%2BhjBdqk3MxkkaknhbribRAriiuEUEwquHavrpwDgxTvM7YnOj1k6aArkcewS7s2Y%3D&platform=NZKPT&sourcetype=nxgp&product=CJFQ&filename=DZYJ202204007&tablename=cjfdlast2022&type=JOURNAL&scope=trial&cflag=overlay&dflag=pdf&pages=1-1&language=CHS&trial=1-1&nonce=D46C9EDD4F524234AA2F61C275406BBA (accessed on 20 October 2026).
59. Sun, Y.; Luo, G. Spatial-temporal migration of earthquakes in the northeastern Tibet Plateau: Insights from a finite Aelement model. *Chin. J. Geophys.* **2018**, *61*, 2246–2264. Available online: https://kns.cnki.net/reader/flowpdf?invoice=X577HtAKs%2F5w6DBZNNhxRsDRI3RWTLW0V13pt9qG9Kd2IHm5aKaXiaoof6GGxdLoDzzZrCK7rYWiNNlhuPG5Jndpa4hRbKNO18oYTlJYp2o3H5JSbP%2BuBh99oiCovOK4zaTMYm3FoZ0uldkvtk53eufSJFzguboqOwSpyvGKXhI%3D&platform=NZKPT&sourcetype=nxgp&product=CJFQ&filename=DQWX201806008&tablename=cjfdlast2018&type=JOURNAL&scope=trial&cflag=overlay&dflag=pdf&pages=1-2&language=CHS&trial=1-2&nonce=C7E556647BFF4B59A4D98BBF208CEBC3 (accessed on 20 October 2026).
60. Wang, S.; Zhang, X.; Zhang, S.; Zhang, X.; Xue, F. Characteristics of Recent Tectonic Deformation and Seismic Activityin the Northeastern Margin of Tibetan Plateau. *Acta Geosci. Sin.* **2005**, *3*, 209–216.
61. Xu, W.; Su, X.; Yu, S.; Zhu, Q. Faults activity and crustal deformation pattern on the northeastern corner of the Tibet Plateau. *Chin. J. Geophys.* **2024**, *67*, 2596–2611. Available online: https://kns.cnki.net/reader/flowpdf?invoice=kyC%2BTbVGUTYCuxMo8OVDx5xYbZTW8MTQE7euH5z3tCiEiXshBnxK57%2Fw8KYNgQawcLeUDJuZWVJdcOKJNd9w6phLItpDA%2FE1R3KjDDL6juaaRNZmrURXgRiwOkVw4aSPTfsG0qUdoRqeLAJuOJLTBO5SPn5RLqAilhuIwNtJdas%3D&platform=NZKPT&sourcetype=nxgp&product=CJFQ&filename=DQWX202407009&tablename=cjfdlast2024&type=JOURNAL&scope=trial&cflag=overlay&dflag=pdf&pages=1-2&language=CHS&trial=1-2&nonce=565E0971D93B4F35BAAD7EAB786C1A8B (accessed on 20 October 2026).
62. Li, C.; Chai, X.; Gan, W.; Hao, M.; Wang, Q.; Zhuang, W.; Yang, F. Kinematic characteristics of the Ordos block and its periphery based on GPS observations. *Seismol. Geol.* **2020**, *42*, 316–332. https://doi.org/10.3969/j.Issn.0253-4967.2020.02.005.
63. Chen, Y.; Chen, J.; Guo, B.; Li, S.; Qi, S.; Zhao, P.; Li, X. Crustal structure and deformation between different blocks in the northern part of the western margin of Ordos. *Chin. J. Geophys.* **2020**, *63*, 886–896. Available online:

https://kns.cnki.net/reader/flowpdf?invoice=BtKhZikwXO5CQRObTwv48JLckxn5ExUYtYV%2BcJgEDwJy1WT7QTLEx5sNj26iqlOnqhVhTuDvK3bkooRmbrZ9itFC%2FuhxjvgEmiOpAQs69f8P4p4wSBR9vp%2Fgp9EzXRjHAymOrlgcGAkHEndzp4eEXtXBQlEEH%2BaE4zpPzZWOrWI%3D&platform=NZKPT&sourcetype=nxgp&product=CJFQ&filename=DQWX202003011&tablename=cjfdlast2022&type=JOURNAL&scope=trial&cflag=overlay&dflag=pdf&pages=1-2&language=CHS&trial=1-2&nonce=B9E49D8CD9C541CC9C3AF955E30A598F (accessed on 20 October 2026).

64. Li, Y.; Cui, D.; Hao, M. GPS-Constrained Inversion of Slip Rate on Major Active Faults in the Northeastern Margin of Tibet Plateau. *Earth Sci.* **2015**, *40*, 1767–1780.
65. Gan, W.; Molnar, P.; Zhang, P.; Xiao, G.; Liang, S.; Zhang, K.; Li, Z.; Xu, K.; Zhang, L. Initiation of Clockwise Rotation and Eastward Transport of Southeastern Tibet Inferred from Deflected Fault Traces and GPS Observations. *GSA Bull.* **2021**, *134*, 1129–1142.
66. Lü, Z.; Wu, J.; Meng, G.; Qiao, X.; Xu, K. Analysis of spatial distribution of strain at eastern margin of Tibetan Plateau. *J. Geod. Geodyn.* **2014**, *34*, 19–23. Available online: https://kns.cnki.net/reader/flowpdf?invoice=J9nbVVnSSdVyB2th1RK3lAAbchwDJ4AaMLnj2sj5Ru%2BSzK6xxvLCTBjUs9j%2FDaOnEaLWLoxH9vsESciEI1Rtd58nmLeCsONTqGG8TAl%2BLALCTPrvrg48qZ6i7ef4V8mQewWVUtohNNJurDhsNC3QIovm7%2BCB7qh3dgux7GJHEmI%3D&platform=NZKPT&sourcetype=nxgp&product=CJFQ&filename=DKXB201401005&tablename=cjfd2014&type=JOURNAL&scope=trial&cflag=overlay&dflag=pdf&pages=&language=CHS&trial=&nonce=BFCFD471C070456AA1A83BC4A6228BFD (accessed on 20 October 2026).
67. Sheng, S.; Wan, Y.; Huang, J.; Bu, Y.; Li, X. Present tectonic stress field in the Circum-Ordos region deduced from composite focal mechanism method. *Chin. J. Geophys.* **2015**, *58*, 436–452. Available online: https://kns.cnki.net/reader/xml?invoice=C4ct%2FmK04I%2F7j8IuNGINwardqgWDStRaajeiI5DPKRhC1PtewabAvUK7XZ9c14bDg560wcZgX6cobE9I5ZwTsy1rxYCB3SF9z4OcoN71T3I5ETvztKk4uPaMHEaLgJ17n2Q7HJ490xpXmLWGnGk%2F7vJ1%2BKzOaKB3E8aD4OOEK8o%3D&platform=NZKPT&sourcetype=nxgp&product=CJFQ&filename=DQWX201502008&tablename=cjfdlast2022&type=JOURNAL&scope=readonline&cflag=html&dflag=xml&pages=&language=CHS&trial=&nonce=0949ACE91F0D4CCEA9890CAECACC2514 (accessed on 20 October 2026).
68. China Earthquake Administration Ordos Active Fault System Research Group. *Ordos Peripheral Active Fault System*; Seismic Publishing House: Beijing, China, 1988. Available online: https://sc.panda985.com/scholar?hl=zh-CN&as_sdt=0%2C5&q=++1988%E9%84%82%E5%B0%93%E5%A4%9A%E6%96%AF%E5%91%A8%E7%BC%98%E6%B4%BB%E5%8A%A8%E6%96%AD%E8%A3%82%E7%B3%BB&btnG=https://cir.nii.ac.jp/crid/1971712334731249459 (accessed on 20 October 2026).
69. Wang, H.; Gao, R.; Yin, A.; Xiong, X.; Kuang, C.; Li, W.; Huang, W. Deep structure geometry features of Haiyuan Fault and deformation of the crust revealed by deep seismic reflection profiling. *Chin. J. Geophys.* **2012**, *55*, 3902–3909. Available online: https://kns.cnki.net/reader/xml?invoice=L15ddcVyZwUXDKehj%2BJ553br3dM7veZszFcmkIle70x6yUMyyaDqXbV57L%2B7o8%2B2c30zv%2BxQOjRu29bYWswFvu8npyGLOZ3M1bisrYpmB%2B53HOxXMdv56cuUZWDe1hgnL%2BfsGguKjqwT298IjnOxZFD2pBhep%2Flw%2FZbayAvjK%2FI%3D&platform=NZKPT&sourcetype=nxgp&product=CJFQ&filename=DQWX201212004&tablename=cjfd2012&type=JOURNAL&scope=readonline&cflag=html&dflag=xml&pages=&language=CHS&trial=&nonce=A6A722DE507242438AAB4EDAD914631E (accessed on 20 October 2026).
70. Deng, Q.; You, H. Structural Activity Characteristics and Formation Mechanisms of the Peripheral Faulted Basin in Ordos. Geological Research Institute, National Earthquake Administration, Studies on Modern Crustal Movement (1)—Continental Rift Valleys and Deep-Seated Processes. 1985. Available online: https://sc.panda985.com/scholar?hl=zh-CN&as_sdt=0%2C5&q=+%E9%84%82%E5%B0%94%E5%A4%9A%E6%96%AF%E5%91%A8%E7%BC%98%E6%96%AD%E9%99%B7%E7%9B%86%E5%9C%B0%E5%B8%A6%E7%9A%84%E6%9E%84%E9%80%A0%E6%B4%BB%E5%8A%A8%E7%89%B9%E5%BE%81%E5%8F%8A%E5%85%B6%E5%BD%A2%E6%88%90%E6%9C%BA%E5%88%B6&btnG= (accessed on 20 October 2026).
71. Guo, X.; Jiang, C.; Wang, X.; Tian, X. Source mechanisms and stress field characteristics of small to medium earthquakes at the periphery of the Ordos block. *J. Geod. Geodyn.* **2017**, *37*, 675–685. https://doi.org/10.14075/j.jgg.2017.07.003.
72. Liang, K. Late Quaternary Tectonic Activity Characteristics of the Northwestern Margin of the Ordos block. Ph.D. Thesis, Institute of Geology, China Earthquake Administration, Beijing, China, 2019. Available online: https://kns.cnki.net/reader/flowpdf?invoice=gjPj4mR5hvyM0OTr6FXx8LanTufXQlGZ0dPYQFBUiF2CaEix6XVvgtNAfQa4fl4tdcQ3CNum7PA1rQXX2ItS8qlyxFPeJu

28k8NMEP8D57YdXHaRfEE2IJhljqKo9m1I%2FiYT2KyWwHH5mw%2BZKheISFDIt2GSAaIgImiX8xDrzBs%3D&platform=NZKPT&sourcetype=nxgp&product=CDFD&filename=1019177255.nh&tablename=cdfdlast2020&type=DISSERTATION&scope=trial&cflag=overlay&dflag=pdf&pages=1-15&language=CHS&trial=1-15&nonce=A903D48F8F5D420697E869BB064E8702 (accessed on 20 October 2026).

73. Zhang, P.; Xu, X.; Wen, X.; Ran, Y. Slip rates and recurrence intervals of the Longmen Shan fault zone, and tectonic implications for the mechanism of the May 12 Wenchuan earthquake, 2008, Sichuan, *China. Chin. J. Geophys.* **2008**, *4*, 1066–1073. Available online: https://kns.cnki.net/reader/flowpdf?invoice=q%2FMPljeY8b1KNsgVR49hrso9YbZqEWTWLyZiBRhQLzkbvYB4crHoqjnVboQWMO6uj0Q%2BK%2BNGjNAImtU66gMaD8Zil1RnPjg4bj1%2BK%2Fd71NufOLKzPekW3bGdXKhEhxkclJH%2FZYMUQ3YET%2F24WNrzWSGsXHWJ%2B69ZNBW9zBP0nfo%3D&platform=NZKPT&sourcetype=nxgp&product=CJFQ&filename=DQWX200804017&tablename=cjfd2008&type=JOURNAL&scope=trial&cflag=overlay&dflag=pdf&pages=&language=CHS&trial=&nonce=ED1528053B294D5992715A85C20B039C (accessed on 20 October 2026).

74. Zhang, P. Late Quaternary tectonic deformation and earthquake hazard in continental China. *Quat. Sci.* **1999**, *19*, 404–413. Available online: https://kns.cnki.net/reader/flowpdf?invoice=m5IFsITSgNl5490IUeReRF6Vp3L9PzyUjQZ0VCGaCyKxSKP9d6gtrj0mDeqOyl1Adw0uZeNPlDvGC2z%2BDKSZhf0sBh8xL5gKV2X%2BnenuivYuLOF%2BRkv%2F76A2ra6mW0OSv%2BU3i3grVRjoSX3AxUQz8BykB6kbiwEh7skfOFSZFa4%3D&platform=NZKPT&sourcetype=nxgp&product=CJFQ&filename=DSJJ199905002&tablename=cjfd9899&type=JOURNAL&scope=trial&cflag=overlay&dflag=pdf&pages=&language=CHS&trial=&nonce=0E4AF0C8852D4747A171CD2EB264E86C (accessed on 20 October 2026).

75. Zhang, R.; Zhang, Z.; Zheng, D.; Liu, X.; Lei, Q.; Shao, Y. Coulomb stress transfer of strong earthquakes within tectonic belts near western Ordos block. *Chin. J. Geophys.* **2021**, *64*, 3576–3599. Available online: https://kns.cnki.net/reader/flowpdf?invoice=ERcxTguzswKxsEPhlroEKKj3TMveUrESxA8hDu%2FQu7rTVWaD5D8eqIqPUTCqsXbv0%2FZ44SibU08VVXWuoKnj%2B81OaCzPc0p4%2F8tDab%2BmhBhOoCCqOV5IGOzPl%2BwJfPFnSHkqxVSTx8u8akw9BIZC7J1xt1436ZUjyaOcTxhh9GE%3D&platform=NZKPT&sourcetype=nxgp&product=CJFQ&filename=DQWX202110014&tablename=cjfdlast2021&type=JOURNAL&scope=trial&cflag=overlay&dflag=pdf&pages=1-3&language=CHS&trial=1-3&nonce=B3C7BDAAA5BC48C180A0DABD619127AD (accessed on 20 October 2026).

76. Fan, Y.; Che, Z. The fault activity in recent time along northern section of North-South Seismic Belt and its both sides. *Earthquake* **2022**, *21*, 87–93. Available online: https://kns.cnki.net/reader/xml?invoice=CXCizWI4vJa2L69XU%2B0kAZtm7eBarEMY1x3mamVvx48Od5Ewy5lQGzSJwaWBm%2FrIAkkgvEUOEMtpAEM2ryUJdJG36lwraqxQ1T1OSC03PpDH3IevsrlmMfN0Vw6HPOFECKAALa5%2FJqW5CmKH5%2B4XXvrTxTq4IXcV34JO8ZShPYQ%3D&platform=NZKPT&sourcetype=nxgp&product=CJFQ&filename=DIZN200102013&tablename=cjfd2001&type=JOURNAL&scope=readonline&cflag=html&dflag=xml&pages=&language=CHS&trial=&nonce=4BFE3B622CBD453F849A3206E7ED3C26 (accessed on 20 October 2026).

77. Ren, X.; Zhao, W.; Chai, C.; Liu, X. Estimation of recurrent interval of strong earthquakes in ns earthquake belt. *Inland Earthq.* **2002**, *1*, 69–75. Available online: https://kns.cnki.net/reader/xml?invoice=wO0fvLYb84mnUiODIp2%2Fqzpy3CV6LAVDFmmtl3z%2FKRs4nFnFaE1FwyfOnS7kHRMd2hV2V3UvNnmYl%2FvjxwpG8spXr0b%2BBY8jMPK%2BdhLdmpclAECPFa4l5SFVPf8u2kvar2BBX37Gbod5%2Bt%2FWzZiSavHelBBLkdXY%2BYK5Z5hRFxs%3D&platform=NZKPT&sourcetype=nxgp&product=CJFQ&filename=LLDZ200201011&tablename=cjfd2002&type=JOURNAL&scope=readonline&cflag=html&dflag=xml&pages=&language=CHS&trial=&nonce=ECF8B1FF4FE54FD79337289EDE30A7AA (accessed on 20 October 2026).

78. Du, F.; Wen, X.; Feng, J.; Liang, M.; Long, F.; Wu, J. Seismic-tectonic characteristics and strong earthquake risk background of the Liupanshan fault zone. *Chin. J. Geophys.* **2018**, *61*, 545–559. https://doi.org/10.6038/cjg2018L0181.
79. Wei, C. Study of the Present Crustal Deformation Characteristics of the Southwest Margin of Ordos Block Using GPS. Master's Thesis, Lanzhou Institute of Seismology, China Earthquake Administration, Lanzhou, China, 2020. Available online: https://kns.cnki.net/reader/flowpdf?invoice=u2lcM17rW%2FtdDWa7cge53oOO%2FDIVMYrKo2boJ0uwx01h51qJlckcAzi4efIwm0GWVq7mBz8uY2lI4CTEiINZNu27pqEUkchg%2B9D3vD0mU93BwEBAB60kS5U7x9fHWCk5cVt7lEkLhyyr0PgKdvAf4ASQSyqklWLUW2ipuD6gkSQ%3D&platform=NZKPT&sourcetype=nxgp&product=CMFD&filename=1020020143.nh&tablename=cmfd202201&type=DISSERTATION&scope=trial&cflag=overlay&dflag=pdf&pages=1-9&language=CHS&trial=1-9&nonce=DD24CD8FE3D64D8FAD051126C6C89C0C (accessed on 20 October 2026).

Disclaimer/Publisher's Note: The statements, opinions and data contained in all publications are solely those of the individual author(s) and contributor(s) and not of MDPI and/or the editor(s). MDPI and/or the editor(s) disclaim responsibility for any injury to people or property resulting from any ideas, methods, instructions or products referred to in the content.